Non-Maxwellianity of electron distributions near Earth's magnetopause

Daniel Bruce Graham[1], Yuri V. Khotyaintsev[1], Mats André[1], Andris Vaivads[2], Alexandros Chasapis[3], William H. Matthaeus[4], Alessandro Retino[5], Francesco Valentini[6], and Daniel J Gershman[7]

[1]Swedish Institute of Space Physics
[2]KTH Royal Institute of Technology, Stockholm, Sweden
[3]University of Colorado
[4]University of Delaware
[5]Laboratoire de Physique des Plasmas - CNRS
[6]Università della Calabria
[7]NASA Goddard Space Flight Center

November 24, 2022

Abstract

Plasmas in Earth's outer magnetosphere, magnetosheath, and solar wind are essentially collisionless. This means particle distributions are not typically in thermodynamic equilibrium and deviate significantly from Maxwellian distributions. The deviations of these distributions can be further enhanced by plasma processes, such as shocks, turbulence, and magnetic reconnection. Such distributions can be unstable to a wide variety of kinetic plasma instabilities, which in turn modify the electron distributions. In this paper the deviations of the observed electron distributions from a bi-Maxwellian distribution function is calculated and quantified using data from the Magnetospheric Multiscale (MMS) spacecraft. A statistical study from tens of millions of electron distributions shows that the primary source of the observed non-Maxwellianity are electron distributions consisting of distinct hot and cold components in Earth's low-density magnetosphere. This results in large non-Maxwellianities in at low densities. However, after performing a stastical study we find regions where large non-Maxwellianities are observed for a given density. Highly non-Maxwellian distributions are routinely found are Earth's bowshock, in Earth's outer magnetosphere, and in the electron diffusion regions of magnetic reconnection. Enhanced non-Maxwellianities are observed in the turbulent magnetosheath, but are intermittent and are not correlated with local processes. The causes of enhanced non-Maxwellianities are investigated.

Non-Maxwellianity of electron distributions near Earth's magnetopause

D. B. Graham [1], Yu. V. Khotyaintsev [1], M. André [1], A. Vaivads [2], A. Chasapis [3], W. H. Matthaeus [4], A. Retino [5], F. Valentini [6], D. J. Gershman [7,8]

[1]Swedish Institute of Space Physics, Uppsala, Sweden.
[2]Space and Plasma Physics, School of Electrical Engineering and Computer Science, KTH Royal Institute of Technology, Stockholm, Sweden.
[3]Laboratory of Atmospheric and Space Physics, University of Colorado, Boulder, CO, USA.
[4]Department of Physics and Astronomy, University of Delaware, Newark, DE, USA.
[5]Laboratoire de Physique des Plasmas, CNRS/Ecole Polytechnique/Sorbonne Université/ Université Paris-Sud/Observatoire de Paris, Paris, France.
[6]Dipartimento di Fisica, Università della Calabria, Arcavacata di Rende, Italy.
[7]NASA Goddard Space Flight Center, Greenbelt, MD, USA.
[8]Department of Astronomy, University of Maryland, College Park, MD, USA.

Key Points:

- 1: Electron non-Maxwellianity is computed for 6 months of data (~85 million electron distributions).
- 2: Electron non-Maxwellianity is typically large in the magnetosphere due to hot and cold electron populations.
- 3: Enhanced non-Maxwellianity is found in reconnection regions, the bowshock, and magnetosheath turbulence.

Corresponding author: D. B. Graham, `dgraham@irfu.se`

Abstract

Plasmas in Earth's outer magnetosphere, magnetosheath, and solar wind are essentially collisionless. This means particle distributions are not typically in thermodynamic equilibrium and deviate significantly from Maxwellian distributions. The deviations of these distributions can be further enhanced by plasma processes, such as shocks, turbulence, and magnetic reconnection. Such distributions can be unstable to a wide variety of kinetic plasma instabilities, which in turn modify the electron distributions. In this paper the deviations of the observed electron distributions from a bi-Maxwellian distribution function is calculated and quantified using data from the Magnetospheric Multiscale (MMS) spacecraft. A statistical study from tens of millions of electron distributions shows that the primary source of the observed non-Maxwellianity are electron distributions consisting of distinct hot and cold components in Earth's low-density magnetosphere. This results in large non-Maxwellianities in at low densities. However, after performing a stastical study we find regions where large non-Maxwellianities are observed for a given density. Highly non-Maxwellian distributions are routinely found are Earth's bowshock, in Earth's outer magnetosphere, and in the electron diffusion regions of magnetic reconnection. Enhanced non-Maxwellianities are observed in the turbulent magnetosheath, but are intermittent and are not correlated with local processes. The causes of enhanced non-Maxwellianities are investigated.

1 Introduction

Many space and astrophysical plasmas are essentially collisionless so Coulomb collisions are unlikely to be efficient in keeping particle distributions close to thermal equalibrium, i.e., a Maxwellian distribution. As a result non-Maxwellian distributions can readily develop and are indeed frequently observed in space plasmas. In collisionless plasmas non-Maxwellian distributions can remain kinetically stable, which need not relax to Maxwellian distributions. However, non-Maxwellian distributions can be important source of instabilities and can potentially generate a variety of electrostatic and electromagnetic waves. Plasma processes such as shocks, magnetic reconnection, and turbulence can further increase the deformations in the particle distributions from a Maxwellian distribution. Quantifying the deviation in particle distributions is crucial to understanding the effects of both large-scale processes, such as shocks and magnetic reconnection, and kinetic-scale processes, such as wave-particle interactions.

At present various papers have considered the non-Maxwellianity of particle distributions in both simulations and observations [*Greco et al.*, 2012; *Valentini et al.*, 2016; *Chasapis et al.*, 2018; *Perri et al.*, 2020; *Liang et al.*, 2020]. These studies have focused on plasma turbulence in Earth's magnetosheath and magnetic reconnection. The simulation results showed that ion non-Maxwellianity was spatially non-uniform and was associated with strong currents and temperature anisotropy [*Greco et al.*, 2012; *Valentini et al.*, 2016]. Similarly, electron non-Maxwellianity was found to increase the electron diffusion region (EDR) and separatrices of magnetic reconnection [*Liang et al.*, 2020]. In kinetic simulations the background distributions, such as in modeling of magnetosheath turbulence and magnetic reconnection, are assumed to be Maxwellian. Such distributions are not necessarily valid in Earth's magnetosheath and magnetopause, where the background distributions can differ significantly from a Maxwellian distribution while remaining kinetically stable. Recent observations from the Magnetospheric Multiscale (MMS) spacecraft suggest that ion non-Maxwellianity is weakly correlated with the local current sheets in the turbulent magnetosheath [*Perri et al.*, 2020]. In contrast, *Chasapis et al.* [2018] found that electron non-Maxwellianity tended to increase in regions of strong currents. Estimates of the non-Maxwellianity of particle distributions based on recent MMS observations have only focused on very short time intervals. Thus, it is unclear if such deviations from Maxwellianity are statistically significant when compared with a large volume of data. Therefore, a statistical study of the non-Maxwellianity is required.

The purpose of this paper is to investigate and quantify the non-Maxwellianity of electron distribution functions in the near Earth plasma environment, specifically near Earth's magnetopause, in the magnetosheath, and near the bowshock. In this paper we propose a measure of the deviation of the observed electron distribution function from a bi-Maxwellian distribution function, where temperature anisotropy is included. We show that statistically the non-Maxwellianity of electron distributions increases as plasma density decreases. Large deviations of observed electron distributions from a bi-Maxwellian distribution function are observed in the outer magnetosphere, in magnetic reconnection electron diffusion regions, at the bowshock, and intermittently in magnetosheath turbulence. The outline of this paper is as follows: Section 2 the data used is stated, section 3 states the theory and methods used to calculate electron non-Maxwellianity, section 4 presents the statistical results, section 5 presents case studies of the reconnection ion and electron diffusion regions, the bowshock, and magnetosheath turbulence, and section 6 states the conclusions.

2 Data

In this paper we use high-resolution burst mode data from the four MMS spacecraft [*Burch et al.*, 2016]. We use particle distributions and moments from Fast Plasma Investigation (FPI) [*Pollock et al.*, 2016]. Three-dimensional electron distributions and moments are sampled every 30 ms. The electron distributions are sampled over 32 energy channels ranging from 10 eV to 30 keV, which covers the thermal electron energy range in the outer magnetosphere and magnetosheath. Ion distributions and moments are sampled every 150 ms. We use electric field **E** and magnetic field **B** data from the Electric field Double Probes (EDP) [*Lindqvist et al.*, 2016; *Ergun et al.*, 2016] and Fluxgate Magnetometer (FGM) [*Russell et al.*, 2016], respectively. The spacecraft potential V_{sc} is computed from the Spin-plane Double Probes (SDP).

3 Theory and methods

In this section we define the non-Maxwellianity parameter ϵ. The non-Maxwellianity ϵ is defined as the velocity space integrated absolute difference between the observed distribution function and a model bi-Maxwellian distribution function given by the particle moments:

$$\epsilon = \frac{1}{2n_e} \int_{v,\theta,\phi} |f_e(v,\theta,\phi) - f_{\text{model}}(v,\theta,\phi)| v^2 \sin\theta dv d\theta d\phi, \tag{1}$$

where v is the electron speed, θ is the polar angle, ϕ is the azimuthal angle, n_e is the electron number density, $f_e(v,\theta,\phi)$ is the observed velocity-space density, and $f_{\text{model}}(v,\theta,\phi)$ is the velocity space density of the model distribution. The factor $1/(2n_e)$ normalizes ϵ to a dimensionless quantity with domain $\epsilon \in [0,1]$, where $\epsilon = 0$ corresponds to no deviation of $f_e(v,\theta,\phi)$ from $f_{\text{model}}(v,\theta,\phi)$ and $\epsilon = 1$ corresponds to a maximal deviation, such that there is no overlap $f_e(v,\theta,\phi)$ and $f_{\text{model}}(v,\theta,\phi)$ in velocity space. For f_{model} we use a drifting bi-Maxwellian distribution, given by:

$$f_{\text{model}}(\mathbf{v}) = \frac{n_e}{\pi^{3/2} v_{e,\parallel}^3} \frac{T_{e,\parallel}}{T_{e,\perp}} \exp\left(-\frac{(v_\parallel - V_\parallel)^2}{v_{e,\parallel}^2} - \frac{(v_{\perp,1} - V_\perp)^2 + v_{\perp,2}^2}{v_{e,\parallel}^2 (T_{e,\perp}/T_{e,\parallel})} \right), \tag{2}$$

where $T_{e,\parallel}$ and $T_{e,\perp}$ are the parallel and perpendicular electron temperatures, $v_{e,\parallel} = \sqrt{2k_B T_{e,\parallel}/m_e}$ is the parallel electron thermal speed, $V_\parallel$ is the bulk velocity parallel to **B**, $V_\perp$ is the magnitude of the bulk velocity perpendicular to **B**, and k_B is the Boltzmann constant. This calculation of ϵ corresponds to the lowest order moment, i.e., number density, so finite ϵ will result from deviations from a bi-Maxwellian at thermal electron energies. The velocity coordinates $(v_{\|}, v_{\perp,1}, v_{\perp,2})$ used in equation (2) are defined such that $v_{\|}$ is the speed along the magnetic field direction, $v_{\perp,1}$ is the speed along the perpendicular bulk velocity direction, and $v_{\perp,2}$ is orthogonal to $v_{\|}$ and $v_{\perp,1}$. The parameters n_e, $\mathbf{V}_e$, and $\mathbf{T}_e$, used to calculate f_{model} are the FPI-DES electron moments [*Pollock et al.*, 2016]. To compute ϵ we transform f_{model} into the same coordinate system and discretize to the same energy and angle channels as the observed f_e for direct comparison. We note that this definition of ϵ differs from the definition used in previous studies [e.g., *Greco et al.*, 2012]. The definition of *Greco et al.* [2012] is closely related to the enstrophy of the particle distribution [*Servidio et al.*, 2017]. We have used the definition in equation (1) because: (1) The definition used in *Greco et al.* [2012] is not dimensionless, which is problematic when there are large changes in density, such as across the magnetopause. (2) We have used a drifting bi-Maxwellian distribution as f_{model}, rather than an isotropic Maxwellian distribution, so that increases in ϵ do not simply correspond to large bulk electron flows in the spacecraft frame, or large temperature anisotropies, which are straightforward to obtain from the particle moments. In equation (2) we have assumed a single perpendicular electron temperature $T_{e,\perp}$ meaning f_{model} is gyrotropic, so agyrotropic features of the observed electron distribution will not be captured by the model distribution. Thus, agyrotropic distributions, such as those found in the electron diffusion regions of magnetic reconnection, should result in an increased ϵ.

At low electron energies, there are several effects that can artificially increase ϵ. These include:

(1) Spacecraft photoelectrons are detected when the Active Spacecraft Potential Control (ASPOC) [*Torkar et al.*, 2016] is off and the spacecraft potential is larger than $\approx$ 10 eV. The energy channels affected by spacecraft photoelectrons are removed and the remaining energy channels are corrected for when calculating ϵ, so the effect of spacecraft photoelectrons should be small.

(2) Photoelectrons generated inside the electron detectors produce enhancements in the phase space density [*Gershman et al.*, 2017]. This affects the Sunward pointing detectors, and can occur at energies exceeding eV_{sc}.

(3) Secondary photoelectrons can occur within the detector, resulting in artifically large phase-space densities at low energies. These electrons can occur at energies exceeding eV_{sc}.

(4) Low-energy electrons can be focused along the spin-plane and axial booms, which are positively charged [e.g., *Toledo-Redondo et al.*, 2019]. In addition, when ASPOC is on the ion plumes are emitted from the spacraft, modifying the motion of low-energy electrons [*Barrie et al.*, 2019]. This can distort the measured electron distribution at low energies.

While there is a model for internal photoelectrons [*Gershman et al.*, 2017], which can approximately remove these effects, the other effects are not straightforward to remove. Therefore, we simply perform the calculation of ϵ for electron energies $E > 28$ eV. This corresponds to neglecting the lower 4 energy channels in the FPI-DES distribution functions for phase 1a of MMS operations when evaluating equation (1). In addition, energy channels with eV/e< V_{sc} are removed, and the energy channels are corrected by $-eV_{sc}$ when calculating f_{model} and ϵ. The spacecraft potential V_{sc} is computed from the average probe-to-spacecraft potentials of the four spin-plane probes. This average probe-to-spacecraft potential was compared to the cutoff energies of photoelectrons seen in FPI-DES data to calibrate V_{sc} [*Graham et al.*, 2018].

As examples of the calculation of ϵ, Figure 1 shows three observed electron distributions, the associated f_{model}, and values of ϵ. The distributions are from a reconnection event observed at the magnetopause on 30 October 2015 [*Graham et al.*, 2016a]. The first distribution is in the magnetosphere close to the magnetopause (Figures 1a–1c), the second distribution is close to the reconnection ion diffusion region where $T_{e,\|}/T_{e,\perp}$ peaks (Figures 1d–1f), and the third distribution is in the magnetosheath where $T_{e,\|}/T_{e,\perp} < 1$ (Figures 1g–1i).

Figure 1a shows an approximately isotropic electron distribution with $T_{e,\|}/T_{e,\perp} = 1.1$ and $\epsilon = 0.20$. The modeled distribution (Figure 1b) is an approximately isotropic distribution. One of the differences between the observed and modeled distribution is the fluctuations in f_e due to the counting statistics of the particle instrument at relatively low $n_e \lesssim 1\,\mathrm{cm}^{-3}$, which results in an increase in ϵ. This can be seen by comparing Figures 1a and 1b; the observed f_e shows fluctuations as functions of speed and angle, while the modeled f_e smoothly varies. Figure 1c shows that quantitively there is some deviation of the observed distribution from $f_{\rm model}$. In particular, at pitch angle $\theta = 90°$, the shape of f_e differs from $f_{\rm model}$ in the thermal energy range.

For the second distribution both f_e and $f_{\rm model}$ are qualitatively similar. However, Figure 1f shows that there is significant deviation in f_e from $f_{\rm model}$. For $\theta = 90°$, f_e is close to Maxwellian at thermal energies, while for $\theta = 0°$ and 180° a flat-top distribution is observed, which deviates from the shape of a Maxwellian. Thus, the flat-top distribution corresponds to an enhanced non-Maxwellianity of $\epsilon = 0.17$.

The final distribution is in the high-density magnetosheath, so there is little noise in f_e because the particle counts are high. Here, f_e and $f_{\rm model}$ are very similar, although there are some deviations in f_e from $f_{\rm model}$, as seen in Figure 1i. For this distribution $\epsilon = 0.1$, corresponding to relatively small deviations from a bi-Maxwellian distribution.

4 Statistical results

In this section we investigate the statistical properties of ϵ. We calculate ϵ for all burst mode electron data from September 2015 to March 2016 (the first magnetopause phase of the MMS mission), corresponding to $\sim$ 85 million distributions from the four spacecraft. We first consider the dependence of ϵ on n_e. Low-densities correspond to the outer magnetosphere, while high densities typically correspond to the magnetosheath. In Figure 2 we plot two-dimensional histograms of $\log_{10}(\epsilon)$ versus $\log_{10}(n_e)$ for data when ASPOC is off, ASPOC is on, and all data in panels (a)–(c), respectively. In all three panels we see that for $n_e \lesssim 10$ cm^{-3} there is statistically an increase in ϵ as n_e decreases, which approximately scales as $\epsilon \propto 1/\sqrt{n_e}$. For $n_e \gtrsim 10$ cm^{-3}, typically corresponding to the magnetosheath, we find that ϵ does not depend strongly on n_e. We find that ϵ is not strongly affected by whether or not ASPOC is on, except at low n_e, where ϵ is slightly larger when ASPOC is on. This might be due to the internal photoelectron emission in the FPI detectors, which is more significant at low n_e and the spacecraft potential is low, or due to distortions in the observed electron distribution by the plume of ions around the spacecraft when ASPOC is on [*Barrie et al.*, 2019]. We do not find any statistical differences between the four spacecraft (not shown).

There are two main reasons for the increase in ϵ at low n_e in the magnetosphere:

(1) In the magnetosphere distinct cold and hot electron populations are frequently present at the same time [*Walsh et al.*, 2020]. In these cases the total effective electron

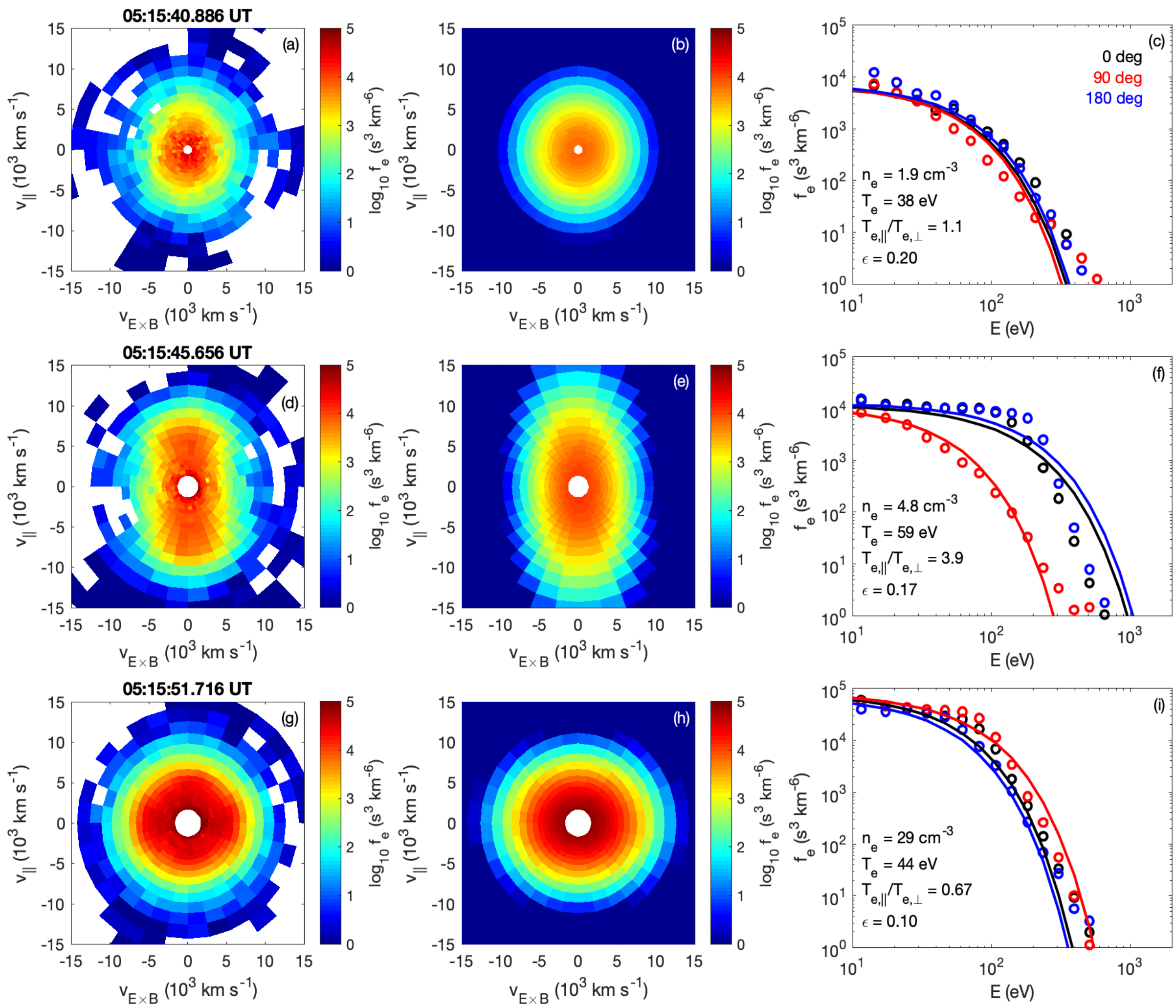

Figure 1. Three examples of electron distributions and the predicted bi-Maxwellian distribution based on the electron moments from MMS1 on 30 October 2015. Panels (a), (d), and (g) show a two-dimensional slice of the observed three-dimensional electron distribution in the **B** and **E** × **B** plane. Panels (b), (e), and (h) show the modeled bi-Maxwellian distributions in the same plane. Panels (c), (f), and (i) show the phase-space densities at pitch angles 0° (black), 90° (red), and 180° (blue) for the observed distributions (circles) and modeled bi-Maxwellian (solid lines). The distribution in panels (a)–(c) is in the magnetosphere, (d)–(f) is near the ion diffusion region where $T_{e,\|}/T_{e,\perp}$ peaks, (g)–(i) is in the magnetosheath where $T_{e,\|}/T_{e,\perp}$ is minimal. The electron distribution properties and ϵ of the three distributions are given in panels (c), (f), and (i).

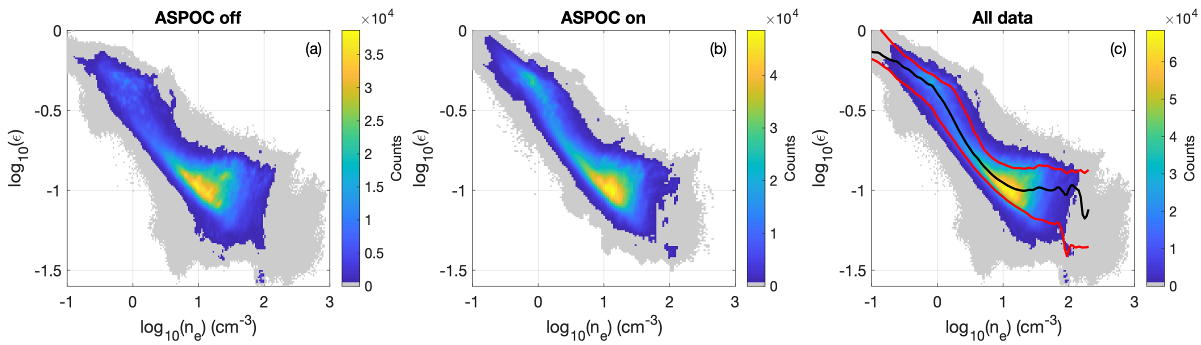

Figure 2. Two-dimensional histograms of $\log_{10}(n_e)$ versus $\log_{10}(\epsilon)$. (a) Histogram for data when ASPOC is off, (b) histogram for data when ASPOC is on, and (c) histogram for all data. The color shading indicates the counts. The black line indicates the median (50th percentile) of ϵ as a function n_e and the lower and upper red curves indicate the 10th and 90th percentiles as a function of n_e, respectively.

temperature is

$$T_e \approx \frac{n_c T_c + n_h T_h}{n_c + n_h}, \tag{3}$$

where the subscripts c and h refer to the cold and hot electron components. When n_c and n_h are comparable T_e differs significantly from T_c and T_h, and large ϵ develop. In the magnetosheath the electron distributions are characterized by a single temperature, although the shape can differ from bi-Maxwellian distribution. This results in a smaller ϵ in the magnetosheath compared to the magnetosphere.

(2) As n_e decreases the particle counts measured in each energy and angle bin of FPI-DES decreases. This results in increased statistical uncertainty, corresponding to a more grainy looking distribution at lower density, which differs from the smooth f_{model} distribution, resulting in an increase in ϵ.

The first effect iss physical and due to differences in typical magnetospheric and magnetosheath distributions, while the second effect is an instrumental effect. Both effects result in the statistical increase in ϵ as n_e decreases, seen in Figure 2. To illustrate these two effects, we plot two electron distributions in Figure 3. The first distribution (top row) is in the magnetosphere close to the magnetopause. For this distribution we calculate $\epsilon = 0.69$. The second distribution (bottom row) is in the magnetosheath close to the magnetopause. For this distribution we calculate $\epsilon = 0.085$. Both distributions are observed by MMS1 on 06 December 2015 when the spacecraft crossed the magnetopause

[*Khotyaintsev et al.*, 2016]. Figures 3a and 3b show 2D slices of the observed f_e in the **B** and $\mathbf{E} \times \mathbf{B}$ plane and f_{model} calculated from the particle moments. The distribution in Figure 3a is characterized by a very cold component, with $n_c = 0.3$ cm^{-3} and $T_c = 27$ eV, and a hot component, with $n_h = 0.06$ cm^{-3} and $T_h = 5$ keV. The total distribution has $n_e = 0.36$ cm^{-3} and $T_e = 1$ keV. Thus, f_{model} shown in Figure 3b differs from both the cold and hot components of f_e, resulting in a large ϵ. In Figure 3c we plot $(f_e - f_{\mathrm{model}})v^3$, which indicates the regions of velocity space that contribute most significantly to ϵ. The largest contribution is from low energies, where $f_e \gg f_{\mathrm{model}}$ and most of the particles are located. At intermediate energies ~ 1 keV, $f_e \ll f_{\mathrm{model}}$ because f_{model} has $T_e = 1$ keV, whereas f_e is negligible due to the temperatures of the two components. For $E \sim 5$ keV, $f_e \gg f_{\mathrm{model}}$ due to $T_h > T_e$. As a result $|f_e - f_{\mathrm{model}}|$ is large over almost all velocity space making ϵ large.

At low densities the counts per energy and angle bin are small and in many cases no counts are measured, as indicated by the white regions in Figure 3a. This results in a more grainy looking f_e, in contrast to the smooth f_{model} (Figure 3b). This results in ϵ tending to increase as n_e decreases. At high densities the counts are very high in the thermal energy range (for example, the distribution in Figure 3d), so the effects of the finite counting statistics are small. In Appendix A: we show that the most significant contribution to ϵ in the magnetosphere is the distinct cold and hot electron populations. The effect of the counting statistics on ϵ is smaller when hot and cold electrons are present.

For the distribution in Figure 3d only a single electron population is observed, characterized by $n_e = 21$ cm^{-3} and $T_e = 74$ eV. As a result f_{model} (Figure 3e) is very similar to f_e, and $\epsilon = 0.085$. Despite f_e and f_{model} looking similar, non-Maxwellian features are observed in the thermal energy range, as shown in Figure 3f.

In Figure 2c we overplot the median ϵ (ϵ_{50}) in black, and the 10th and 90th percentiles ϵ_{10} and ϵ_{90} (lower and upper red curves, respectively) as functions of n_e. We find that $\epsilon_{50} \approx 0.1$ is approximately constant for $10\,\mathrm{cm}^{-3} \lesssim n_e \lesssim 100\,\mathrm{cm}^{-3}$. Because of the strong dependence of ϵ on n_e, we need to consider the statistical median and percentiles when considering specific events to determine if the electron distributions are unusually non-Maxwellian compared with the median values of ϵ. We will use these percentiles as a function of density to determine whether electron distributions in specific regions significantly deviate from a bi-Maxwellian distributions or not.

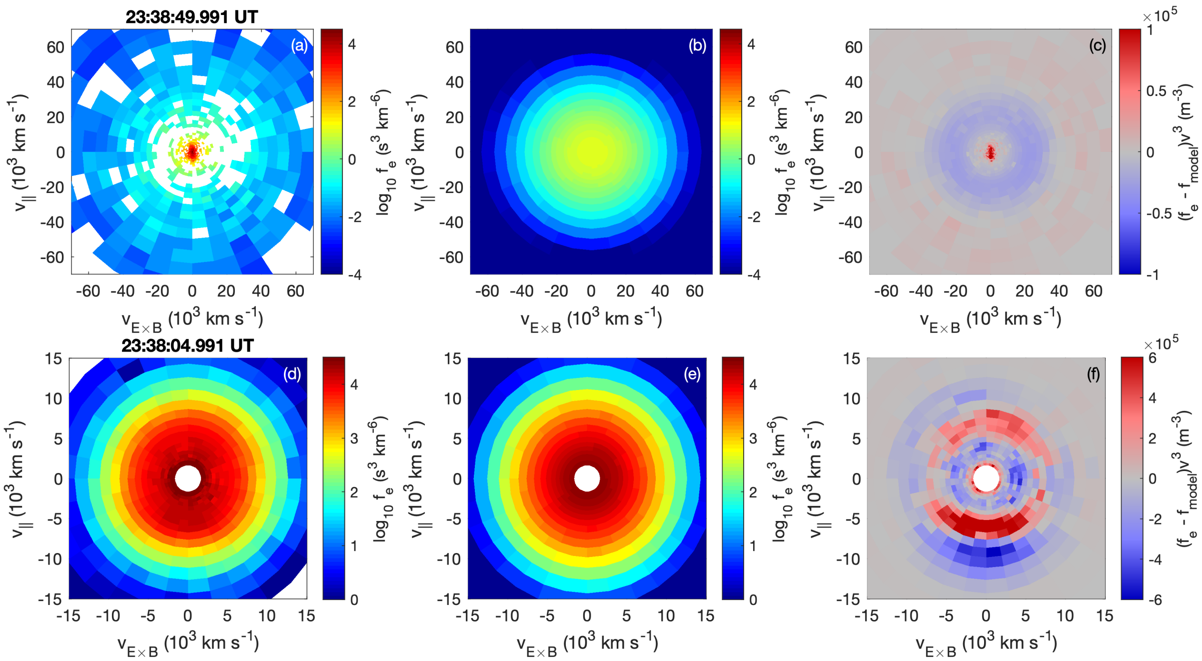

Figure 3. Two examples of electron distributions and the modeled bi-Maxwellian distribution based on the electron moments from MMS1 on 06 December 2015 (cf., *Khotyaintsev et al.* [2016]). Panels (a) and (d) show a two-dimensional slice of the observed three-dimensional electron distribution in the **B** and **E** $\times$ **B** plane. Panels (b) and (e) show the modeled bi-Maxwellian distributions in the same plane. Panels (c) and (f) show $(f_e - f_{\rm model})v^3$ in the same plane, which indicates the regions of velocity space that contribute most to ϵ. The distribution in panels (a)–(c) is in the magnetosphere close to the magnetopause, and (d)–(f) is in the magnetosheath close to the magnetopause.

In Figure 4a we plot the histogram of $\log_{10}\epsilon$ versus $\log_{10} T_e$. We find that statistically ϵ increases as T_e increases. This is primarily due to the statistical increase in T_e as n_e decreases. Low-density higher-temperature regions correspond to the outer magnetosphere, while high-density lower-temperature regions typically correspond to the magnetosheath. In Figure 4b we plot ϵ versus $\log_{10} T_{e,\|}/T_{e,\perp}$. Overall, we find that the statistical dependence of ϵ on $T_{e,\|}/T_{e,\perp}$ is relatively weak. However, the smallest ϵ are found for $T_{e,\|}/T_{e,\perp} \sim 1$. In this study there are more distributions with $T_{e,\|}/T_{e,\perp} > 1$ than $T_{e,\|}/T_{e,\perp} < 1$, with a median and mean $T_{e,\|}/T_{e,\perp}$ of 1.1 and 1.2, respectively.

We now compare ϵ with the agyrotropy of the electron distribution. We use the agyrotropy measure $\sqrt{Q}$ as defined in *Swisdak* [2016]. This measure is based on the off-diagonal components of the electron pressure tensor $\mathbf{P}_e$ and is given by

$$\sqrt{Q} = \left(\frac{P_{12}^2 + P_{13}^2 + P_{23}^2}{P_\perp^2 + 2P_\perp P_\|} \right)^{1/2}, \tag{4}$$

where we have rotated the measured $\mathbf{P}_e$ into the field-aligned coordinates of the form:

$$\mathbf{P}_e = \begin{pmatrix} P_\| & P_{12} & P_{13} \\ P_{12} & P_\perp & P_{23} \\ P_{13} & P_{23} & P_\perp \end{pmatrix}. \tag{5}$$

The agyrotropic measure $\sqrt{Q}$ has values between 0 and 1, with 0 corresponding to a gyrotropic distribution and 1 to maximum agyrotropy. In Figure 4c we plot the histogram of ϵ versus $\sqrt{Q}$ for $n_e > 5$ cm^{-3} (at lower n_e the agyrotropy measures tend to be unreliable). We find that the vast majority of distributions are approximately gyrotropic, with median and mean values of $\sqrt{Q}$ of 0.008 and 0.009, respectively. The largest values of $\sqrt{Q}$ observed are $\sim$ 0.1, which correspond to values observed in the EDRs of magnetopause reconnection [*Graham et al.*, 2017; *Norgren et al.*, 2016; *Webster et al.*, 2018]. For these large values of $\sqrt{Q}$ there is a tendency of ϵ to increase with $\sqrt{Q}$. However, only a tiny fraction of the distributions have large $\sqrt{Q}$, and for most distributions there is little dependence of ϵ on $\sqrt{Q}$. This is not surprising because: (1) gyrotropic distributions can deviate significantly from a bi-Maxwellian distribution function, and (2) $\sqrt{Q}$ is based on the pressure tensor, so large large off-diagonal pressure terms may not correspond to large changes in phase-space density.

In Figure 4d we plot the histogram of ϵ versus the magnitude of the current density $|\mathbf{J}|$ calculated from the particle moments. We find no correlation between ϵ and $|\mathbf{J}|$, which suggests that regions of large $|\mathbf{J}|$, such as narrow current sheets, do not significantly en-

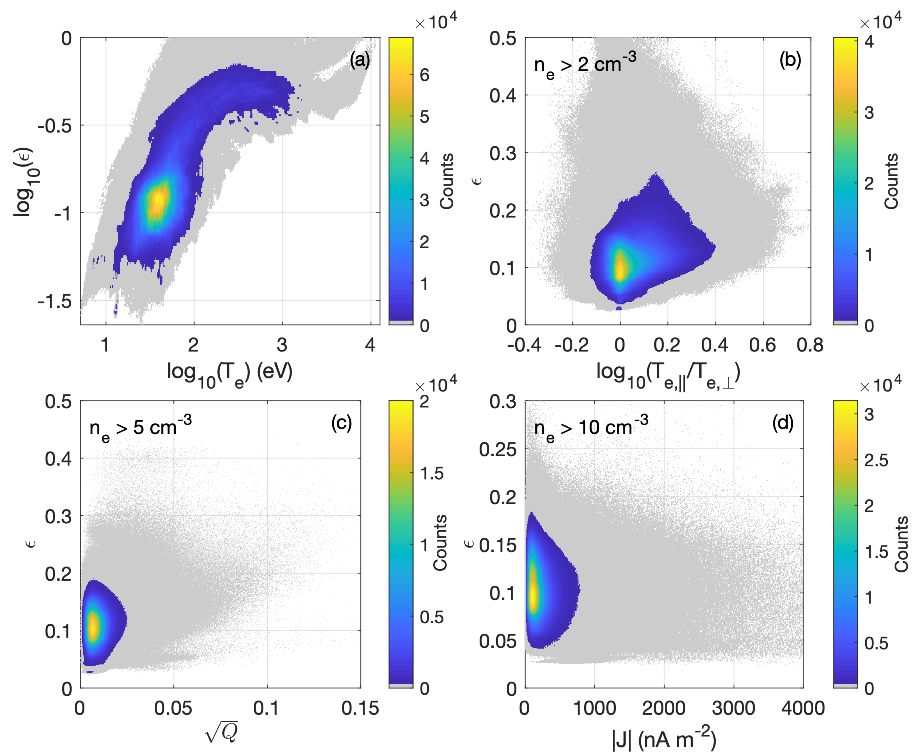

Figure 4. Two-dimensional histograms of ϵ versus different plasma conditions. (a) $\log_{10}\epsilon$ versus $\log_{10} T_e$. (b) ϵ versus $\log_{10} T_{e,\|}/T_{e,\perp}$ for $n_e > 2$ cm^{-3}. (c) ϵ versus agyrotropy measure $\sqrt{Q}$ for $n_e > 5$ cm^{-3}. (d) ϵ versus $|\mathbf{J}|$ for $n_e > 2$ cm^{-3}.

hance ϵ above background values. Similarly, we do not find any correlation between ϵ and $\mathbf{E} \cdot \mathbf{J}$ (not shown). Overall, aside from ϵ scaling with T_e due to the correlation between T_e and n_e, there is little statistical dependency of ϵ on the local plasma conditions.

To further investigate the relationship between ϵ and n_e and T_e we plot the 2D histogram of n_e and T_e in Figure 5a. We see that there is a statistical increase in T_e as n_e decreases, as expected from electron distributions in the outer magnetosphere, magnetopause, and in the magnetosheath. However, for a given n_e there is a large range of T_e, in particular for $n_e \lesssim 1$, corresponding to the outer magnetosphere. This larger range of T_e in the magnetosphere can result from the relative densities of cold and hot components n_c and n_h varying significantly. In Figures 5b and 5c we plot the mean and standard deviation of ϵ versus n_e and T_e. These values are computed on the same grid as in Figure 5a, so Figure 5a indicates the number of values used to calculate each mean and standard deviation. Figure 5b shows the strong dependence of ϵ on n_e, as well as a weaker dependence on T_e. In particular, the mean ϵ increases as T_e increases for a given n_e. This is likely in part due to the lowest energy part of the electron distribution being excluded to avoid contamination from internal photoelectrons and spacecraft charging effects. Figure 5c shows that the standard deviation of ϵ tends to increase with decreasing n_e and increasing T_e. This might correspond to more variable electron distributions in the outer magnetosphere.

We now investigate the relationship between the parallel electron plasma β, $\beta_{e,\parallel}$, and $T_{e,\parallel}/T_{e,\perp}$ and the instability of these electron distributions. In Figure 5d we plot the 2D histogram of $T_{e,\parallel}/T_{e,\perp}$ and $\beta_{e,\parallel}$. We find that for $\beta_{e,\parallel} \lesssim 1$ there is a wide range of $T_{e,\parallel}/T_{e,\perp}$, although most data are found near $T_{e,\parallel}/T_{e,\perp} = 1$. For $\beta_{e,\parallel} \gtrsim 1$ the range of $T_{e,\parallel}/T_{e,\perp}$ decreases as $\beta_{e,\parallel}$ increases.

We can compare this histogram with the thresholds for the oblique resonant electron firehose instability [*Li and Habbal*, 2000] and the whistler temperature anisotropy instability [*Kennel and Petschek*, 1966]. The oblique electron firehose instability can occur in a high $\beta_{e,\parallel}$ plasma with $T_{e,\parallel}/T_{e,\perp} > 1$. Theoretical work has shown that the oblique resonant electron firehose instability has a lower threshold than the field-aligned non-resonant electron fireshose instability [*Li and Habbal*, 2000], so we only consider the former case here. The whistler temperature anisotropy instability can occur for $T_{e,\parallel}/T_{e,\perp} < 1$. These instabilities are proposed to constrain the values of $T_{e,\parallel}/T_{e,\perp}$ that can develop by pitch-angle scattering electrons so the electron distribution becomes more isotropic. Numerical studies

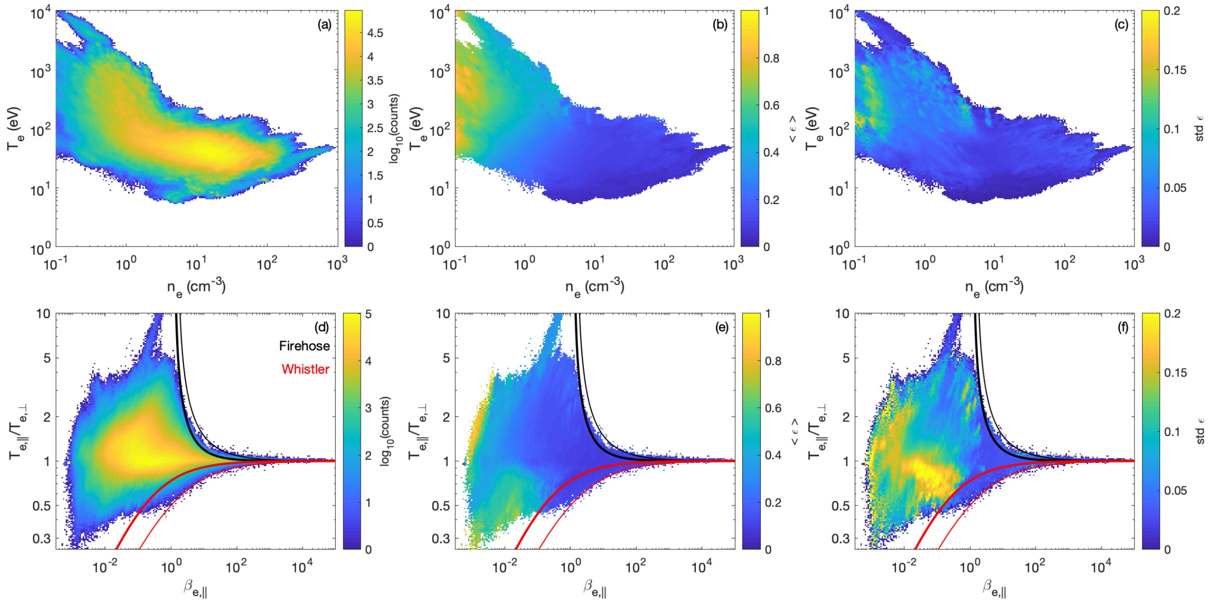

Figure 5. Two-dimensional plots of counts and ϵ versus T_e and n_e, and $T_{e,\parallel}/T_{e,\perp}$ and ϵ. (a) Two-dimensional histograms of T_e versus n_e. (b) Mean ϵ versus T_e and n_e. (c) Standard deviation of ϵ versus T_e and n_e. (d) Two-dimensional histogram of $T_{e,\parallel}/T_{e,\perp}$ versus $\beta_{e,\parallel}$. (e) Mean ϵ versus $T_{e,\parallel}/T_{e,\perp}$ versus $\beta_{e,\parallel}$. (f) Standard deviation of ϵ versus $T_{e,\parallel}/T_{e,\perp}$ versus $\beta_{e,\parallel}$.

have shown that the threshold $T_{e,\parallel}/T_{e,\perp}$ for these instabilities scales with $\beta_{e,\parallel}$ and has the form [*Gary and Wang*, 1996]

$$\frac{T_{e,\parallel}}{T_{e,\perp}} = \left(1 + S_e \beta_{e,\parallel}^{-\alpha_e}\right)^{-1}, \tag{6}$$

where S_e and α_e are constants. We consider the thresholds corresponding to growth rates $\gamma/\Omega_{ce} = 0.01$ and 0.1. For the electron firehose instability we use $S_e = -1.23$ and $\alpha_e = 0.88$, and $S_e = -1.32$ and $\alpha_e = 0.61$ for $\gamma/\Omega_{ce} = 0.01$ and 0.1, respectively [*Gary and Nishimura*, 2003]. For the whistler instability we use $S_e = 0.36$ and $\alpha_e = 0.55$, and $S_e = 1.0$ and $\alpha_e = 0.49$ for $\gamma/\Omega_{ce} = 0.01$ and 0.1, respectively [*Gary and Wang*, 1996]. These thresholds are plotted in Figures 5d–5f, where the black and red curves correspond to the firehose and whistler thresholds, respectively. The thick lines correspond to $\gamma/\Omega_{ce} = 0.01$ and the thin lines correspond to $\gamma/\Omega_{ce} = 0.1$.

For $T_{e,\parallel}/T_{e,\perp} > 1$ the firehose instability for $\gamma/\Omega_{ce} = 0.01$ provides an approximate boundary for the largest $T_{e,\parallel}/T_{e,\perp}$ for $\beta_{e,\parallel} \gtrsim 2$. Only 0.016 % of the data exceed the $\gamma/\Omega_{ce} = 0.01$ threshold, so regions unstable to the firehose instability are very rare. For $\beta_{e,\parallel} \lesssim 2$ the threshold for the firehose instability is much larger than any observed

$T_{e,\parallel}/T_{e,\perp}$. This means that for $\beta_{e,\parallel} \lesssim 2$, such as on the magnetospheric side of the magnetopause and in the magnetosphere, the firehose instability is unlikely to occur, and thus cannot limit the values of $T_{e,\parallel}/T_{e,\perp}$ found there. Regions where the firehose instability is more likely to occur are in the magnetosheath, and potentially at the magnetopause boundary and in reconnection regions, where the magnetic field **B** becomes very small.

For $T_{e,\parallel}/T_{e,\perp} < 1$ the whistler temperature anisotropy instability provides an approximate boundary for $\beta_{e,\parallel} \gtrsim 0.1$ for the allowable $T_{e,\parallel}/T_{e,\perp}$. For the $\gamma/\Omega_{ce} = 0.01$ threshold approximately 0.12 % of the data exceed the threshold, nearly an order of magnitude higher than for the firehose instability. We find that for $\beta_{e,\parallel} \gtrsim 1$ the cutoff in the observed data matches the $\gamma/\Omega_{ce} = 0.1$ threshold very well. This might suggest that the maximum growth rate for whistlers near the magnetopause and in the magnetosheath is $\gamma/\Omega_{ce} = 0.1$.

We note that the thresholds for the whistler and firehose instabilities are based on an electron bi-Maxwellian distribution function. Thus, a large deviation of the observed distribution from a bi-Maxwellian distribution may invalidate the threshold predictions. In Figures 5e and 5f we plot the mean and standard deviation of ϵ as functions of $T_{e,\parallel}/T_{e,\perp}$ and $\beta_{e,\parallel}$. Figure 5e shows that when $T_{e,\parallel}/T_{e,\perp}$ approaches or exceeds the whistler and firehose thresholds the values of ϵ remain relatively small. This suggests that the thresholds are reasonable indicators of instability. Figure 5f shows that the standard deviation is relatively small when the thresholds are exceeded, although there are regions with enhanced standard deviations close to both the firehose and whistler instabilities. This might indicate that some distributions in these regions may be unstable.

For magnetosheath plasma, electron distributions often exhibit flat-top distribution functions so they will often differ from a bi-Maxwellian, producing a finite ϵ. It is unclear to what to what extent such distributions affect the firehose and whistler thresholds, although the good agreement between the threshold conditions and the cutoff in the observed data suggests that the numerical thresholds for the instabilities are reasonable. For magnetospheric plasmas previous observations have shown that non-Maxwellian distributions develop. One example is the magnetospheric plasmas consist of both hot and cold electron distributions, which will modify the threshold for whistler waves [e.g. *Gary et al.*, 2012]. Similarly, in the magnetospheric separatrices of reconnection complex electron distributions develop, which can excite whistler waves [*Graham et al.*, 2016b; *Khotyaintsev et al.*, 2019]. Thus, we expect that whistlers can be generated if they do not exceed the threshold conditions due to the deviations from the bi-Maxwellian distribution function. It is unclear if deviations from a bi-Maxwellian distributions can enhance the instability of the oblique electron firehose instability.

5 Case studies

Using the results in Figure 2, we can use the statistical percentiles of ϵ as a function of n_e to find regions of localized enhanced or reduced ϵ and investigate their source regions. We specifically focus on the magnetic reconnection ion and electron diffusion regions, the bowshock, and the turbulent magnetosheath.

5.1 Ion Diffusion Region

We investigate the ion diffusion region (IDR) observed 2015 December 30 by *Graham et al.* [2016a] at Earth's dayside magnetopause. The IDR was identified by a strong Hall electric field and intense parallel electron heating. Figure 6 provides an overview of the electron behavior for this event from MMS1. The spacecraft crossed the magnetopause from the magnetosphere to the magnetosheath, indicated by the reversal in the magnetic field $\mathbf{B}$ and substantial increase in n_e (Figures 6a and 6b). At the magnetopause, we see large fluctuations in the electron bulk velocity $\mathbf{V}_e$ (Figure 6c), intense parallel electron heating (Figure 6f), and an increase in $\sqrt{Q}$ (Figure 6g). We find that $\sqrt{Q}$ peaks at 0.06 near the center of the current sheet, which may indicate close proximity to the EDR. The peak in electron heating was observed on the magnetospheric side of the magnetopause in the magnetospheric inflow region next to the Hall region, where ions decouple from the electron motion [*Graham et al.*, 2016a]. Here $\beta_{e,\|}$ is low so the peak $T_{e,\|}/T_{e,\perp} = 3.9$ is well below the threshold for the electron firehose instability. Therefore, the electron firehose instability cannot limit the magnitude of $T_{e,\|}/T_{e,\perp}$ found in the magnetopause current sheet. On the magnetosheath side of the current sheet we find that some short intervals have $T_{e,\|}/T_{e,\perp} < 1$ that exceed the whistler temperature anisotropy instability, and find that there are whistler waves in these regions (not shown).

The electron non-Maxwellianity ϵ is plotted in Figure 6h. Overall, we find that ϵ decreases from about 0.2 to about 0.1 from the magnetosphere to the magnetosheath. This is due primarily to the change in n_e, so it is difficult to identity regions of enhanced non-Maxwellianity by simply plotting ϵ. Using the measured n_e we calculate the 10th, 50th

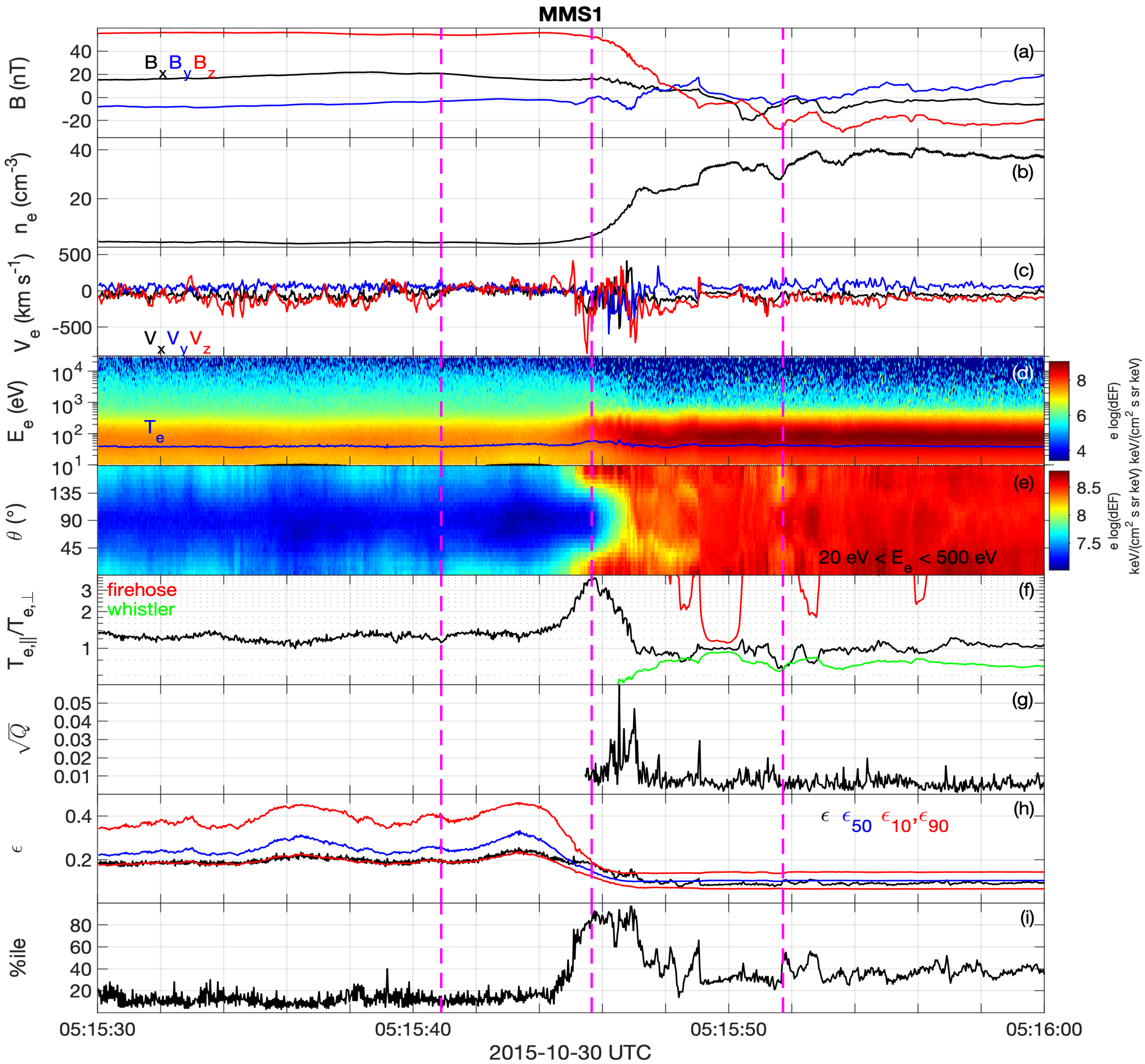

Figure 6. Overview of the electron behavior from MMS1 associated with the ion diffusion region observed on 2015 October 30. (a) **B**. (b) n_e. (c) $\mathbf{V}_e$. (d) Electron omnidirectional differential energy flux (blue line indicates T_e). (e) Spectrogram of the electron pitch-angle distribution for energies 20 eV $<$ E $<$ 500 eV. (f) $T_{e,\|}/T_{e,\perp}$ (black), and firehose (red) and whistler (green) thresholds (for $\gamma/\Omega_{ce} = 0.01$). (g) $\sqrt{Q}$. (h) ϵ (black), and the 10th and 90th percentiles of ϵ as a function of n_e (red) and median ϵ as a function n_e. (i) Percentile of the observed ϵ as a function of n_e. The magenta dashed lines indicate the times the electron distributions in Figure 1 are taken.

(median), and 90th percentiles of ϵ, ϵ_{10}, ϵ_{50}, and ϵ_{90}, respectively, from the statistical results in Figure 2c. These quantities are plotted in Figure 6h. In the magnetosphere (low density) we find that ϵ remains close to ϵ_{10}, indicating that statistically the distribution is close to Maxwellian for a magnetospheric distribution. In this case there is only a single colder electron population with $T_e \approx 40$ eV, and negligible hot electrons. This results in the relatively low ϵ observed in the magnetosphere. In the magnetosheath (high density) ϵ has values between ϵ_{10} and ϵ_{50}, suggesting that while the electron distributions are non-Maxwellian, but the non-Maxwellianity is not particularly large. However, in the IDR where large $T_{e,\parallel}/T_{e,\perp}$ occurs there is an increase in $\sqrt{Q}$, and ϵ approaches and exceeds ϵ_{90}, meaning that statistically the non-Maxwellianity is high in this region. This is most clearly seen in Figure 6i, where we plot the percentile that the observed ϵ belongs to as a function of n_e based on the statistical results in Figure 2c. We find that the percentile increases where $T_{e,\parallel}/T_{e,\perp}$ and $\sqrt{Q}$ peak, while in the magnetosphere the percentile is low and in the magnetosheath the percentile remains close to 50. The magenta dashed lines in Figure 6 indicate the times of the three electron distributions in Figure 1. The source of the increased ϵ in the ion diffusion region is the flat-top shape of the distribution parallel and antiparallel to **B** (Figure 1d). Figure 1 shows that the shapes of the magnetospheric and magnetosheath distributions in the thermal energy range deviate from a bi-Maxwellian distribution.

These results indicate that calculating ϵ alone is not sufficient to identify regions of unusually large non-Maxwellianity when considering magnetopause crossings. However, using the statistical results derived from Figure 2c, we can identify regions where the calculated ϵ correspond to unusually large deviations from a bi-Maxwellian distribution function. For this example enhanced deviations in the electron distributions from a bi-Maxwellian are found in the ion diffusion region of asymmetric reconnection, although there is little change in the value of ϵ across the magnetopause.

5.2 Electron Diffusion Region

As an exampe of an EDR crossing, Figure 7 shows the magnetopause crossings observed on 2015 October 22 by MMS1 [*Phan et al.*, 2016; *Toledo-Redondo et al.*, 2016]. The EDR is observed at 06:05:22 UT, indicated by the yellow-shaded region in Figure 7. Over the entire interval we observe three partial magnetopause crossings, where B_z decreases and n_e increases (Figures 7a and 7b). Between the first and second magnetopause crossings there is a southward ion outflow and after the third magnetopause crossing, where the EDR is observed, there is a northward outflow. The spacecraft enters the magnetosheath at approximately 06:05:35 UT. The outflows are here indicated by the large-scale changes in the electron flow $V_{e,z}$ in Figure 7c. In the magnetosphere T_e is very low due to cold electrons dominating the electron distributions (Figure 7d). The electron pitch-angle distribution in Figure 7e shows that there are complex changes in the electron distribution functions across the magnetopause boundaries. Similarily, $T_{e,\|}/T_{e,\perp}$ varies significantly across the interval (Figure 7f). At the third magnetopause crossing we observe the largest $\mathbf{V}_e$ (Figure 7c) and $\sqrt{Q}$ (Figure 7g), which peaks just above 0.1, signifying the EDR.

In Figure 7h we plot the timeseries of ϵ, as well as ϵ_{10}, ϵ_{50}, and ϵ_{90}. We note that after the first magnetopause crossing ϵ_{10}, ϵ_{50}, and ϵ_{90} remain relatively constant. In the EDR we find a large enhancement in ϵ (well above ϵ_{90}), which is colocated with the peak in $\sqrt{Q}$. For this event we also observe very large enhancements in ϵ in both the northward and southward ion outflows (both have extended regions where $\epsilon > \epsilon_{90}$). Indeed the largest ϵ is observed in the northward reconnection outflow, rather than at the EDR. Here, $\sqrt{Q}$ is negligible so these deviations from bi-Maxwellianity are gyrotropic in nature. This event illustrates why there is statistically a lack of correlation between ϵ and $\sqrt{Q}$.

In Figure 7f we compare $T_{e,\|}/T_{e,\perp}$ with the local electron firehose and whistler thresholds. Throughout the interval $T_{e,\|}/T_{e,\perp}$ remains below the threshold of the electron firehose instability. For the whistler instability we find that in some regions $T_{e,\|}/T_{e,\perp}$ exceeds the threshold. Figure 7i, which shows the frequency-time spectrogram of $\mathbf{B}$, showing that whistler waves are found near these regions. However, whistlers are found where $T_{e,\|}/T_{e,\perp}$ does not satisfy the threshold for instability, such as in the magnetosphere and throughout the northward outflow. In the magnetosphere we observe distinct hot and cold electron populations (Figure 7d), where the cold population is characterized by $T_{e,\|}/T_{e,\perp} > 1$, resulting in the overall distribution having $T_{e,\|}/T_{e,\perp} > 1$, while the hot population with energies $E > 1$ keV has $T_{e,\|}/T_{e,\perp} < 1$, which is the likely source of the whistler waves. In this case we estimate $n_h/n_c \approx 3 \times 10^{-3}$, meaning that the hot component has only a small effect on ϵ. In the outflow we observe complex electron distributions (an example is shown below in Figure 8). Therefore, in these regions there tends to be a significant ϵ, so the whistler instability thresholds predicted from a single bi-Maxweliian distribution are no longer valid.

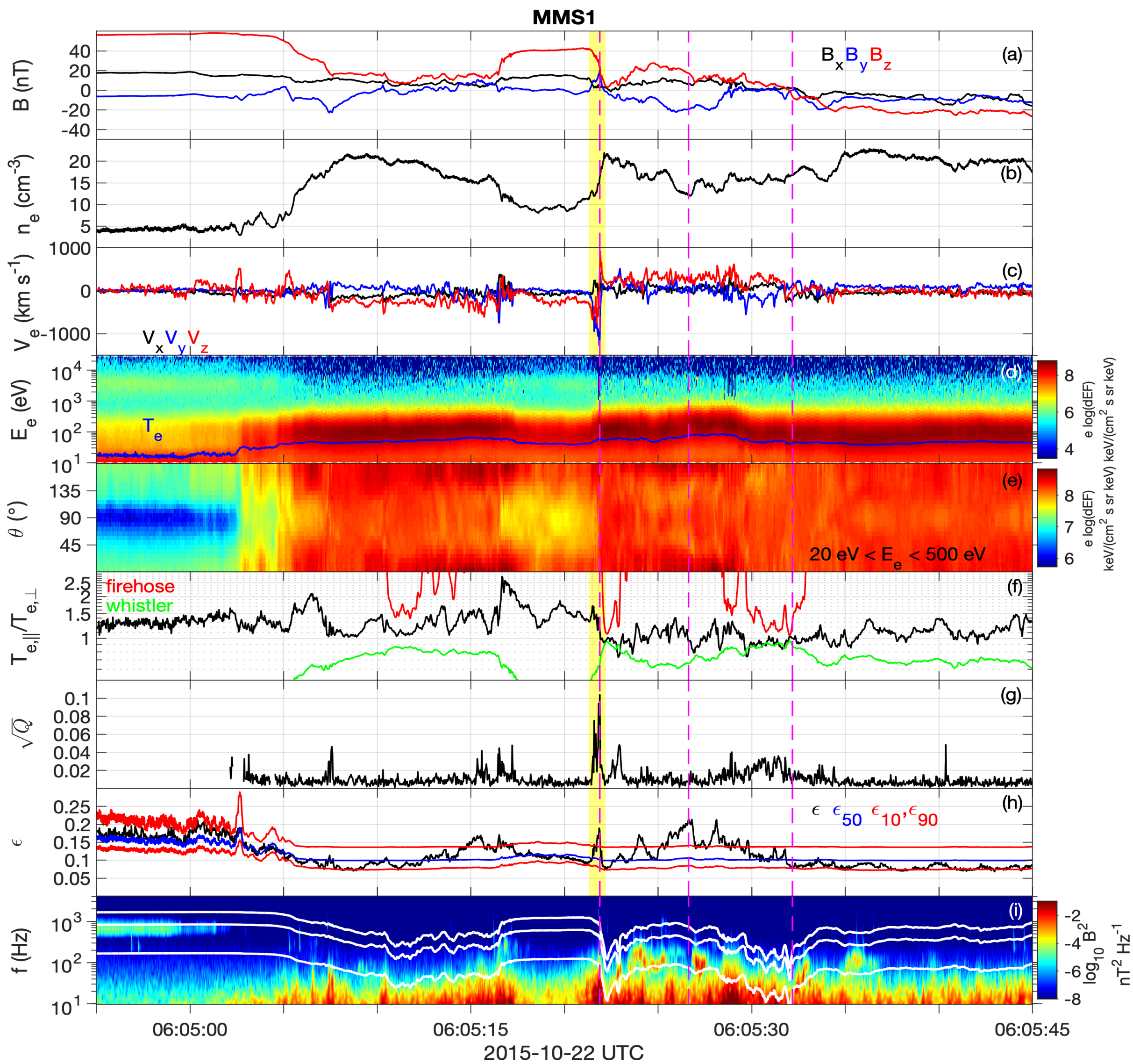

Figure 7. Overview of the electron behavior from MMS1 associated with the electron diffusion region observed on 2015 October 22. (a) **B**. (b) n_e. (c) $\mathbf{V}_e$. (d) Electron omnidirectional differential energy flux (blue line indicates T_e). (e) Spectrogram of the electron pitch-angle distribution for energies $20\,\text{eV} < E < 500\,\text{eV}$. (f) $T_{e,\parallel}/T_{e,\perp}$ (black), and firehose (red) and whistler (green) thresholds (for $\gamma/\Omega_{ce} = 0.01$). (g) $\sqrt{Q}$. (h) ϵ (black), and the 10th and 90th percentiles of ϵ as a function of n_e (red) and median ϵ as a function n_e. (h) Percentile of the observed ϵ as a function of n_e.

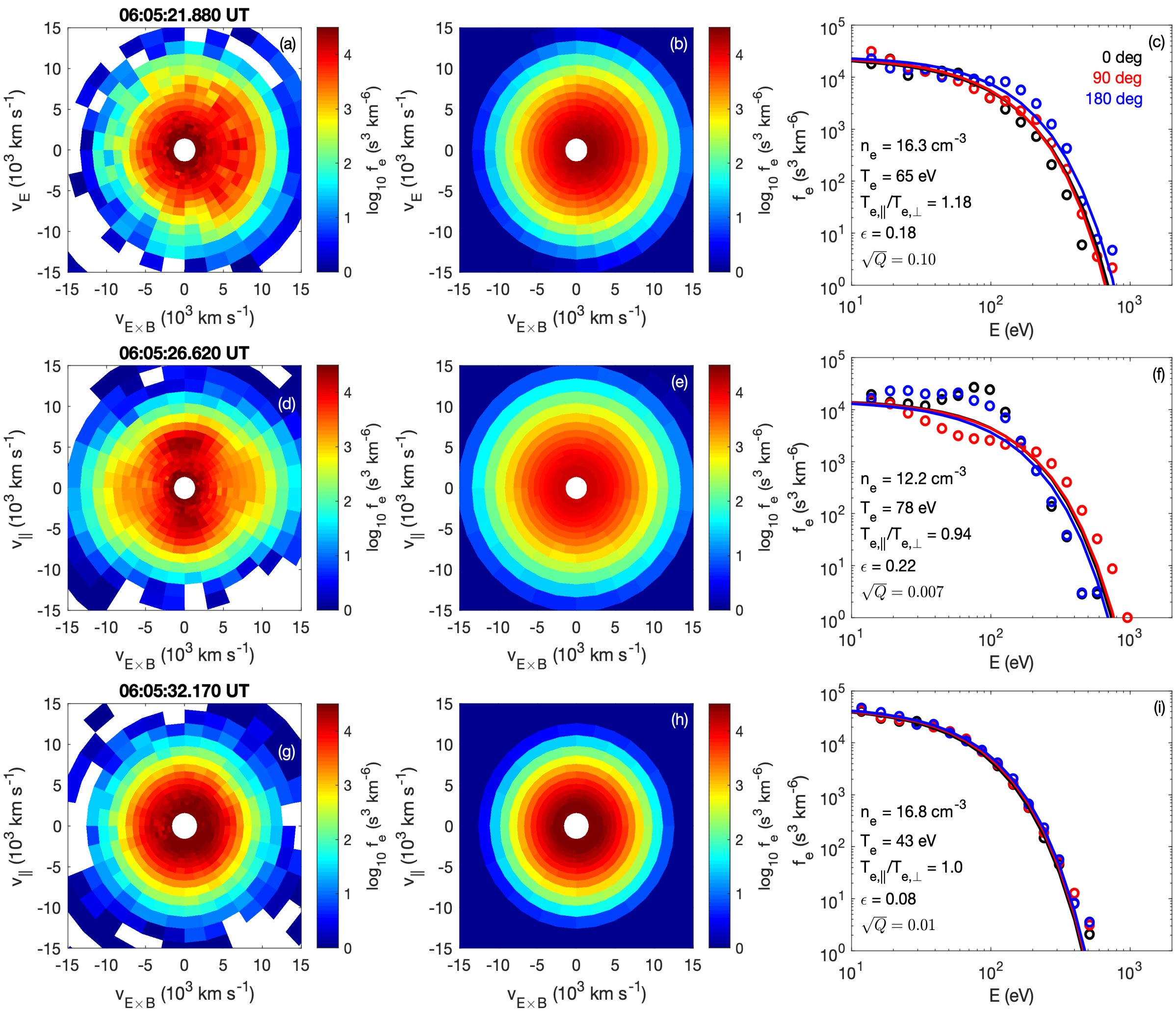

Figure 8. Three examples of electron distributions and the predicted bi-Maxwellian distribution based on the electron moments from the EDR crossing observed by MMS1 on 22 October 2015. Panels (a), (d), and (g) show a two-dimensional slice of the observed three-dimensional electron distribution in the **B** and **E**×**B** plane. Panels (b), (e), and (h) show the modeled bi-Maxwellian distributions in the same plane. Panels (c), (f), and (i) show the phase-space densities at pitch angles 0° (black), 90° (red), and 180° (blue) for the observed distributions (circles) and modeled bi-Maxwellian (solid lines). The distribution in panels (a)–(c) is in the EDR where $\sqrt{Q}$ peaks, (d)–(f) is in the ion outflow where ϵ peaks, (g)–(i) is close to the magnetosheath where ϵ is small. The electron distribution properties and ϵ of the three distributions are given in panels (c), (f), and (i).

In Figure 8 we investigate three electron distributions observed in the EDR where $\sqrt{Q}$ peaks (Figures 8a–8c), in the reconnection outflow where ϵ peaks (Figures 8d–8f), and a point in the ouflow where ϵ is small (Figures 8g–8i). These points are indicated by the three dashed magenta lines in Figure 7. Figure 8a shows a distribution consisting of a near-stationary core and a crescent propagating in the $\mathbf{E} \times \mathbf{B}$ direction, which is responsible for the peak in $\sqrt{Q}$ and the large $\mathbf{V}_e$. Such distributions are typical of EDRs at the magnetopause [*Burch et al.*, 2016; *Graham et al.*, 2017; *Norgren et al.*, 2016]. As expected the model distribution does not capture the observed features, and is simply a bi-Maxwellian drifting in the $\mathbf{E} \times \mathbf{B}$ direction, which results in the enhanced ϵ. Note that the pitch-angle distribution (Figure 8c) does not capture the agyrotropy, so in this plot the source of ϵ becomes unclear.

In Figure 8d the observed distribution prominantly feaatures counter-streaming electron beams parallel and antiparallel to $\mathbf{B}$, and higher-energy electrons perpendicular to $\mathbf{B}$. For electron energies $E \lesssim 200\,\mathrm{eV}$ the counter-streaming result in $T_{e,\|}/T_{e,\perp} > 1$, while for $E \gtrsim 200\,\mathrm{eV}$ we find $T_{e,\|}/T_{e,\perp} < 1$. The total $T_{e,\|}/T_{e,\perp}$ is close to 1, so the model distribution is approximately Maxwellian (Figure 8e). Figure 8f shows that f_e at pitch angles 0°, 90°, and 180° all differ significantly from f_{model} and as a result ϵ is relatively large. These distributions can account for the observed whistler waves, where $T_{e,\|}/T_{e,\perp}$ does not satisfy the instability threshold.

The distribution in Figure 8g is close to Maxwellian and very similar to f_{model} (Figure 8h). Figure 8i shows that the profiles of f_e at $\theta = 0°$, 90°, and 180° match well f_{model}, so the distribution is approximately Maxwellian. Figures 7 and 8 show that the shape electron distributions can vary significantly throughout the reconnection outflow, with both complex distributions and approximately Maxwellian distributions developing.

More generally we have investigated the non-Maxwellianity of the electron distributions associated with the 11 EDRs observed in the first phase of the MMS mission [*Fuselier et al.*, 2017; *Webster et al.*, 2018]. We find that in each case there is an enhancement in ϵ in or near the EDR, which typically exceeds ϵ_{90}. In some outflow regions large ϵ are observed, although the values of ϵ, and whether these values exceed ϵ_{90}, varies between events. This suggests that large values of ϵ are a necessary, but not sufficient criterion for identification of EDRs.

5.3 Bowshock

In this subsection we investigate the non-Maxwellianity of electron distributions at the bowshock. In particular, we investigate a quasi-perpendicular bowshock in detail. We find that ϵ is strongly enhanced at the bowshock but typically returns to nominal values within the magnetosheath. Figure 9 shows an example of a quasi-perpendicular bowshock observed on 04 November 2015 around 05:58:00 UT. This bowshock was previously studied by *Oka et al.* [2017]. At this time the spacecraft were located at [10.4, 2.1, -0.5] R_E (GSE). For this shock we estimate the shock-normal angle to be $\theta_{Bn} = 83°$, corresponding to a quasi-perpendicular shock, and the Alfven Mach number is $M_A \approx 11$. Based on the width of the shock foot we estimate that the shock moves ~ 30 km s^{-1} Sunward in the spacecraft frame.

Figure 9 shows that the spacecraft was initially in a solar wind-like plasma, with low **B**, fast Earthward flow $V_{e,x} = -700$ km s^{-1}, and density $n_e = 7.1$ cm^{-3}. We see that the electron fluxes vary near 100 eV and observe large-amplitude emission of Langmuir waves at the local plasma frequency (not shown), indicating that the spacecraft is in the electron foreshock region. The shock foot begins at approximately 05.58:00 UT, and is seen as the increase in n_e and $|B_y|$, and the decrease in $|V_{e,x}|$. The shock ramp begins at approximately 05:58:14 UT, and a series of shock ripples are observed in **B** and n_e. The overshoot is observed at 05:58:19 UT.

In Figure 9g we plot ϵ along with ϵ_{10}, ϵ_{50}, and ϵ_{90}. At the beginning of the interval ϵ is very low, but increases beginning at 05:57:46 UT. At this time ϵ likely varies because the spacecraft is in the electron foreshock, where electrons reflected and accelerated at the bowshock can cause ϵ to increase above the values in the unperturbed solar wind. In the shock foot ϵ begins to exceed ϵ_{90}, which extends for about 13 seconds until just after the shock ramp (yellow-shaded interval in Figure 9). Based on the shock speed this region of enhanced ϵ has a spatial scale of $\sim$ 400 km, which corresponds to $2\rho_i$ or 5 d_i based on the magnetosheath parameters, where ρ_i and d_i are the ion Larmor radius and ion inertial length, respectively. Thus, the region of enhanced ϵ extends over ion spatial scales. Downstream of the shock ϵ typically remains between ϵ_{10} and ϵ_{50}, with some local enhancements in ϵ. Throughout this region we observe rapid fluctuations in $T_{e,\parallel}/T_{e,\perp}$, although $T_{e,\parallel}/T_{e,\perp}$ does not exceed the threshold for the firehose instability and rarely satisfies the threshold for whistler waves.

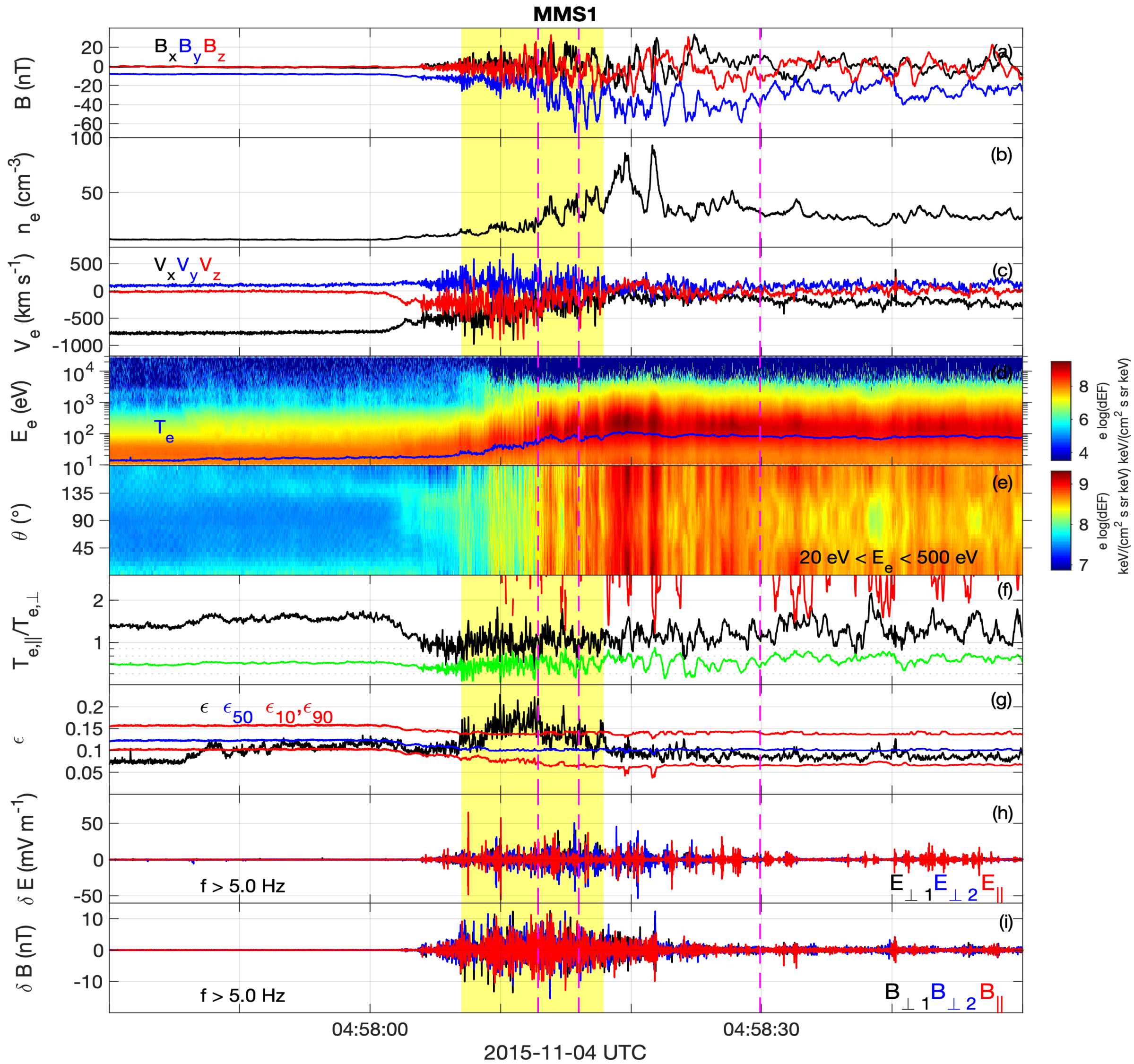

Figure 9. Overview of the electron behavior from MMS1 associated a bowshock crossing observed on 2015 November 4 observed by MMS1. (a) **B**. (b) n_e. (c) $\mathbf{V}_e$. (d) Electron omnidirectional differential energy flux (blue line indicates T_e). (e) Spectrogram of the electron pitch-angle distribution for energies $20\,\mathrm{eV} < E < 500\,\mathrm{eV}$. (f) $T_{e,\parallel}/T_{e,\perp}$ (black), and firehose (red) and whistler (green) thresholds (for $\gamma/\Omega_{ce} = 0.01$). (g) ϵ (black), and the 10th and 90th percentiles of ϵ as a function of n_e (red) and median ϵ as a function n_e. (h) Fluctuating electric field $\delta\mathbf{E}$ above $f = 5\,\mathrm{Hz}$ in field-aligned coordinates. (i) Fluctuating magnetic field $\delta\mathbf{B}$ above $f = 5\,\mathrm{Hz}$ in field-aligned coordinates.

In Figures 9h and 9i we plot the fluctuating electric and magnetic fields, $\delta\mathbf{E}$ and $\delta\mathbf{B}$, in field-aligned coordinates above 5 Hz. The region of enhanced ϵ coincides with the most intense $\delta\mathbf{E}$ and $\delta\mathbf{B}$. Fluctuations both parallel and perpendicular to the background magnetic field are observed. For $\delta\mathbf{E}$ the parallel fluctuations are typically observed near the ion plasma frequency f_{pi}, while the perpendicular fluctuations are observed at lower frequencies. The magnetic field fluctuations are primarily seen at low frequencies below the lower hybrid frequency. In the magnetosheath $\delta\mathbf{B}$ are significantly reduced, while $\delta\mathbf{E}$ parallel to the background magnetic field continue to be observed intermittently. The large-amplitude electrostatic and electromagnetic fluctuations in the bowshock may result in the electron distribution with large ϵ becoming more Maxwellian in the magnetosheath due to wave-particle interactions.

In Figure 10 we plot three electron distributions at the times indicated by the magenta dashed lines in Figure 9 and compare these distributions with the modeled bi-Maxwellian distribution function. The distributions are observed in the shock foot [panels (a)–(c)], near the shock ramp [panels (d)–(f)], and in the magnetosheath [panels (g)–(i)]. In each observed distribution there is a super-thermal tail in the electron distribution. However, these tails do not significantly increase ϵ because the phase-space densities are very low, meaning their contributions to T_e and n_e are negligible.

The electron distribution in Figure 10a exhibits a dense low-energy electron beam parallel to $\mathbf{B}$, associated with accelerated solar wind electrons. For the direction antiparallel to $\mathbf{B}$ the electrons are hotter than in the parallel direction. These features are not captured by the bi-Maxwellian distribution (Figure 10b), resulting in a relatively large ϵ. Figure 10c shows that the shape of the observed electron distribution differs greatly from the bi-Maxwellian distribution, consistent with ϵ being unusually large. Figure 10d shows an electron distribution near the ramp, where shock ripples are observed. The distribution is similar to the one in Figure 10a, except the solar wind electrons have been further accelerated parallel to $\mathbf{B}$ and now occupy a smaller range of pitch angles. At $\theta = 90^\circ$, and 180° we observe flat-top like distributions, as previously observed at quasi-perpendicular shocks [*Feldman et al.*, 1982; *Scudder*, 1995]. Here, ϵ is reduced from the distribution in Figure 10a, but remains well above the statistical median. These distributions consisting of a beam of accelerated solar wind electrons and flat-top-like distributions have been observed previously and are due to the cross-shock potential in the deHoffman-Teller frame. By integrating the divergence of the electron pressure divergence over position, we esti-

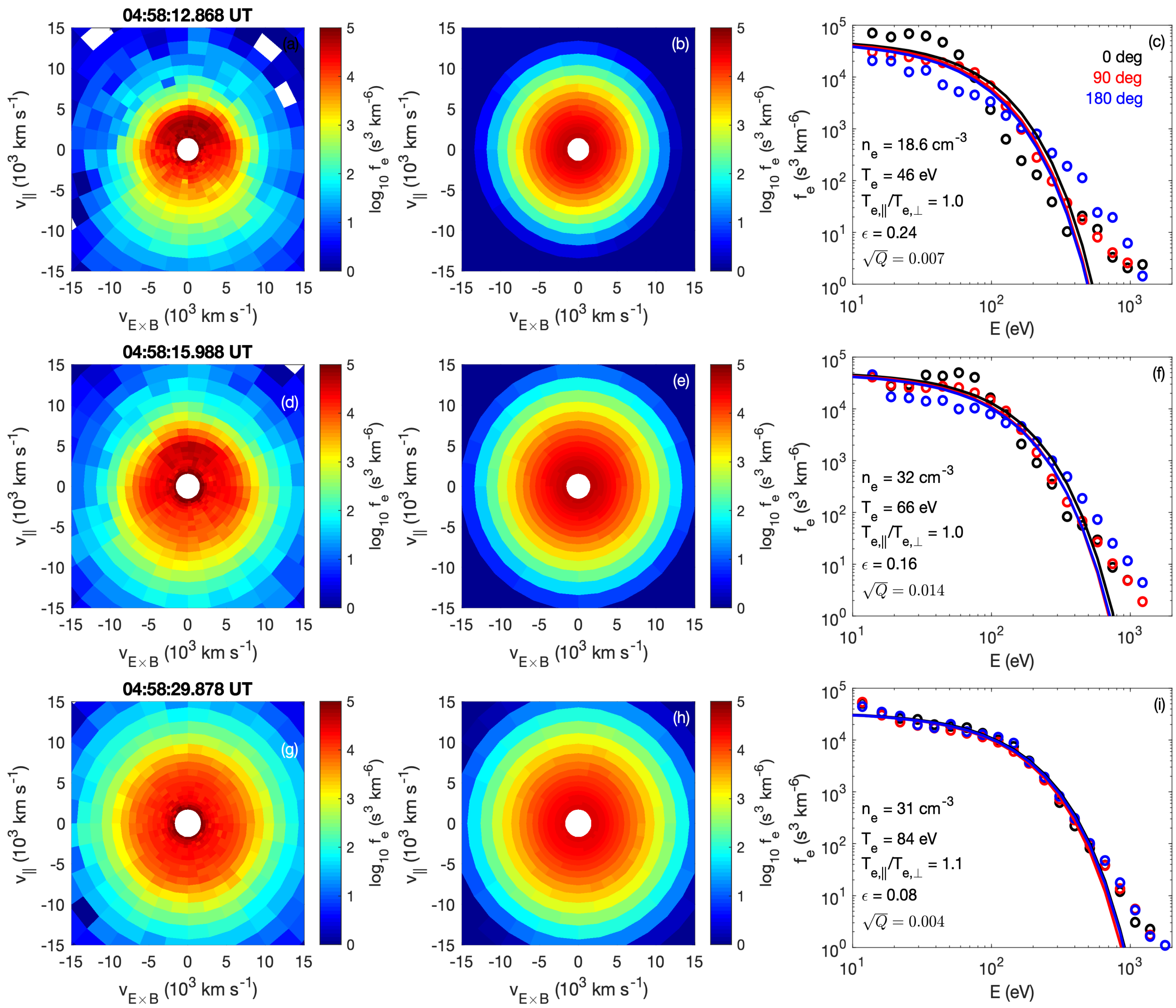

Figure 10. Three examples of electron distributions and the modeled bi-Maxwellian distribution based on the electron moments from the foreshock crossing observed by MMS1 on 04 November 2015. Panels (a), (d), and (g) show a two-dimensional slice of the observed three-dimensional electron distribution in the **B** and **E** $\times$ **B** plane. Panels (b), (e), and (h) show the modeled bi-Maxwellian distributions in the same plane. Panels (c), (f), and (i) show the phase-space densities at pitch angles 0° (black), 90° (red), and 180° (blue) for the observed distributions (circles) and modeled bi-Maxwellian (solid lines). The distribution in panels (a)–(c) is in the shock foot, (d)–(f) is near the shock ramp, (g)–(i) is in the magnetosheath behind the bowshock. The electron distribution properties and ϵ of the three distributions are given in panels (c), (f), and (i).

mate a maximum cross-shock potential of $\sim$ 300 V, which is several times larger than the maximum energy of the beam of solar wind electrons in the shock and the energies where the distribution is relatively flat $E \lesssim 100$ eV.

In the magnetosheath behind the bowshock the electrons are close to Maxwellian, for example the electron distribution in Figures 10g–10i. In these panels we see little deviation from a Maxwellian distribution function. We conclude that the strongly enhanced ϵ occur at ion spatial scales across the shock. Behind the shock in the magnetosheath ϵ is significantly reduced, but continues to vary with position.

5.4 Turbulent Magnetosheath

In this subsection we investigate a region of magnetosheath turbulence behind the quasi-parallel bowshock. Figure 11 provides an overview of the region observed by MMS1 on 25 October 2015. The interval is characterized by multiple current sheets, as indicated by reversal in $\mathbf{B}$ (Figure 11a), and narrow enhancements in $\mathbf{J}$ (Figure 11c). Figure 11d shows that T_e remains relatively constant, although there are some variations in the electron fluxes. Figure 11e and 11f that $T_{\|}/T_{\perp}$ varies across the interval, with $T_{\|}/T_{\perp}$ ranging from 1 to 2. We find that the whistler and firehose thresholds for instability are not satisfied in this interval. Throughout the interval $\sqrt{Q}$ remains relatively small, although some enhancements in $\sqrt{Q}$ occur over very short intervals.

In Figure 11h we plot ϵ, along with ϵ_{10}, ϵ_{50}, and ϵ_{90}. In general, ϵ_{10}, ϵ_{50}, and ϵ_{90} remain relatively constant across the entire interval. We find that ϵ varies between 0.05 and 0.17, and peaks in the region of enhanced n_e and $\mathbf{J}$ at 10:49:55 UT. Figure 11i shows that the percentile of ϵ ranges from 1 to 99, meaning the electron distributions vary from very close to Maxwellian to highly non-Maxwellian for magnetosheath conditions. In general, we see no clear correlation between ϵ and the other local plasma parameters. For example, there is no clear consistent correlation with $\mathbf{J}$. At 10:49:55 UT there is a peak in ϵ and $\mathbf{J}$; however, at other times there are peaks in $\mathbf{J}$ without enhanced ϵ (e.g., at 10:49:09 UT), and there are peaks in ϵ where $\mathbf{J}$ is negligible (e.g., at 10:49:16 UT). To illustrate this further, Figure 12 shows the histograms of the entire dataset, with the data from the magnetosheath turbulence interval (from all four spacecraft) overplotted as magenta points. Figure 12a shows a wide range of ϵ observed in this interval and no clear correlation with n_e. Similarly, there is no correlation of ϵ with $T_{\|}/T_{\perp}$ and $\sqrt{Q}$ (Figures 12b and 12c). Fig-

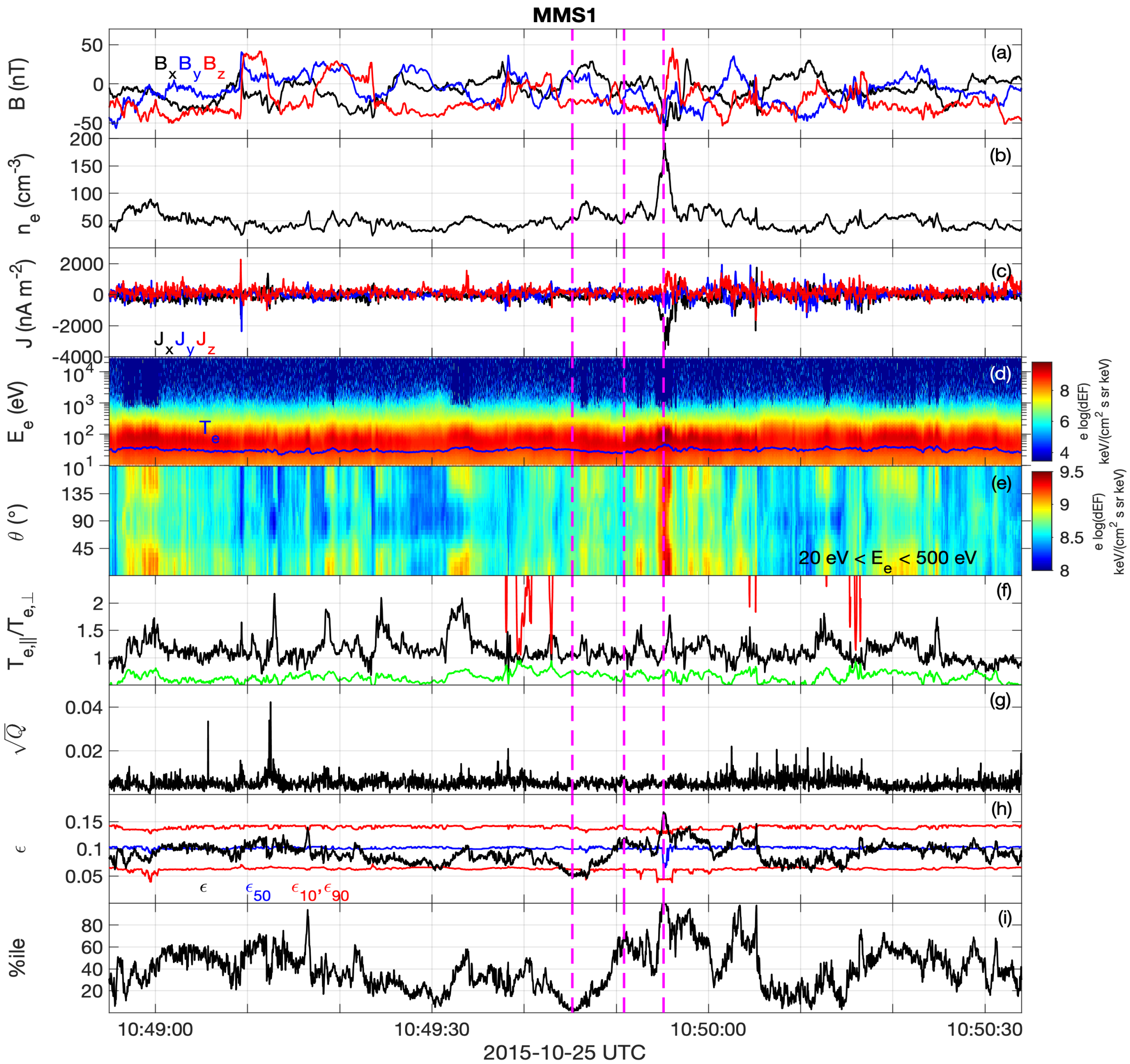

Figure 11. Overview of the electron behavior from MMS1 in the turbulent magnetosheath observed on 2015 October 25 observed by MMS1. (a) **B**. (b) n_e. (c) $\mathbf{V}_e$. (d) Electron omnidirectional differential energy flux (blue line indicates T_e). (e) Spectrogram of the electron pitch-angle distribution for energies 20 eV $<$ E $<$ 500 eV. (f) $T_{e,\|}/T_{e,\perp}$ (black), and firehose (red) and whistler (green) thresholds (for $\gamma/\Omega_{ce} = 0.01$). (h) ϵ (black), and the 10th and 90th percentiles of ϵ as a function of n_e (red) and median ϵ as a function n_e. (i) Percentile of the observed ϵ as a function of n_e.

ure 12d shows there is a slight tendency of ϵ to increase with $\mathbf{J}$, which in this case is due to the region centered around 10:49:55 UT. Overall, there is little clear correlation of ϵ with the local plasma conditions. Other turbulent magnetosheath intervals, such as those investigated in *Yordanova et al.* [2016] and *Voros et al.* [2017] yield qualitatively similar results. We propose that the enhanced non-Maxwellian features may develop at the bowshock, and that the locally observed changes in ϵ are due to the changing magnetic connectivity to the bowshock during the turbulent intervals.

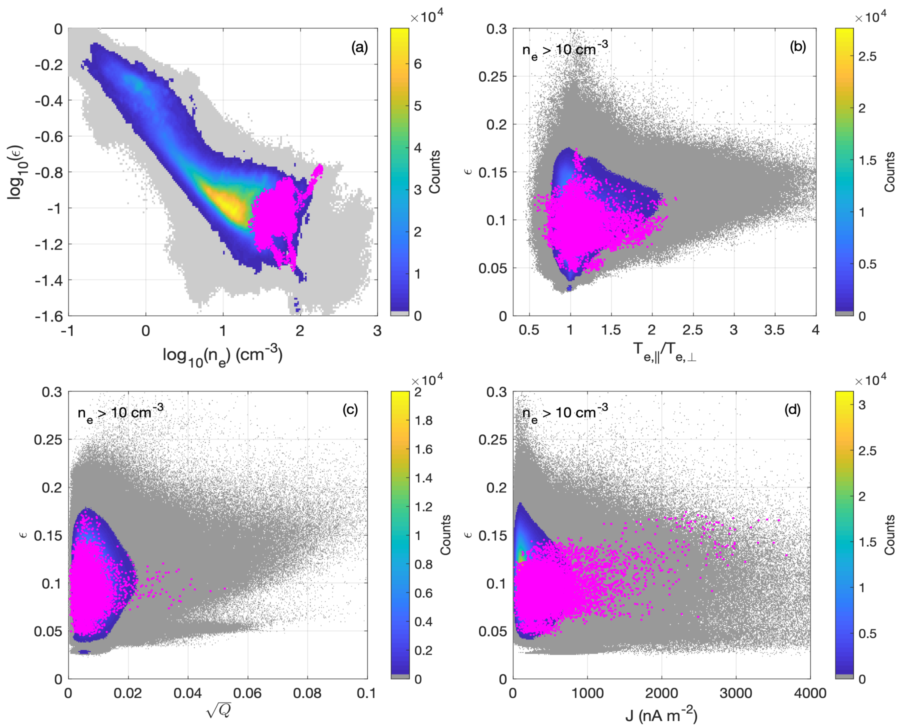

Figure 12. Two-dimensional histograms of ϵ versus different plasma conditions when $n_e > 10\ \mathrm{cm}^{-3}$ [panels (b)–(d)]. Overplotted in magenta are scatter plots of the points in the interval shown in Figure 9 for MMS1–MMS4. (a) $\log_{10}\epsilon$ versus $\log_{10}T_e$. (b) ϵ versus $\log_{10}T_{e,\parallel}/T_{e,\perp}$. (c) ϵ versus agyrotropy measure $\sqrt{Q}$. (d) ϵ versus $|\mathbf{J}|$.

In Figure 13 we present three electron distributions at the times indicated by the magenta dashed lines in Figure 11. Each row consists of the observed electron distribution the model bi-Maxwellian distribution and $(f_e - f_{\mathrm{model}})v^3$, which indicates the regions of velocity space that contribute most to ϵ. The observed distributions have ϵ of 0.046, 0.12, and 0.17, which correspond to percentiles of 1, 72, and 99, respectively. In each case the distributions are close to isotropic, with $T_{\parallel}/T_{\perp} = 1.1$. For the first distribution, Figures 13a and 13b show that f_e is very similar to f_{model}, and as a result $(f_e - f_{\mathrm{model}})v^3$ remains small. For the second there is a beam-like feature in f_e (Figure 13d), which is not captured by f_{model} (Figure 13e) and results in an enhanced ϵ. Figure 13g shows a clear flat-top distribution, which differs significantly from f_{model} (Figure 13h). Figure 13i shows large values of $(f_e - f_{\mathrm{model}})v^3$, with $(f_e - f_{\mathrm{model}})v^3 < 0$ at low speeds, $(f_e - f_{\mathrm{model}})v^3 > 0$ at intermediate speeds, and $(f_e - f_{\mathrm{model}})v^3 < 0$ at higher speeds. This results in a large ϵ. This distribution is similar to the flat-top distributions found at the bowshock, which exhibit large ϵ.

In summary, we find that in magnetosheath turbulence ϵ varies significantly, but is not directly correlated with local plasma conditions, such as density, temperature, temperature anisotropy, and current density. This may suggest that the local plasma turbulence does not significantly enhance ϵ. We propose that the enhanced ϵ seen intermittently in magnetosheath turbulence is likely generated at the bowshock. We suggest that the changes in magnetic connectivity to the bowshock, due to the changes in the direction of $\mathbf{B}$ throughout magnetosheath turbulence affect the local values of ϵ.

6 Conclusions

In this paper we have investigated the deviation of electron distributions from the bi-Maxwellian distribution function. We have defined a dimensionless quantity ϵ, which quantifies the deviation of the observed electron distribution from the bi-Maxwellian distribution function. We have calculated this quantity for the electron distributions observed by the four MMS over a six month interval, primarily focussing on the magnetosphere, magnetopause, and magnetosheath. The key results of this study are:

(1) The electron non-Maxwellianity ϵ scales inversely with the electron number density near the magnetopause. This is primarily due to the tendency of low-density magnetospheric electron distributions having distinct cold and hot populations, which deviate significantly from a single bi-Maxwellian distribution resulting in large ϵ, whereas in the higher-density magnetosheath the electron distributionsa are characterized a single temperature. By comparing specific events with the statistical study of ϵ versus number density we can identify regions of enhanced non-Maxwellianity.

(2) Statistically, the electron non-Maxwellianity does not depend strongly on local plasma properties such as temperature anisotropy, agyrotropy, and current density.

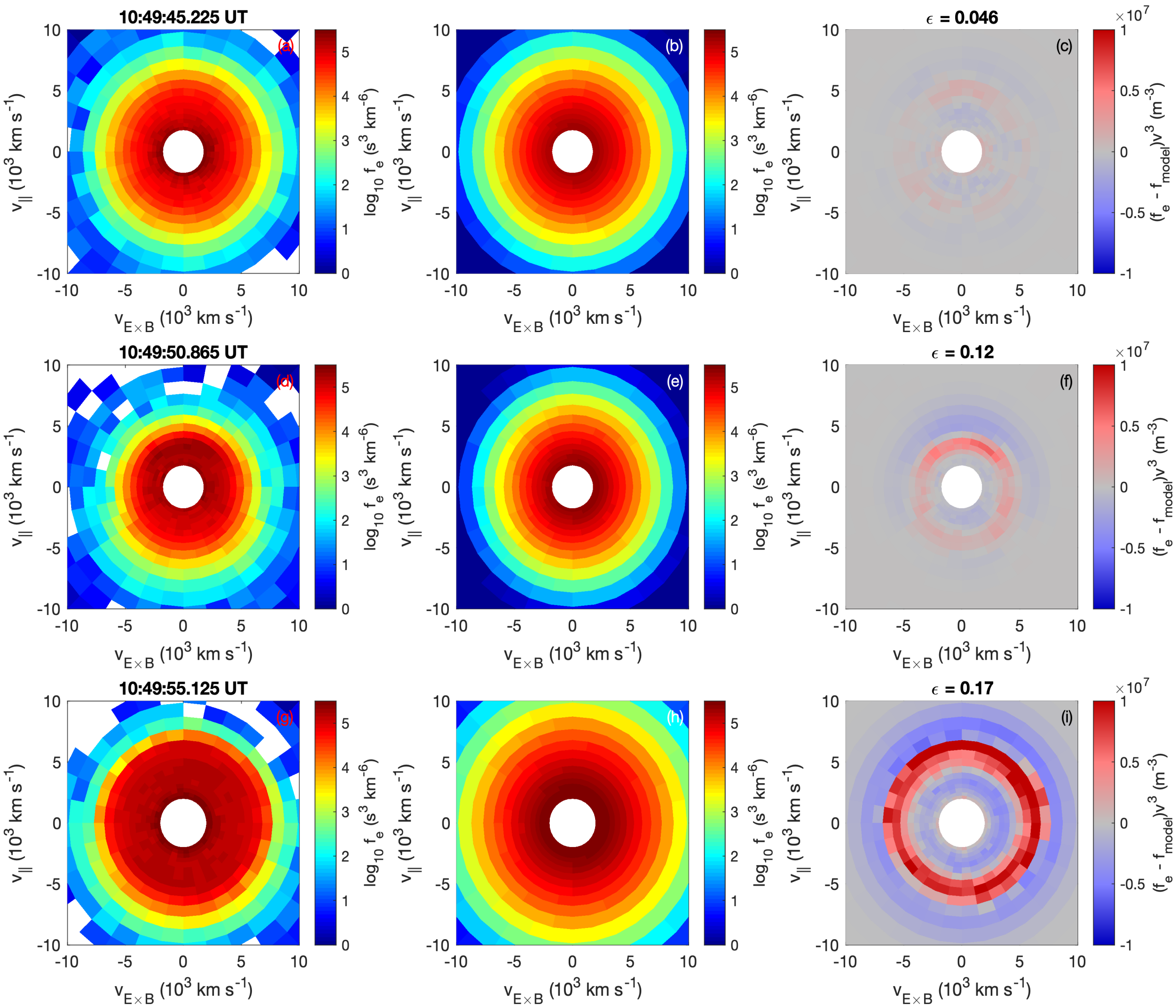

Figure 13. Three examples of electron distributions and the predicted bi-Maxwellian distribution based on the electron moments from the foreshock crossing observed by MMS1 on 25 November 2015 in the turbulent magnetosheath. Panels (a), (d), and (g) show a two-dimensional slice of the observed three-dimensional electron distribution in the **B** and **E** $\times$ **B** plane. Panels (b), (e), and (h) show the modeled bi-Maxwellian distributions in the same plane. Panels (c), (f), and (i) show the modeled bi-Maxwellian distributions in the same plane. Panels (c) and (f) show $(f_e - f_{\text{model}})v^3$ in the same plane, which indicates the regions of velocity space that contribute most to ϵ. The distribution in panels (a)–(c) is corresponds to low ϵ, (d)–(f) correspond to moderate ϵ, and (g)–(i) correspond to high ϵ. The values ofϵ of the three distributions are given in the titles of panels (c), (f), and (i).

(3) The observed temperature anisotropies are bounded by the thresholds for the oblique electron firehose instability and the whistler temperature anisotropy instability in high β plasmas, such as at the magnetopause and in the magnetosheath. The distributions close to these thresholds tend to be close to bi-Maxwellian. These results suggest that these instabilities constrain the electron temperature anisotropies that can develop in high-β plasmas.

(4) Enhanced ϵ are found in the ion and electron diffusion regions of magnetic reconnection. While very large ϵ are observed in the electron diffusion region where electron distributions are agyrotropic, similarly large ϵ can develop in the outflow regions of magnetic reconnection. Thus, ϵ cannot uniquely identify electron diffusion regions.

(5) Enhanced ϵ develops at the bowshock, due to the development of flat-top distributions and electron beams resulting from the cross-shock potential. These ϵ develop over ion spatial scales and tend to decrease behind the bowshock in the magnetosheath.

(6) Intermittent enhancements in ϵ are observed in magnetosheath turbulence. These increases in ϵ are not well correlated with the local plasma conditions, which might suggest that the observed ϵ are produced at the bowshock, and is highly variable in magnesheath turbulence due to the changing magnetic connectivity to the bowshock.

These results show that ϵ can be used to identify regions where large deviations in the observed distributions from a bi-Maxwellian distribution function, which may suggest that local kinetic processes are occurring. Future work on electron non-Maxwellianity should include the following:

(1) More detailed investigations of ϵ in magnetosheth turbulence and how it relates to local turbulent processes and connectivity to the bowshock.

(2) Direct observation of the electron firehose instability and the resulting waves. Our results show that the electron temperature anisotropy is well constrained by the oblique electron firehose instability; however, to our knowledge the electron firehose instability has not been directly observed in spacecraft data.

Acknowledgments

We thank the entire MMS team and instrument PIs for data access and support. This work was supported by the Swedish National Space Board, grant 128/17. MMS data are available at https://lasp.colorado.edu/mms/sdc/public.

A: Non-Maxwellianity of time-averaged electron distributions in the magnetosphere

In this Appendix we investigate the increase in ϵ in the magnetosphere due to the statistical noise in the electron distributions measured by FPI-DES. To do this we average the electron distributions over time to increase the overall counting statistics of the electron distributions and compare the results with the unaveraged distributions. The time averaging ensures that the observed distribution is smoother as a function of speed and angle. For phase 1a of the MMS mission FPI was operating in a mode where two distinct energy tables are used, which alternate for each consecutive electron distribution [*Pollock et al.*, 2016]. This results in the electrons being sampled at 64 energies over two consecutive electron distributions. To create time-averaged electron distributions we first combine each two consecutive electron distributions to construct electron distributions with 64 energy channels and sampled every 60 ms. We then simply average f_e of these distributions at all energies and angles to obtain the time-averaged electron distributions. We now calculate the non-Maxwellianity for the original distributions ϵ, the distributions with 64 energy channels ϵ_{64}, and electron distributions averaged over 3 $\epsilon_{av,3}$, 5 $\epsilon_{av,5}$, and 11 $\epsilon_{av,11}$ of the 64 energy channel distributions. Figures A.1 and A.2 show two examples of these calculations of ϵ.

In Figure A.1 we plot the magnetopause crossing shown in Figure 6. Figures A.1a and A.1b show the electron energy spectrogram and n_e, respectively. The low-density magnetosphere is characterized by a single dominant electron distribution with temperature comparable to the magnetosheath. Figure A.1c shows ϵ, ϵ_{64}, $\epsilon_{av,3}$, $\epsilon_{av,5}$, and $\epsilon_{av,11}$. We find that there is little difference between ϵ and ϵ_{64}, except that the fluctuations in ϵ_{64} are smaller. This is not surprising because ϵ_{64} does not involve time averaging, so the counting statistics are not improved for the 64 energy channel distributions. However, we find that when the distributions are time-averaged there is a decrease in ϵ in the magnetosphere. In the magnetosheath, where n_e is larger, time-averaging has only a very minor effect. In the magnetosphere the most significant decrease occurs between ϵ and $\epsilon_{av,3}$;

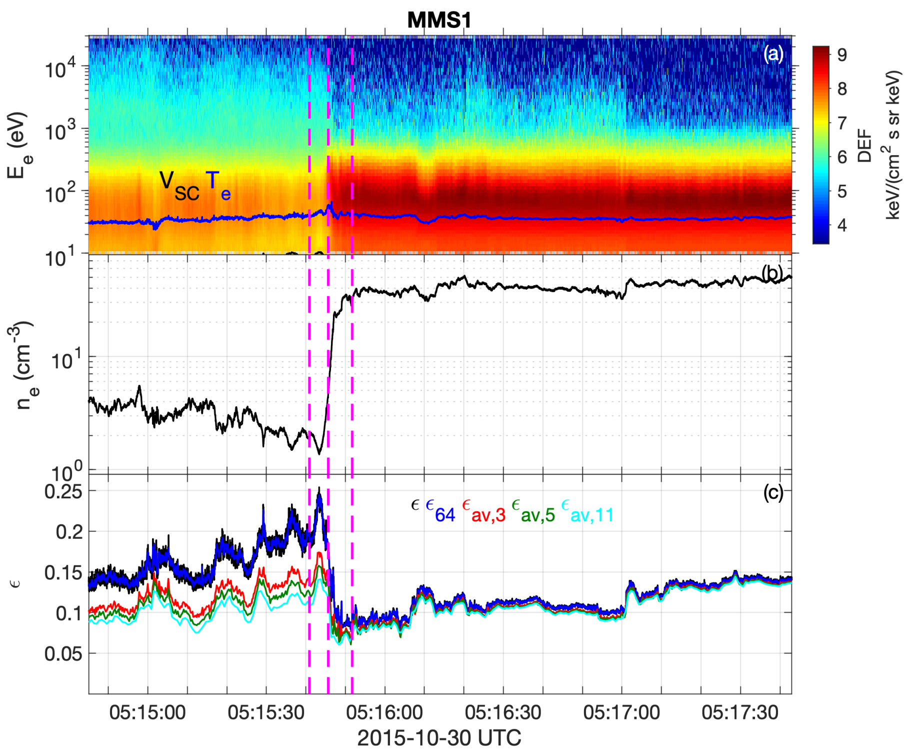

Figure A.1. Calculations of ϵ for different time averages for the magnetopause crossing observed on 2015 October 30 by MMS1. (a) Electron omnidirectional energy spectrogram with T_e (blue) and V_{SC} (black). (b) n_e. (c) Non-Maxwellianities ϵ (black), ϵ_{64}, $\epsilon_{av,3}$ (red), $\epsilon_{av,5}$ (green), $\epsilon_{av,11}$ (cyan). The magenta dashed lines indicate the times of the electron distributions shown in Figure 1.

taking longer time averages does not result in significant further decreases in ϵ. In the magnetosphere ϵ decreases by ~ 30 % when time-averaged distributions are used. This indicates that the counting statistics in the magnetosphere artificially increase ϵ in this case.

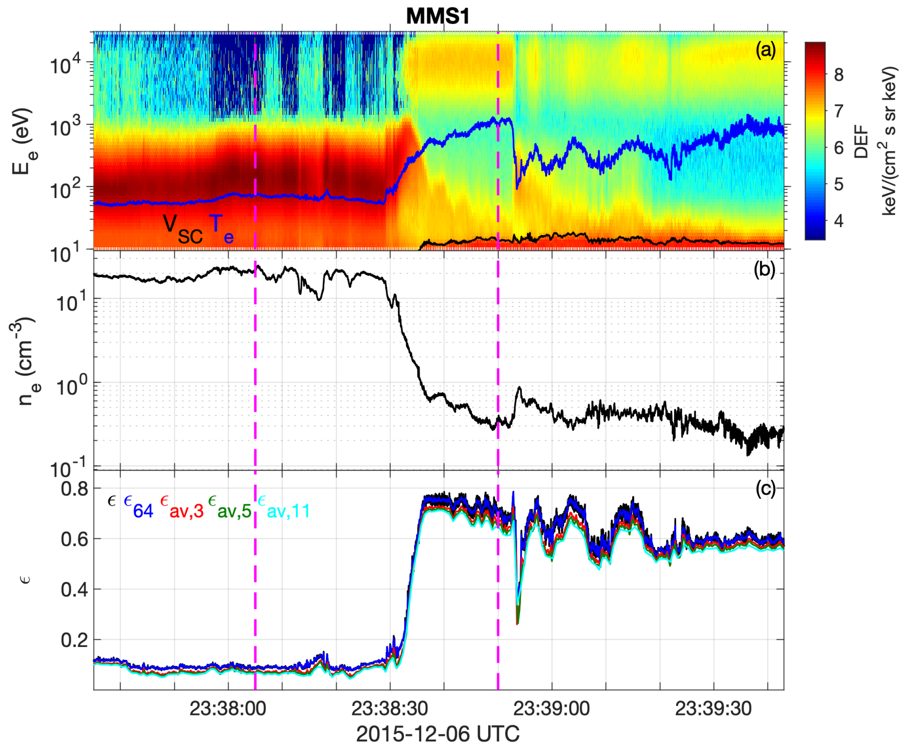

Figure A.2. Calculations of ϵ for different time averages for the magnetopause crossing observed on 2015 December 06 by MMS1. (a) Electron omnidirectional energy spectrogram with T_e (blue) and V_{SC} (black). (b) n_e. (c) Non-Maxwellianities ϵ (black), ϵ_{64}, $\epsilon_{av,3}$ (red), $\epsilon_{av,5}$ (green), $\epsilon_{av,11}$ (cyan). The magenta dashed lines indicate the times of the electron distributions shown in Figure 3.

As a second example, we plot the magnetopause crossing observed on 2015 December 06 in Figure A.2. Two electron distributions from this event are shown in Figure 3. For this event the magnetospheric electron distributions are composed of distinct hot and cold populations (Figure A.1a), in contrast to the event in Figure A.1. In this case time-averaging only results in a very small decrease in ϵ both in the magnetosheath and in the magnetosphere. In the magnetosphere the very large ϵ results from the electrons having distinct temperatures of $\sim$ 10 eV and $\gtrsim$ 1 keV. In this case the effect of counting statistics on ϵ is very small, and the observed ϵ is physical in the magnetosphere. In this case the distinct electron temperatures of magnetospheric electron distributions primarily determines ϵ.

To illustrate the dependence of ϵ on n_h/n_c and T_h/T_c, we consider an electron distribution given by the sum of two stationary Maxwellian distributions with distinct densities n_c and n_h, and distinct temperatures T_c and T_h, where the subscripts c and h refer to the cold and hot distributions. The model Maxwellian distribition used in the calculation of ϵ has $n_e = n_c + n_h$ and temperature given by equation (3). The resulting ϵ is plotted versus n_h/n_c and T_h/T_c in Figure A.3. We find that a large region of parameter space has large values of ϵ. For $n_h/n_c \lesssim 1$ and $T_h/T_c \gtrsim 10$, ϵ can reach very large values. For very large T_h/T_c, ϵ can approach 1.

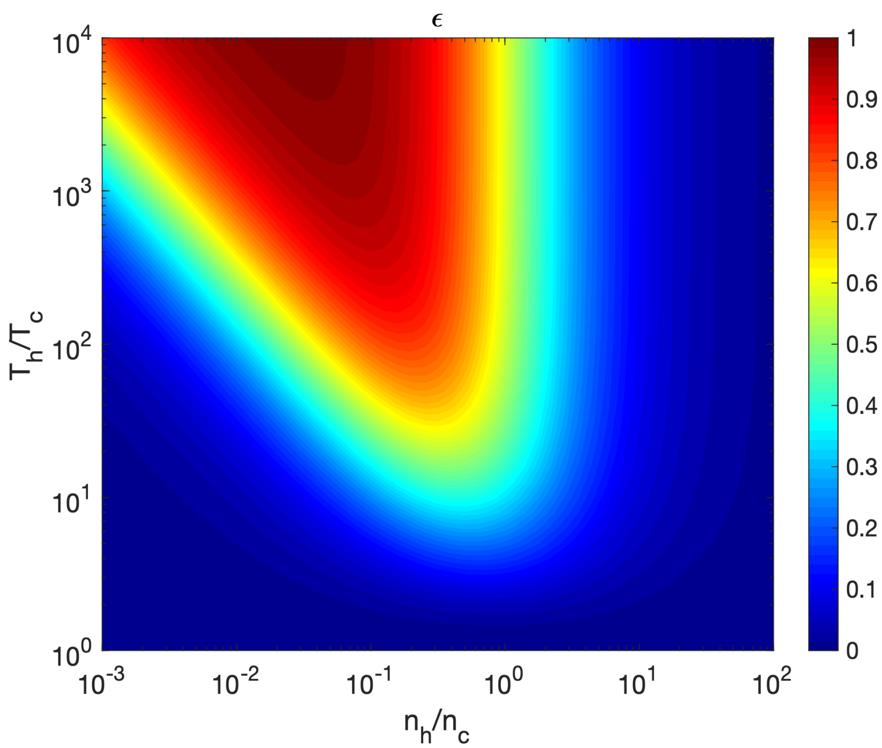

Figure A.3. Non-Maxwellianity ϵ as a function of n_h/n_c and T_h/T_c for electron distributions composed of two Maxwellian distributions with distinct temperatures.

For Earth's outer magnetosphere T_h/T_c is often $\sim 10^2$, with $T_c \sim 10$ eV and $T_c \sim 1$ keV when cold electrons are present and n_c can be comparable to n_h and in some cases $n_c \gg n_h$. As a result, in the outer magnetosphere ϵ will have very large values of ϵ, as seen in Figure A.2. Therefore, we expect that large values of ϵ to be observed in the magnetopause and at the magnetopause when cold electrons are present. This will result in the large values of ϵ in the magnetosphere, $n_e \lesssim 1$ cm^{-3} and can account for the statistical results in Figure 2.

In Figure A.4 we statistically compare ϵ with $\epsilon_{av,5}$ using the entire dataset used in section 4. For direct comparison of ϵ with $\epsilon_{av,5}$ we have downsampled ϵ to the same sampling rate as $\epsilon_{av,5}$ (0.3 s or ten electron distributions). In Figures A.4a and A.4b we plot the histograms of $\log_{10}(\epsilon)$ and $\log_{10}(\epsilon_{av,5})$ versus $\log_{10}(n_e)$, respectivity. Both histograms are qualitatively very similar. In particular, in both plots ϵ and $\epsilon_{av,5}$ statistically decrease significantly for $1\,\mathrm{cm}^{-3} \lesssim n_e \lesssim 10\,\mathrm{cm}^{-3}$. The main difference is that there is a slight decrease in $\epsilon_{av,5}$ compared with ϵ. This can be seen clearly in Figure A.4c, which plots the histogram of ϵ versus $\epsilon_{av,5}$. For almost all points $\epsilon_{av,5} < \epsilon$, as expected from averaging the observed distribution function with time. In Figure A.4d we plot the histogram of $\epsilon_{av,5}/\epsilon$ versus $\log_{10}(n_e)$. For almost all points we find that $0.5 < \epsilon_{av,5}/\epsilon < 1$, meaning that at most averaging five 64 energy channel electron distributions reduces the non-Maxwellianity by a factor of 2. The black line in Figure A.4d shows the median of $\epsilon_{av,5}/\epsilon$ as a function of n_e. For $n_e \lesssim 20$ cm^{-3} we find that the median remains large, > 0.9, indicating that averaging the electron distribution in time does not significantly change the results. For $n_e \gtrsim 20$ cm^{-3} we find that the median of $\epsilon_{av,5}/\epsilon$ decreases to 0.7. At $n_e \sim 1$ cm^{-3} there is a smaller peak in the median at 0.8. This n_e corresponds to the typical density in the outer magnetosphere, where hot and cold electron distributions are common. Because the decrease in $\epsilon_{av,5}$ from ϵ is typically relatively small, we conclude that the increase in ϵ as n_e decreases is physical and primarily due to the simultaneous presence of electron distributions with distinct temperatures in the outer magnetosphere.

In this Appendix we consider the effect of instrumental counting statistics on the calculated ϵ. The key results are:

(1) Improving the counting statistics by averaging the electron distributions over time before calculating ϵ results in ϵ decreasing. This decrease tends to be larger at lower densities. Nevertheless, ϵ increases significantly as density decreases and remains large in the outer magnetosphere and qualitatively the results do not change significantly.

(2) The large values of ϵ in the outer magnetosphere are due to the presence of cold electrons. The simultaneous presence of cold and hot electron distributions with distinct temperatures is the primary source of non-Maxwellianity in the outer magnetosphere.

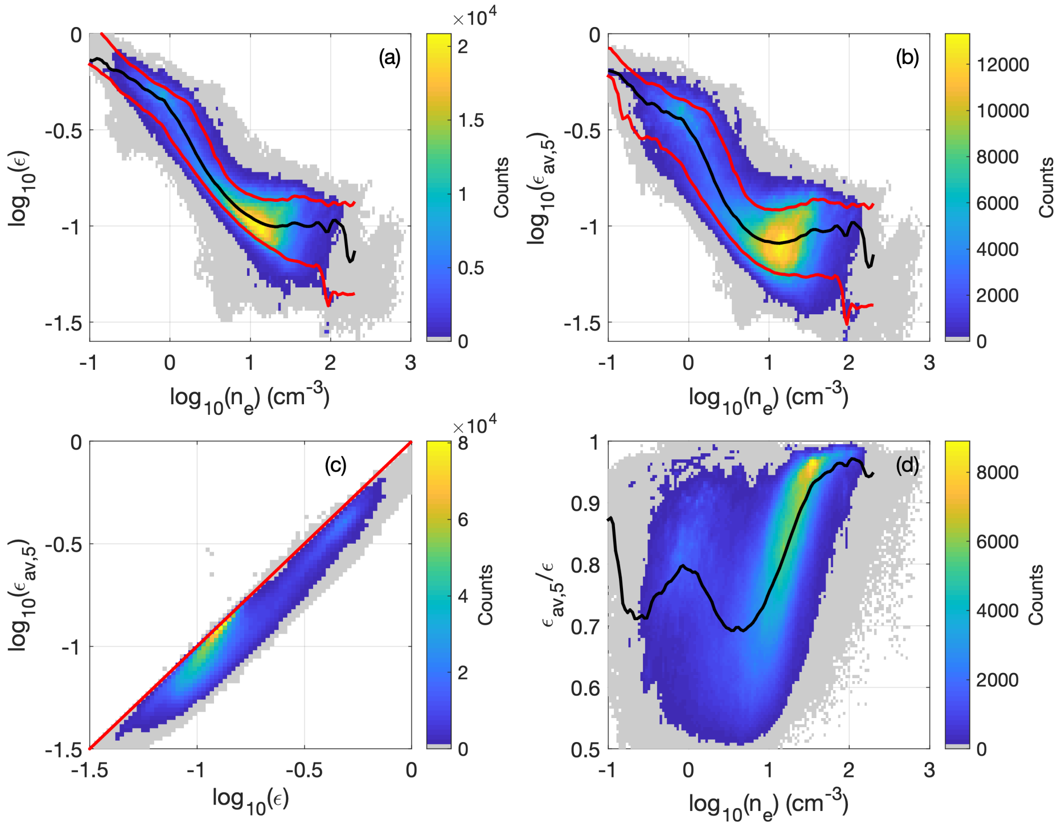

Figure A.4. Statstical comparison of ϵ with $\epsilon_{av,5}$. (a) Histogram of $\log_{10}(n_e)$ versus $\log_{10}(\epsilon)$. (b) Histogram of $\log_{10}(n_e)$ versus $\log_{10}(\epsilon_{av,5})$. The black lines in panels (a) and (b) indicate the medians (50th percentiles) of ϵ and $\epsilon_{av,5}$ as a function n_e and the lower and upper red curves indicate the 10th and 90th percentiles as a function of n_e, respectively. (c) Histogram of $\log_{10}\epsilon$ versus $\log_{10}(\epsilon_{av,5})$. The red line indicates $\epsilon = \epsilon_{av,5}$. (d) Histogram of $\epsilon_{av,5}/\epsilon$ versus n_e. The black line is the median of $\epsilon_{av,5}/\epsilon$ as a function of n_e. For direct comparison of ϵ with $\epsilon_{av,5}$ we have downsampled ϵ to the same sampling rate of $\epsilon_{av,5}$.

References

Barrie, A. C., F. Cipriani, C. P. Escoubet, S. Toledo-Redondo, R. Nakamura, K. Torkar, Z. Sternovsky, S. Elkington, D. Gershman, B. Giles, and C. Schiff (2019), Characterizing spacecraft potential effects on measured particle trajectories, *Physics of Plasmas*, *26*(10), 103,504, doi:10.1063/1.5119344.

Burch, J. L., T. E. Moore, R. B. Torbert, and B. L. Giles (2016), Magnetospheric Multiscale Overview and Science Objectives, *Space Sci. Rev.*, *199*, 5–21, doi:10.1007/s11214-015-0164-9.

Burch, J. L., R. B. Torbert, T. D. Phan, L.-J. Chen, T. E. Moore, R. E. Ergun, J. P. Eastwood, D. J. Gershman, P. A. Cassak, M. R. Argall, S. Wang, M. Hesse, C. J. Pollock, B. L. Giles, R. Nakamura, B. H. Mauk, S. A. Fuselier, C. T. Russell, R. J. Strangeway, J. F. Drake, M. A. Shay, Y. V. Khotyaintsev, P.-A. Lindqvist, G. Marklund, F. D. Wilder, D. T. Young, K. Torkar, J. Goldstein, J. C. Dorelli, L. A. Avanov, M. Oka, D. N. Baker, A. N. Jaynes, K. A. Goodrich, I. J. Cohen, D. L. Turner, J. F. Fennell, J. B. Blake, J. Clemmons, M. Goldman, D. Newman, S. M. Petrinec, K. J. Trattner, B. Lavraud, P. H. Reiff, W. Baumjohann, W. Magnes, M. Steller, W. Lewis, Y. Saito, V. Coffey, and M. Chandler (2016), Electron-scale measurements of magnetic reconnection in space, *Science*, *352*(6290), doi:10.1126/science.aaf2939.

Chasapis, A., W. H. Matthaeus, T. N. Parashar, M. Wan, C. C. Haggerty, C. J. Pollock, B. L. Giles, W. R. Paterson, J. Dorelli, D. J. Gershman, R. B. Torbert, C. T. Russell, P. A. Lindqvist, Y. Khotyaintsev, T. E. Moore, R. E. Ergun, and J. L. Burch (2018), In Situ Observation of Intermittent Dissipation at Kinetic Scales in the Earth's Magnetosheath, *Astrophysical Journal Letters*, *856*(1), L19, doi:10.3847/2041-8213/aaadf8.

Ergun, R. E., S. Tucker, J. Westfall, K. A. Goodrich, D. M. Malaspina, D. Summers, J. Wallace, M. Karlsson, J. Mack, N. Brennan, B. Pyke, P. Withnell, R. Torbert, J. Macri, D. Rau, I. Dors, J. Needell, P.-A. Lindqvist, G. Olsson, and C. M. Cully (2016), The Axial Double Probe and Fields Signal Processing for the MMS Mission, *Space Sci. Rev.*, *199*, 167–188, doi:10.1007/s11214-014-0115-x.

Feldman, W. C., S. J. Bame, S. P. Gary, J. T. Gosling, D. McComas, M. F. Thomsen, G. Paschmann, N. Sckopke, M. M. Hoppe, and C. T. Russell (1982), Electron heating within the Earth's bow shock, *Phys. Rev. Lett.*, *49*, 199–201, doi:10.1103/PhysRevLett.49.199.

Fuselier, S. A., S. K. Vines, J. L. Burch, S. M. Petrinec, K. J. Trattner, P. A. Cassak, L.-J. Chen, R. E. Ergun, S. Eriksson, B. L. Giles, D. B. Graham, Y. V. Khotyaintsev, B. Lavraud, W. S. Lewis, J. Mukherjee, C. Norgren, T.-D. Phan, C. T. Russell, R. J. Strangeway, R. B. Torbert, and J. M. Webster (2017), Large-scale characteristics of reconnection diffusion regions and associated magnetopause crossings observed by MMS, *Journal of Geophysical Research (Space Physics)*, *122*, 5466–5486, doi: 10.1002/2017JA024024.

Gary, S. P., and K. Nishimura (2003), Resonant electron firehose instability: Particle-in-cell simulations, *Physics of Plasmas*, *10*(9), 3571–3576, doi:10.1063/1.1590982.

Gary, S. P., and J. Wang (1996), Whistler instability: Electron anisotropy upper bound, *J. Geophys. Res.*, *101*(A5), 10,749–10,754, doi:10.1029/96JA00323.

Gary, S. P., K. Liu, R. E. Denton, and S. Wu (2012), Whistler anisotropy instability with a cold electron component: Linear theory, *J. Geophys. Res.*, *117*, A07,203, doi: 10.1029/2012JA017631.

Gershman, D. J., L. A. Avanov, S. A. Boardsen, J. C. Dorelli, U. Gliese, A. C. Barrie, C. Schiff, W. R. Paterson, R. B. Torbert, B. L. Giles, and C. J. Pollock (2017), Spacecraft and Instrument Photoelectrons Measured by the Dual Electron Spectrometers on MMS, *Journal of Geophysical Research (Space Physics)*, *122*(A11), 11, doi: 10.1002/2017JA024518.

Graham, D. B., Y. V. Khotyaintsev, C. Norgren, A. Vaivads, M. André, P.-A. Lindqvist, G. T. Marklund, R. E. Ergun, W. R. Paterson, D. J. Gershman, B. L. Giles, C. J. Pollock, J. C. Dorelli, L. A. Avanov, B. Lavraud, Y. Saito, W. Magnes, C. T. Russell, R. J. Strangeway, R. B. Torbert, and J. L. Burch (2016a), Electron currents and heating in the ion diffusion region of asymmetric reconnection, *Geophys. Res. Lett.*, *43*, 4691–4700, doi:10.1002/2016GL068613.

Graham, D. B., A. Vaivads, Y. V. Khotyaintsev, and M. André (2016b), Whistler emission in the separatrix regions of asymmetric reconnection, *J. Geophys. Res.*, *121*, 1934–1954, doi:10.1002/2015JA021239.

Graham, D. B., Y. V. Khotyaintsev, A. Vaivads, C. Norgren, M. André, J. M. Webster, J. L. Burch, P.-A. Lindqvist, R. E. Ergun, R. B. Torbert, W. R. Paterson, D. J. Gershman, B. L. Giles, W. Magnes, and C. T. Russell (2017), Instability of agyrotropic electron beams near the electron diffusion region, *Phys. Rev. Lett.*, *119*, 025,101, doi: 10.1103/PhysRevLett.119.025101.

Graham, D. B., A. Vaivads, Y. V. Khotyaintsev, A. I. Eriksson, M. Andre, D. M. Malaspina, P.-A. Lindqvist, D. J. Gershman, and F. Plaschke (2018), Enhanced escape of spacecraft photoelectrons caused by Langmuir and upper hybrid waves, *Journal of Geophysical Research: Space Physics*, *123*(9), 7534–7553, doi:10.1029/2018JA025874.

Greco, A., F. Valentini, S. Servidio, and W. H. Matthaeus (2012), Inhomogeneous kinetic effects related to intermittent magnetic discontinuities, *Phys. Rev. E*, *86*(6), 066,405, doi: 10.1103/PhysRevE.86.066405.

Kennel, C. F., and H. E. Petschek (1966), Limit on stably trapped particle fluxes, *J. Geophys. Res.*, *71*, 1–28, doi:10.1029/JZ071i001p00001.

Khotyaintsev, Y. V., D. B. Graham, C. Norgren, E. Eriksson, W. Li, A. Johlander, A. Vaivads, M. André, P. L. Pritchett, A. Retino, T. D. Phan, R. E. Ergun, K. Goodrich, P.-A. Lindqvist, G. T. Marklund, O. L. Contel, F. Plaschke, W. Magnes, R. J. Strangeway, C. T. Russell, H. Vaith, M. R. Argall, C. A. Kletzing, R. Nakamura, R. B. Torbert, W. R. Paterson, D. J. Gershman, J. C. Dorelli, L. A. Avanov, B. Lavraud, Y. Saito, B. L. Giles, C. J. Pollock, D. L. Turner, J. D. Blake, J. F. Fennell, A. Jaynes, B. H. Mauk, and J. L. Burch (2016), Electron jet of asymmetric reconnection, *Geophys. Res. Lett.*, *43*, 5571–5580, doi:10.1002/2016GL069064.

Khotyaintsev, Y. V., D. B. Graham, C. Norgren, and A. Vaivads (2019), Collisionless magnetic reconnection and waves: Progress review, *Frontiers in Astronomy and Space Sciences*, *6*, 70, doi:10.3389/fspas.2019.00070.

Li, X., and S. R. Habbal (2000), Electron kinetic firehose instability, *Journal of Geophysical Research: Space Physics*, *105*(A12), 27,377–27,385, doi:10.1029/2000JA000063.

Liang, H., M. H. Barbhuiya, P. A. Cassak, O. Pezzi, S. Servidio, F. Valentini, and G. P. Zank (2020), Kinetic entropy-based measures of distribution function non-maxwellianity: theory and simulations, *Journal of Plasma Physics*, *86*(5), 825860,502, doi:10.1017/S0022377820001270.

Lindqvist, P.-A., G. Olsson, R. B. Torbert, B. King, M. Granoff, D. Rau, G. Needell, S. Turco, I. Dors, P. Beckman, J. Macri, C. Frost, J. Salwen, A. Eriksson, L. Åhlén, Y. V. Khotyaintsev, J. Porter, K. Lappalainen, R. E. Ergun, W. Wermeer, and S. Tucker (2016), The Spin-Plane Double Probe Electric Field Instrument for MMS, *Space Sci. Rev.*, *199*, 137–165, doi:10.1007/s11214-014-0116-9.

Norgren, C., D. B. Graham, Y. V. Khotyaintsev, M. André, A. Vaivads, L.-J. Chen, P.-A. Lindqvist, G. T. Marklund, R. E. Ergun, W. Magnes, R. J. Strangeway, C. T. Russell,

R. B. Torbert, W. R. Paterson, D. J. Gershman, J. C. Dorelli, L. A. Avanov, B. Lavraud, Y. Saito, B. L. Giles, C. J. Pollock, and J. L. Burch (2016), Finite gyroradius effects in the electron outflow of asymmetric magnetic reconnection, *Geophys. Res. Lett.*, *43*, 6724–6733, doi:10.1002/2016GL069205.

Oka, M., L. B. Wilson III, T. D. Phan, A. J. Hull, T. Amano, M. Hoshino, M. R. Argall, O. L. Contel, O. Agapitov, D. J. Gershman, Y. V. Khotyaintsev, J. L. Burch, R. B. Torbert, C. Pollock, J. C. Dorelli, B. L. Giles, T. E. Moore, Y. Saito, L. A. Avanov, W. Paterson, R. E. Ergun, R. J. Strangeway, C. T. Russell, and P. A. Lindqvist (2017), Electron scattering by high-frequency whistler waves at Earth's bow shock, *The Astrophysical Journal*, *842*(2), L11, doi:10.3847/2041-8213/aa7759.

Perri, S., D. Perrone, E. Yordanova, L. Sorriso-Valvo, W. R. Paterson, D. J. Gershman, B. L. Giles, C. J. Pollock, J. C. Dorelli, L. A. Avanov, and et al. (2020), On the deviation from maxwellian of the ion velocity distribution functions in the turbulent magnetosheath, *Journal of Plasma Physics*, *86*(1), 905860,108, doi: 10.1017/S0022377820000021.

Phan, T. D., J. P. Eastwood, P. A. Cassak, M. ÃŸieroset, J. T. Gosling, D. J. Gershman, F. S. Mozer, M. A. Shay, M. Fujimoto, W. Daughton, J. F. Drake, J. L. Burch, R. B. Torbert, R. E. Ergun, L. J. Chen, S. Wang, C. Pollock, J. C. Dorelli, B. Lavraud, B. L. Giles, T. E. Moore, Y. Saito, L. A. Avanov, W. Paterson, R. J. Strangeway, C. T. Russell, Y. Khotyaintsev, P. A. Lindqvist, M. Oka, and F. D. Wilder (2016), MMS observations of electron-scale filamentary currents in the reconnection exhaust and near the X line, *Geophysical Research Letters*, *43*(12), 6060–6069, doi:10.1002/2016GL069212.

Pollock, C., T. Moore, A. Jacques, J. Burch, U. Gliese, Y. Saito, T. Omoto, L. Avanov, A. Barrie, V. Coffey, J. Dorelli, D. Gershman, B. Giles, T. Rosnack, C. Salo, S. Yokota, M. Adrian, C. Aoustin, C. Auletti, S. Aung, V. Bigio, N. Cao, M. Chandler, D. Chornay, K. Christian, G. Clark, G. Collinson, T. Corris, A. De Los Santos, R. Devlin, T. Diaz, T. Dickerson, C. Dickson, A. Diekmann, F. Diggs, C. Duncan, A. Figueroa-Vinas, C. Firman, M. Freeman, N. Galassi, K. Garcia, G. Goodhart, D. Guererro, J. Hageman, J. Hanley, E. Hemminger, M. Holland, M. Hutchins, T. James, W. Jones, S. Kreisler, J. Kujawski, V. Lavu, J. Lobell, E. LeCompte, A. Lukemire, E. MacDonald, A. Mariano, T. Mukai, K. Narayanan, Q. Nguyan, M. Onizuka, W. Paterson, S. Persyn, B. Piepgrass, F. Cheney, A. Rager, T. Raghuram, A. Ramil, L. Reichenthal, H. Rodriguez, J. Rouzaud, A. Rucker, Y. Saito, M. Samara, J.-A. Sauvaud,

D. Schuster, M. Shappirio, K. Shelton, D. Sher, D. Smith, K. Smith, S. Smith, D. Steinfeld, R. Szymkiewicz, K. Tanimoto, J. Taylor, C. Tucker, K. Tull, A. Uhl, J. Vloet, P. Walpole, S. Weidner, D. White, G. Winkert, P.-S. Yeh, and M. Zeuch (2016), Fast Plasma Investigation for Magnetospheric Multiscale, *Space Sci. Rev.*, *199*, 331–406, doi: 10.1007/s11214-016-0245-4.

Russell, C. T., B. J. Anderson, W. Baumjohann, K. R. Bromund, D. Dearborn, D. Fischer, G. Le, H. K. Leinweber, D. Leneman, W. Magnes, J. D. Means, M. B. Moldwin, R. Nakamura, D. Pierce, F. Plaschke, K. M. Rowe, J. A. Slavin, R. J. Strangeway, R. Torbert, C. Hagen, I. Jernej, A. Valavanoglou, and I. Richter (2016), The magnetospheric multiscale magnetometers, *Space Sci. Rev.*, *199*, 189–256, doi:10.1007/s11214-014-0057-3.

Scudder, J. D. (1995), A review of the physics of electron heating at collisionless shocks, *Advances in Space Research*, *15*, 181–223, doi:10.1016/0273-1177(94)00101-6.

Servidio, S., A. Chasapis, W. H. Matthaeus, D. Perrone, F. Valentini, T. N. Parashar, P. Veltri, D. Gershman, C. T. Russell, B. Giles, S. A. Fuselier, T. D. Phan, and J. Burch (2017), Magnetospheric multiscale observation of plasma velocity-space cascade: Hermite representation and theory, *Phys. Rev. Lett.*, *119*, 205,101, doi: 10.1103/PhysRevLett.119.205101.

Swisdak, M. (2016), Quantifying gyrotropy in magnetic reconnection, *Geophys. Res. Lett.*, *43*, 43–49, doi:10.1002/2015GL066980.

Toledo-Redondo, S., M. André, Y. V. Khotyaintsev, A. Vaivads, A. Walsh, W. Li, D. B. Graham, B. Lavraud, A. Masson, N. Aunai, A. Divin, J. Dargent, S. Fuselier, D. J. Gershman, J. Dorelli, B. Giles, L. Avanov, C. Pollock, Y. Saito, T. E. Moore, V. Coffey, M. O. Chandler, P.-A. Lindqvist, R. Torbert, and C. T. Russell (2016), Cold ion demagnetization near the X-line of magnetic reconnection, *Geophysical Research Letters*, *43*(13), 6759–6767.

Toledo-Redondo, S., B. Lavraud, S. A. Fuselier, M. AndrÃľ, Y. V. Khotyaintsev, R. Nakamura, C. P. Escoubet, W. Y. Li, K. Torkar, F. Cipriani, A. C. Barrie, B. Giles, T. E. Moore, D. Gershman, P.-A. Lindqvist, R. E. Ergun, C. T. Russell, and J. L. Burch (2019), Electrostatic spacecraft potential structure and wake formation effects for characterization of cold ion beams in the Earth's magnetosphere, *Journal of Geophysical Research: Space Physics*, *124*(12), 10,048–10,062, doi:10.1029/2019JA027145.

Torkar, K., R. Nakamura, M. Tajmar, C. Scharlemann, H. Jeszenszky, G. Laky, G. Fremuth, C. P. Escoubet, and K. Svenes (2016), Active spacecraft potential control investigation, *Space Science Reviews*, *199*, 515–544, doi:10.1007/s11214-014-0049-3.

Valentini, F., D. Perrone, S. Stabile, O. Pezzi, S. Servidio, R. De Marco, F. Marcucci, R. Bruno, B. Lavraud, J. De Keyser, G. Consolini, D. Brienza, L. Sorriso-Valvo, A. Retinò, A. Vaivads, M. Salatti, and P. Veltri (2016), Differential kinetic dynamics and heating of ions in the turbulent solar wind, *New Journal of Physics*, *18*, 125,001, doi:10.1088/1367-2630/18/12/125001.

Voros, Z., E. Yordanova, A. Varsani, K. J. Genestreti, Y. V. Khotyaintsev, W. Li, D. B. Graham, C. Norgren, R. Nakamura, Y. Narita, F. Plaschke, W. Magnes, W. Baumjohann, D. Fischer, A. Vaivads, E. Eriksson, P.-A. Lindqvist, G. Marklund, R. E. Ergun, M. Leitner, M. P. Leubner, R. J. Strangeway, O. Le Contel, C. Pollock, B. J. Giles, R. B. Torbert, J. L. Burch, L. A. Avanov, J. C. Dorelli, D. J. Gershman, W. R. Paterson, B. Lavraud, and Y. Saito (2017), MMS observation of magnetic reconnection in the turbulent magnetosheath, *Journal of Geophysical Research: Space Physics*, *122*, 11,442–11,467, doi:10.1002/2017JA024535.

Walsh, B. M., A. J. Hull, O. Agapitov, F. S. Mozer, and H. Li (2020), A census of magnetospheric electrons from several eV to 30 keV, *Journal of Geophysical Research: Space Physics*, *125*(5), e2019JA027,577, doi:10.1029/2019JA027577.

Webster, J. M., J. L. Burch, P. H. Reiff, A. G. Daou, K. J. Genestreti, D. B. Graham, R. B. Torbert, R. E. Ergun, S. Y. Sazykin, A. Marshall, R. C. Allen, L.-J. Chen, S. Wang, T. D. Phan, B. L. Giles, T. E. Moore, S. A. Fuselier, G. Cozzani, C. T. Russell, S. Eriksson, A. C. Rager, J. M. Broll, K. Goodrich, and F. Wilder (2018), Magnetospheric Multiscale Dayside Reconnection Electron Diffusion Region Events, *Journal of Geophysical Research (Space Physics)*, *123*, 4858–4878, doi:10.1029/2018JA025245.

Yordanova, E., Z. Voros, A. Varsani, D. B. Graham, C. Norgren, Y. V. Khotyaintsev, A. Vaivads, E. Eriksson, R. Nakamura, P.-A. Lindqvist, G. Marklund, R. E. Ergun, W. Magnes, W. Baumjohann, D. Fischer, F. Plaschke, Y. Narita, C. T. Russell, R. J. Strangeway, O. Le Contel, C. Pollock, R. B. Torbert, B. J. Giles, J. L. Burch, L. A. Avanov, J. C. Dorelli, D. J. Gershman, W. R. Paterson, B. Lavraud, and Y. Saito (2016), Electron scale structures and magnetic reconnection signatures in the turbulent magnetosheath, *Geophys. Res. Lett.*, *43*(12), 5969–5978, doi:10.1002/2016GL069191.

Figure 1.

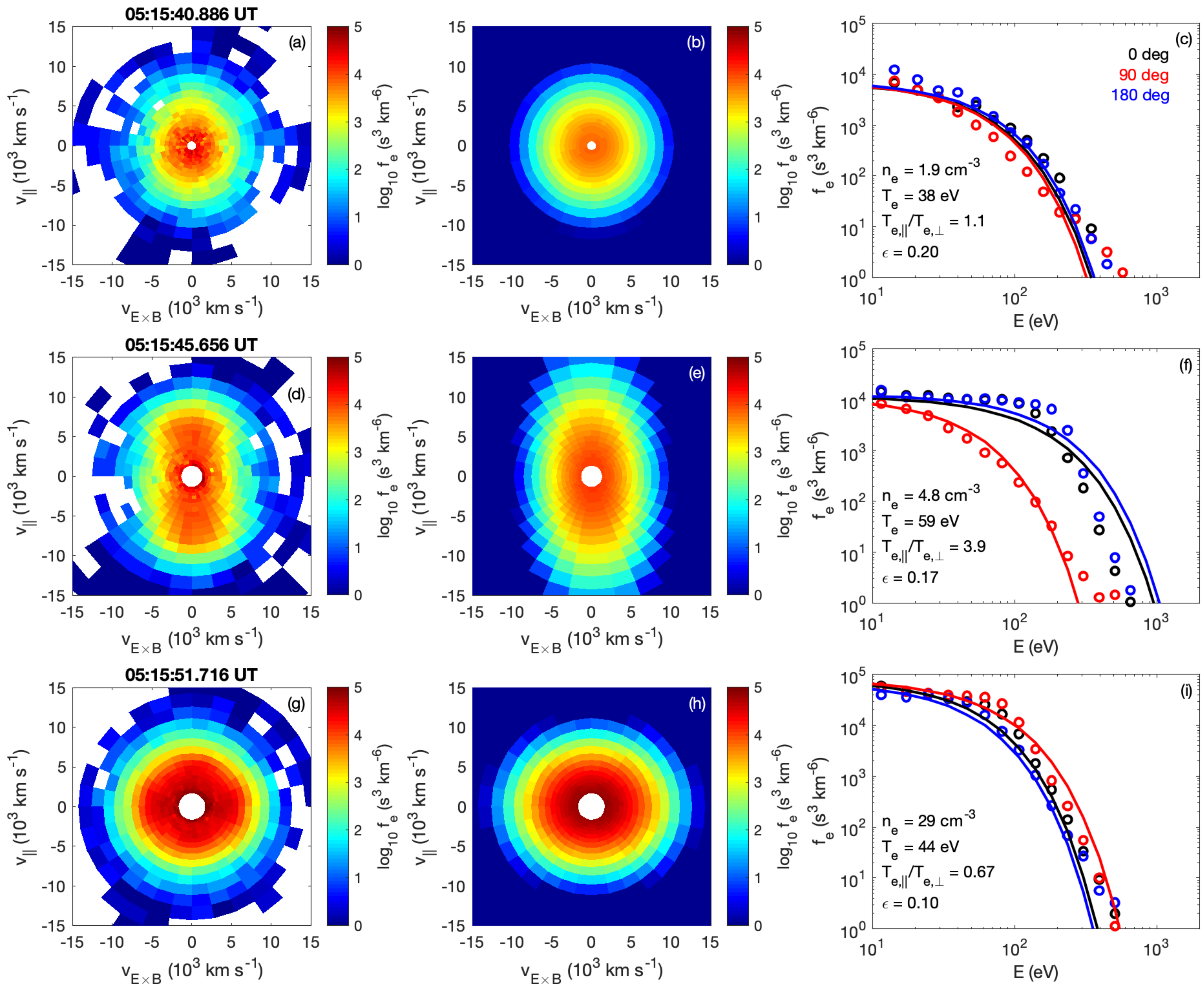

05:15:40.886 UT
05:15:45.656 UT
05:15:51.716 UT
(a)
(b)
(c)
(d)
(e)
(f)
(g)
(h)
(i)
$v_{||}$ (10^3 km s^{-1})
$v_{E\times B}$ (10^3 km s^{-1})
$\log_{10} f_e$ (s^3 km^{-6})
f_e (s^3 km^{-6})
E (eV)
0 deg
90 deg
180 deg
n_e = 1.9 cm^{-3}
T_e = 38 eV
$T_{e,||}/T_{e,\perp}$ = 1.1
ϵ = 0.20
n_e = 4.8 cm^{-3}
T_e = 59 eV
$T_{e,||}/T_{e,\perp}$ = 3.9
ϵ = 0.17
n_e = 29 cm^{-3}
T_e = 44 eV
$T_{e,||}/T_{e,\perp}$ = 0.67
ϵ = 0.10

Figure 2.

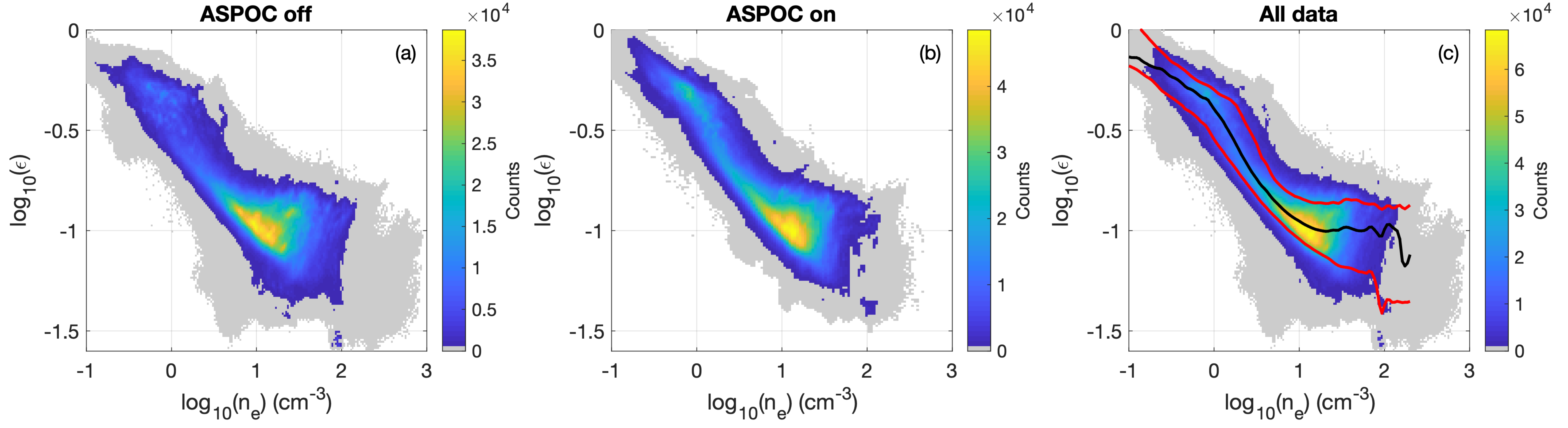
ASPOC off
ASPOC on
All data
(a)
(b)
(c)
$\times 10^4$
Counts
$\log_{10}(\epsilon)$
$\log_{10}(n_e)$ (cm^{-3})
0
-0.5
-1
-1.5
-1
1
2
3
0.5
1.5
2.5
3.5
4
5
6

Figure 3.

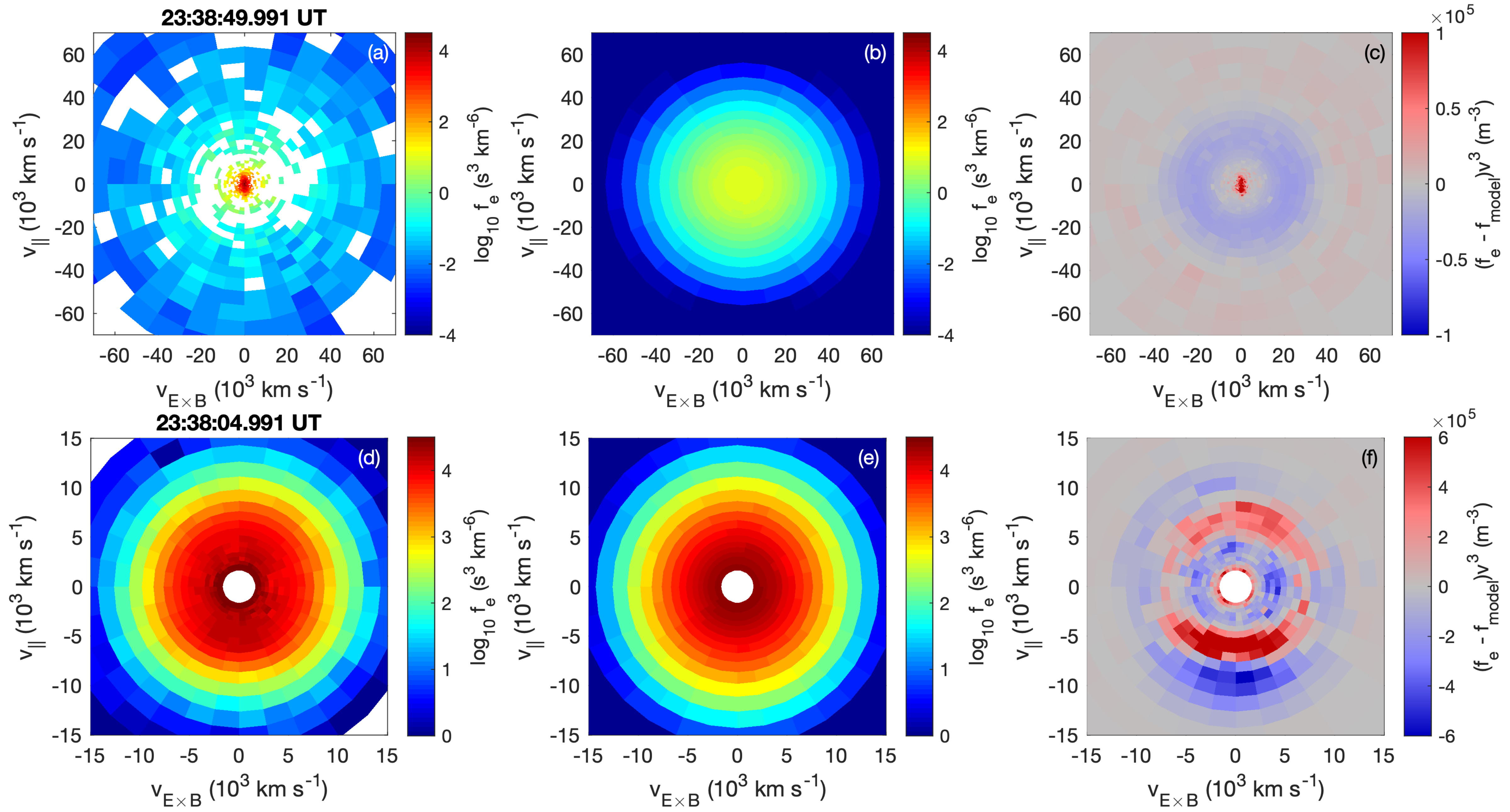

23:38:49.991 UT
(a)
(b)
(c)
23:38:04.991 UT
(d)
(e)
(f)
$v_{||}$ (10^3 km s^{-1})
$v_{E\times B}$ (10^3 km s^{-1})
$\log_{10} f_e$ (s^3 km^{-6})
$(f_e - f_{model})v^3$ (m^{-3})
$\times 10^5$

Figure 4.

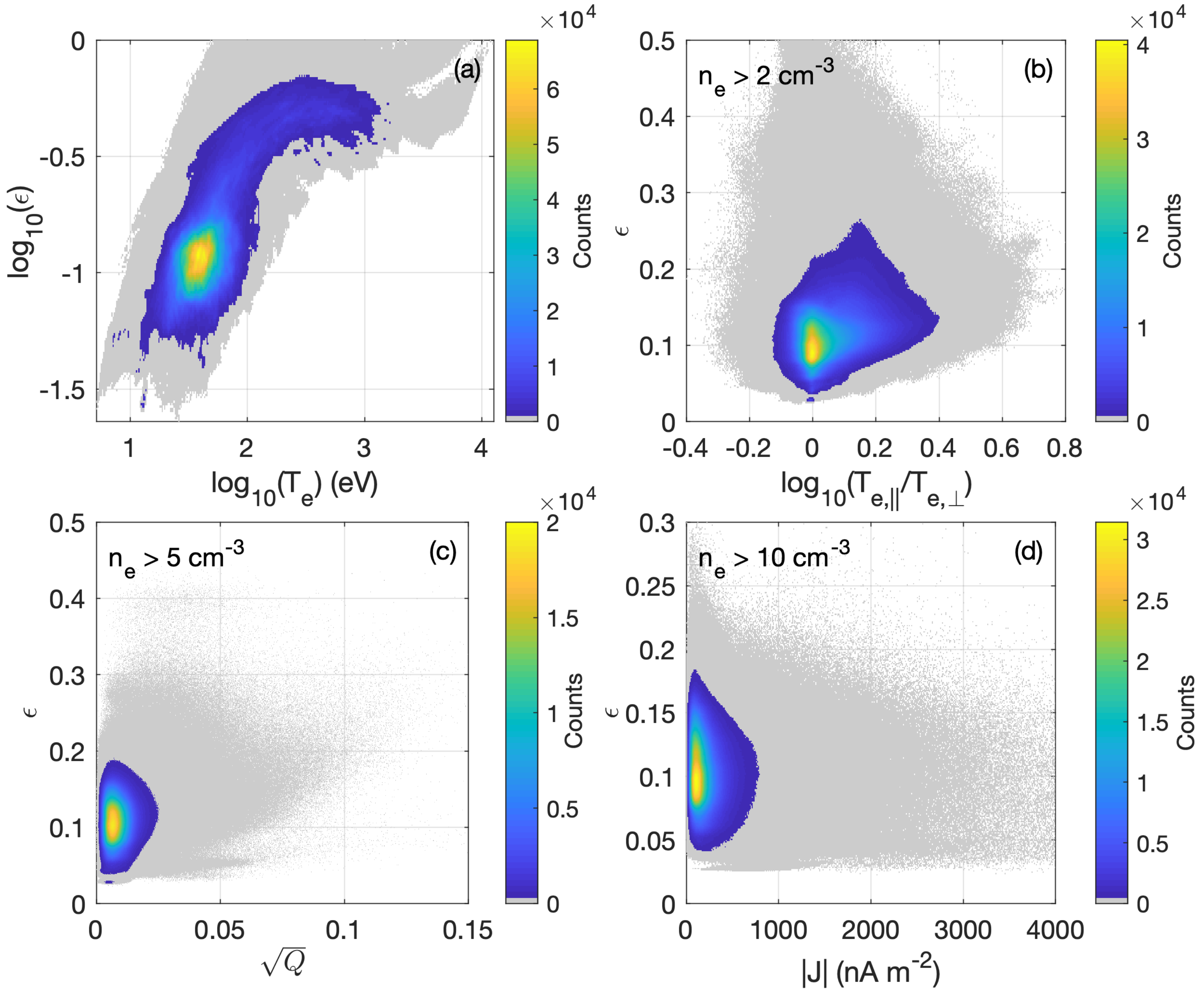
(a)
$\log_{10}(\epsilon)$
$\log_{10}(T_e)$ (eV)
Counts
$\times 10^4$
(b)
$n_e > 2$ cm^{-3}
ϵ
$\log_{10}(T_{e,||}/T_{e,\perp})$
Counts
$\times 10^4$
(c)
$n_e > 5$ cm^{-3}
ϵ
$\sqrt{Q}$
Counts
$\times 10^4$
(d)
$n_e > 10$ cm^{-3}
ϵ
|J| (nA m^{-2})
Counts
$\times 10^4$

Figure 5.

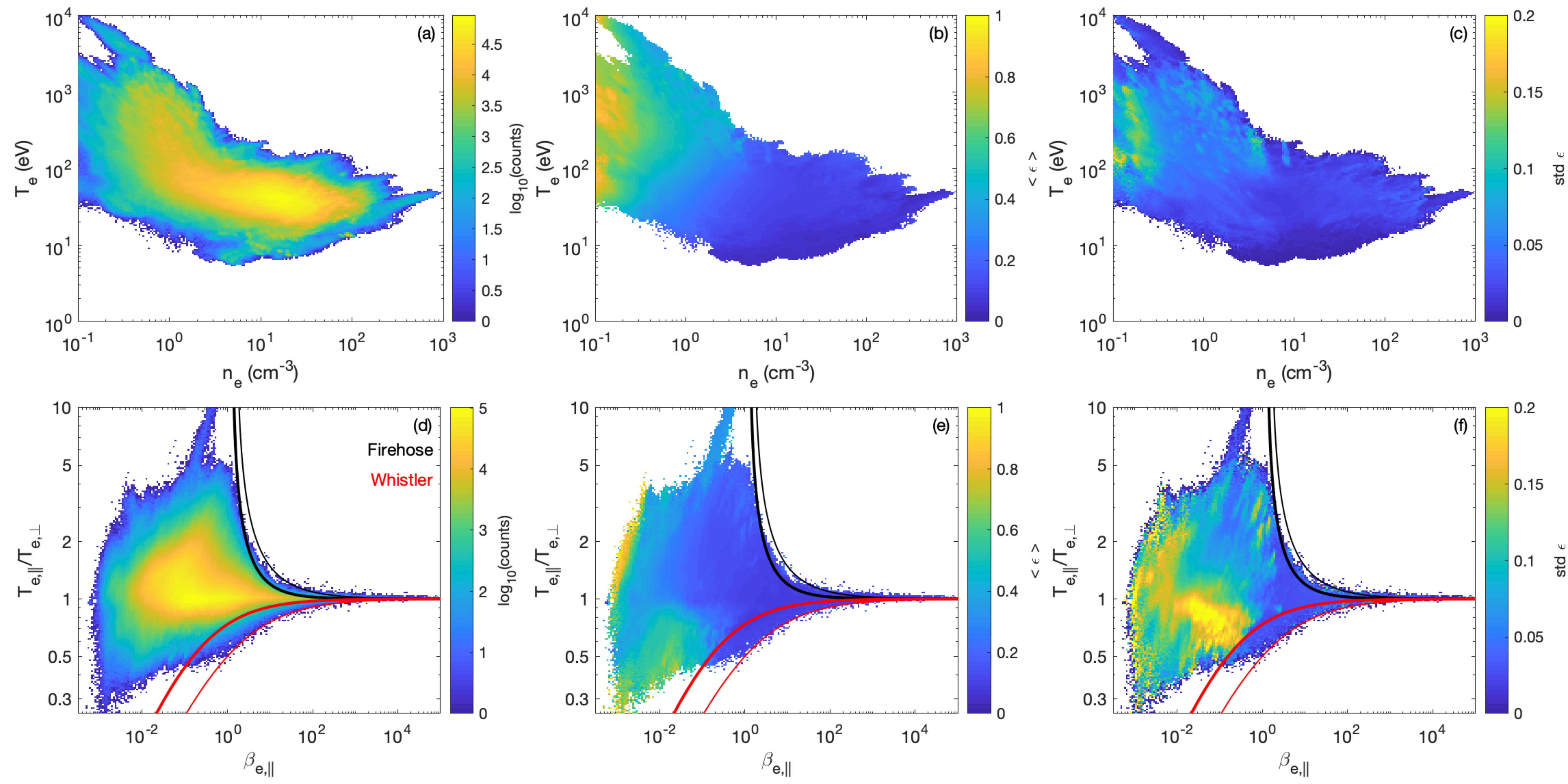

(a)
(b)
(c)
(d)
(e)
(f)
Firehose
Whistler
T_e (eV)
n_e (cm^{-3})
$\log_{10}$(counts)
$< \epsilon >$
std ϵ
$T_{e,\|}/T_{e,\perp}$
$\beta_{e,\|}$

Figure 6.

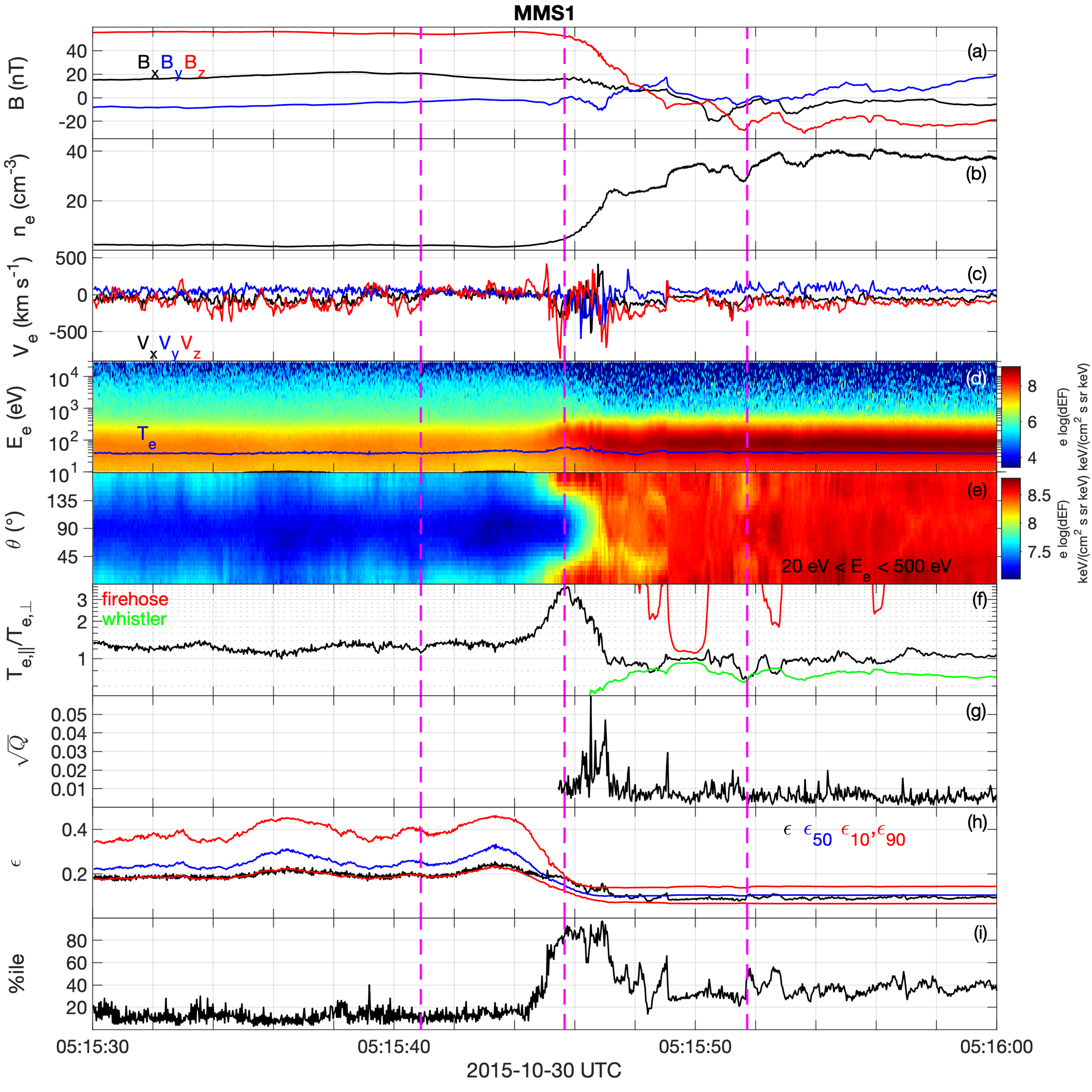

MMS1
B (nT)
Bx By Bz
(a)
ne (cm-3)
(b)
Ve (km s-1)
Vx Vy Vz
(c)
Ee (eV)
Te
(d)
e log(dEF) keV/(cm2 s sr keV)
θ (°)
(e)
20 eV < Ee < 500 eV
Te,||/Te,⊥
firehose
whistler
(f)
√Q
(g)
ϵ
ϵ ϵ50 ϵ10, ϵ90
(h)
%ile
(i)
05:15:30
05:15:40
05:15:50
05:16:00
2015-10-30 UTC

Figure 7.

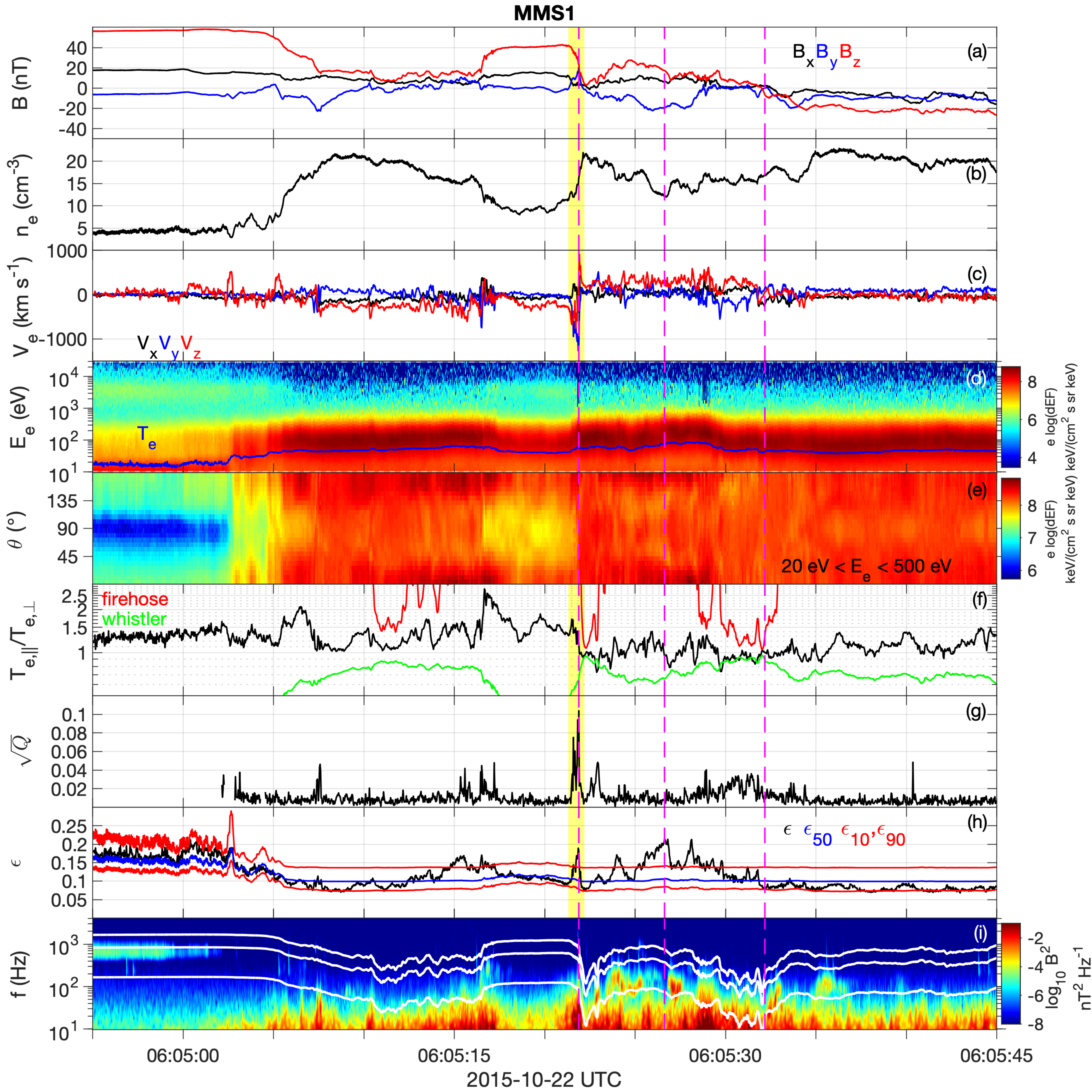

MMS1
B (nT)
(a)
Bx By Bz
ne (cm-3)
(b)
Ve (km s-1)
(c)
Vx Vy Vz
Ee (eV)
(d)
Te
e log(dEF) keV/(cm2 s sr keV)
θ (°)
(e)
20 eV < Ee < 500 eV
e log(dEF) keV/(cm2 s sr keV)
Te,||/Te,⊥
(f)
firehose
whistler
√Q
(g)
ε
(h)
ε ε50 ε10,ε90
f (Hz)
(i)
log10 B2 nT2 Hz-1
06:05:00
06:05:15
06:05:30
06:05:45
2015-10-22 UTC

Figure 8.

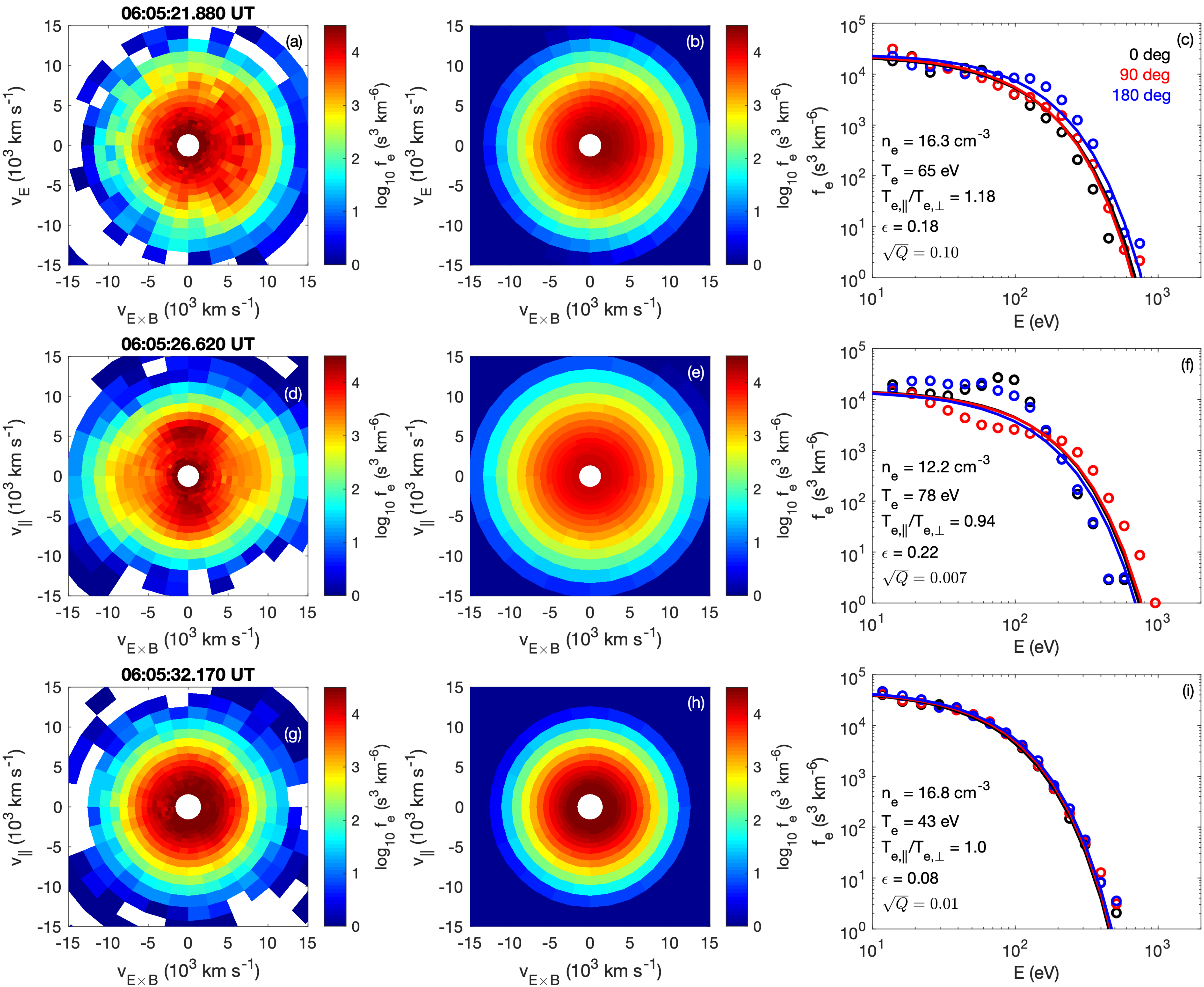
06:05:21.880 UT
06:05:26.620 UT
06:05:32.170 UT
(a)
(b)
(c)
(d)
(e)
(f)
(g)
(h)
(i)
0 deg
90 deg
180 deg
n_e = 16.3 cm^{-3}
T_e = 65 eV
$T_{e,\|}/T_{e,\perp}$ = 1.18
ϵ = 0.18
$\sqrt{Q} = 0.10$
n_e = 12.2 cm^{-3}
T_e = 78 eV
$T_{e,\|}/T_{e,\perp}$ = 0.94
ϵ = 0.22
$\sqrt{Q} = 0.007$
n_e = 16.8 cm^{-3}
T_e = 43 eV
$T_{e,\|}/T_{e,\perp}$ = 1.0
ϵ = 0.08
$\sqrt{Q} = 0.01$
v_E (10^3 km s^{-1})
$v_\|$ (10^3 km s^{-1})
$v_{E\times B}$ (10^3 km s^{-1})
$\log_{10} f_e$ (s^3 km^{-6})
f_e (s^3 km^{-6})
E (eV)

Figure 9.

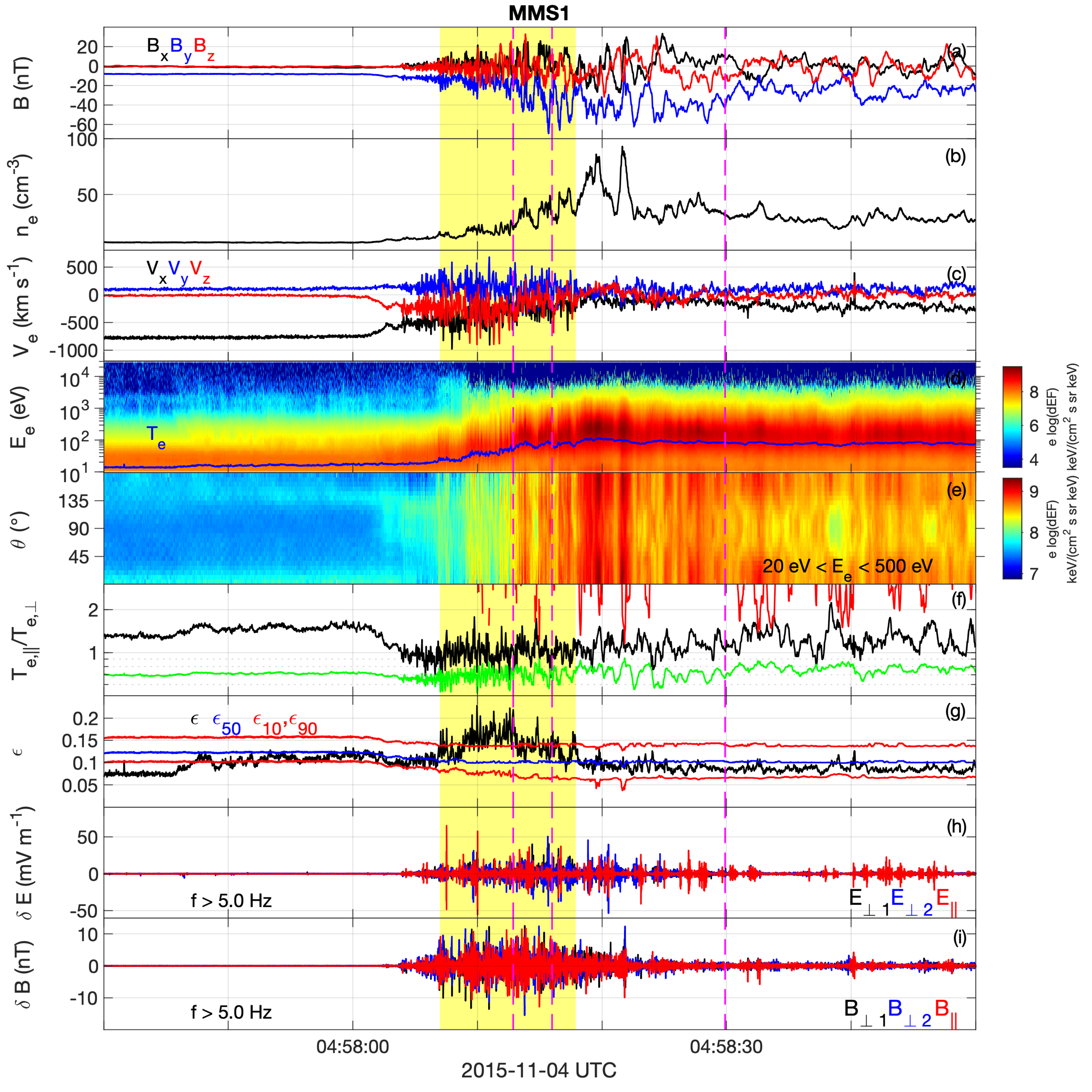

MMS1
B (nT)
$B_x B_y B_z$
(a)
n_e (cm^{-3})
(b)
V_e (km s^{-1})
$V_x V_y V_z$
(c)
E_e (eV)
T_e
(d)
e log(dEF) keV/(cm^2 s sr keV)
θ (°)
(e)
20 eV < E_e < 500 eV
$T_{e,||}/T_{e,\perp}$
(f)
ϵ
ϵ ϵ_{50} ϵ_{10},ϵ_{90}
(g)
δ E (mV m^{-1})
f > 5.0 Hz
$E_{\perp 1} E_{\perp 2} E_{||}$
(h)
δ B (nT)
f > 5.0 Hz
$B_{\perp 1} B_{\perp 2} B_{||}$
(i)
04:58:00
04:58:30
2015-11-04 UTC

Figure 10.

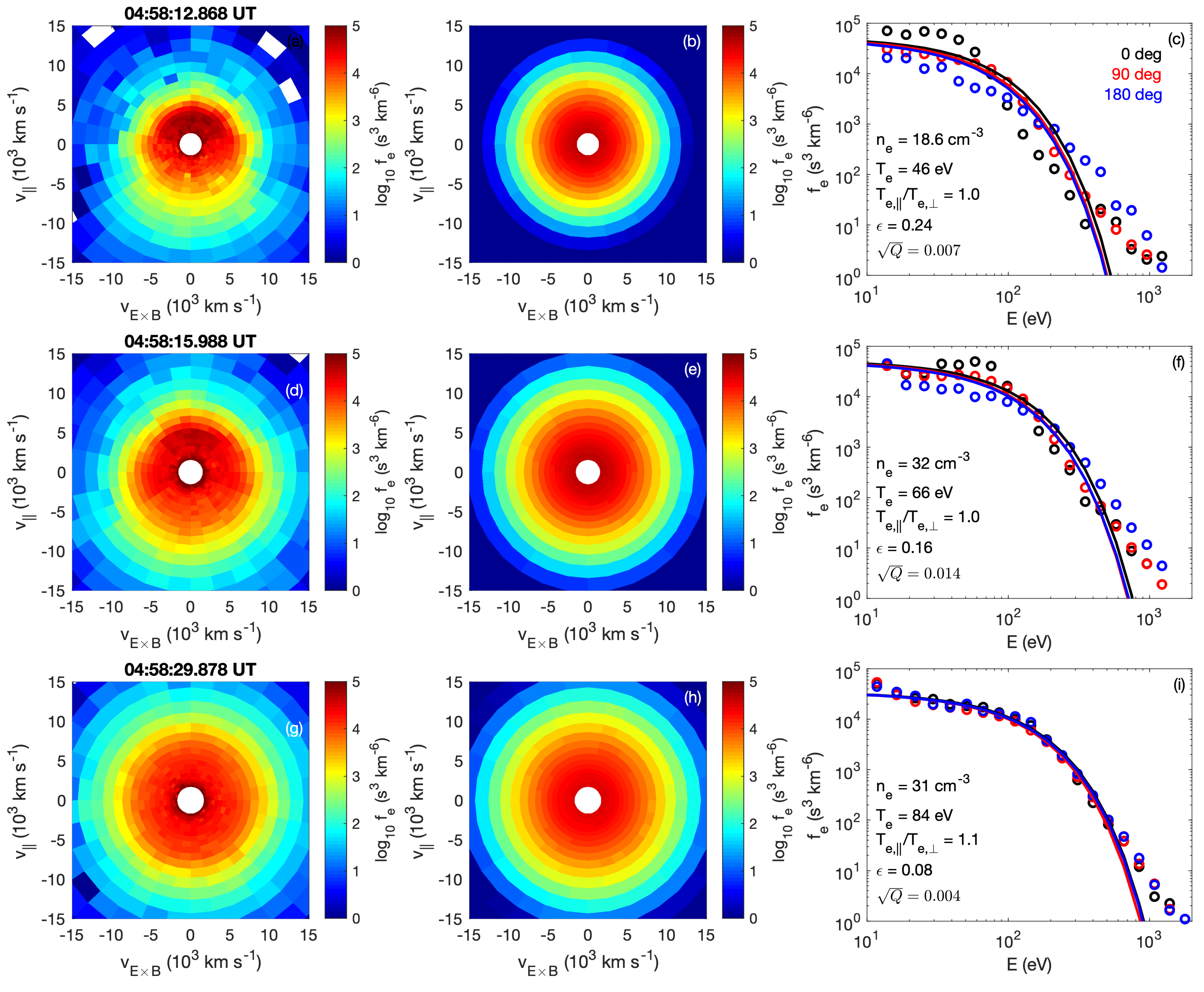

04:58:12.868 UT
04:58:15.988 UT
04:58:29.878 UT
(a)
(b)
(c)
(d)
(e)
(f)
(g)
(h)
(i)
$v_{\|}$ (10^3 km s^{-1})
$v_{E\times B}$ (10^3 km s^{-1})
$\log_{10} f_e$ (s^3 km^{-6})
f_e (s^3 km^{-6})
E (eV)
0 deg
90 deg
180 deg
n_e = 18.6 cm^{-3}
T_e = 46 eV
$T_{e,\|}/T_{e,\perp}$ = 1.0
ϵ = 0.24
$\sqrt{Q} = 0.007$
n_e = 32 cm^{-3}
T_e = 66 eV
$T_{e,\|}/T_{e,\perp}$ = 1.0
ϵ = 0.16
$\sqrt{Q} = 0.014$
n_e = 31 cm^{-3}
T_e = 84 eV
$T_{e,\|}/T_{e,\perp}$ = 1.1
ϵ = 0.08
$\sqrt{Q} = 0.004$

Figure 11.

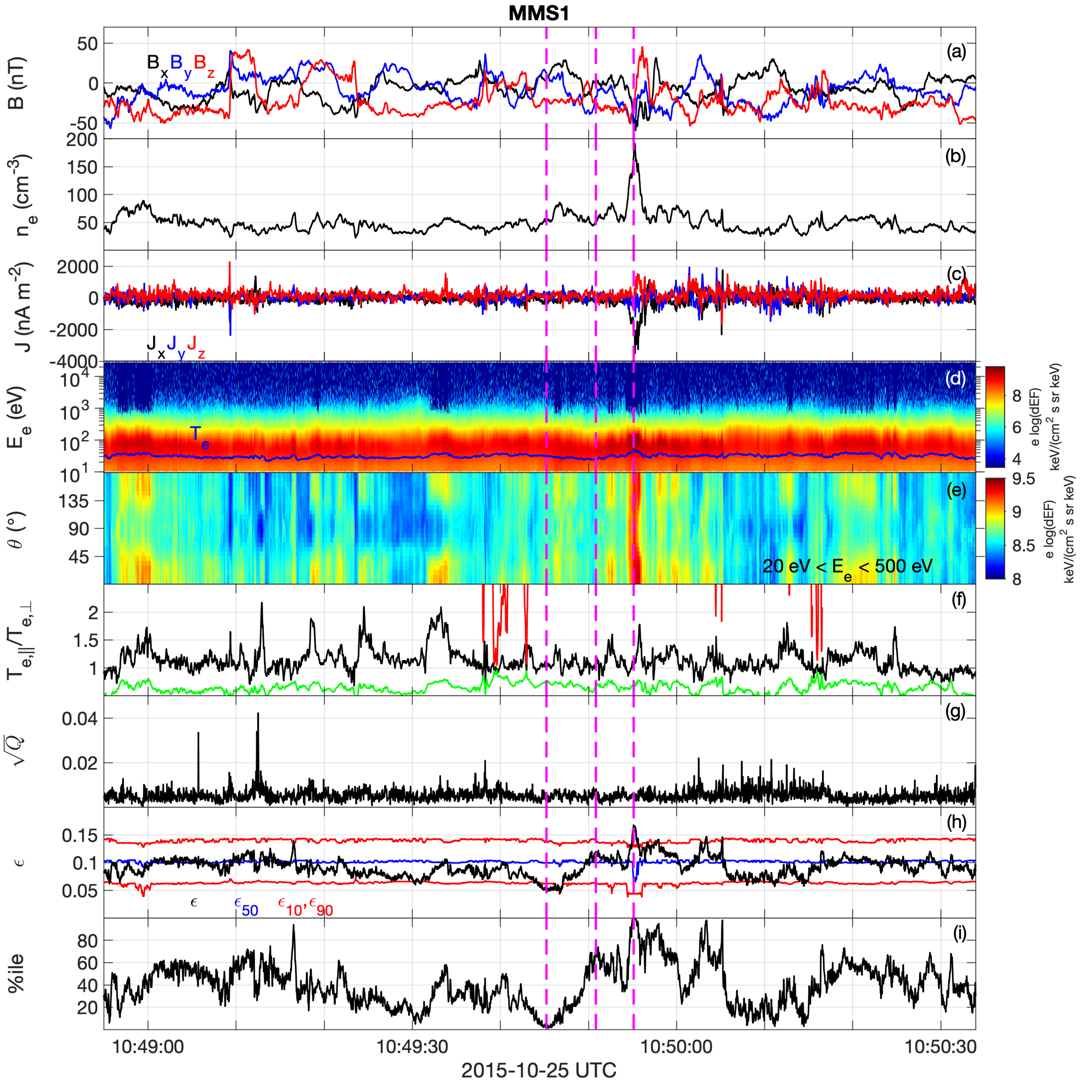

MMS1
B_x B_y B_z
B (nT)
(a)
n_e (cm^{-3})
(b)
J_x J_y J_z
J (nA m^{-2})
(c)
E_e (eV)
T_e
(d)
e log(dEF) keV/(cm^2 s sr keV)
θ (°)
(e)
20 eV < E_e < 500 eV
$T_{e,||}/T_{e,\perp}$
(f)
$\sqrt{Q}$
(g)
ϵ
(h)
ϵ ϵ_{50} ϵ_{10}, ϵ_{90}
%ile
(i)
10:49:00
10:49:30
10:50:00
10:50:30
2015-10-25 UTC

Figure 12.

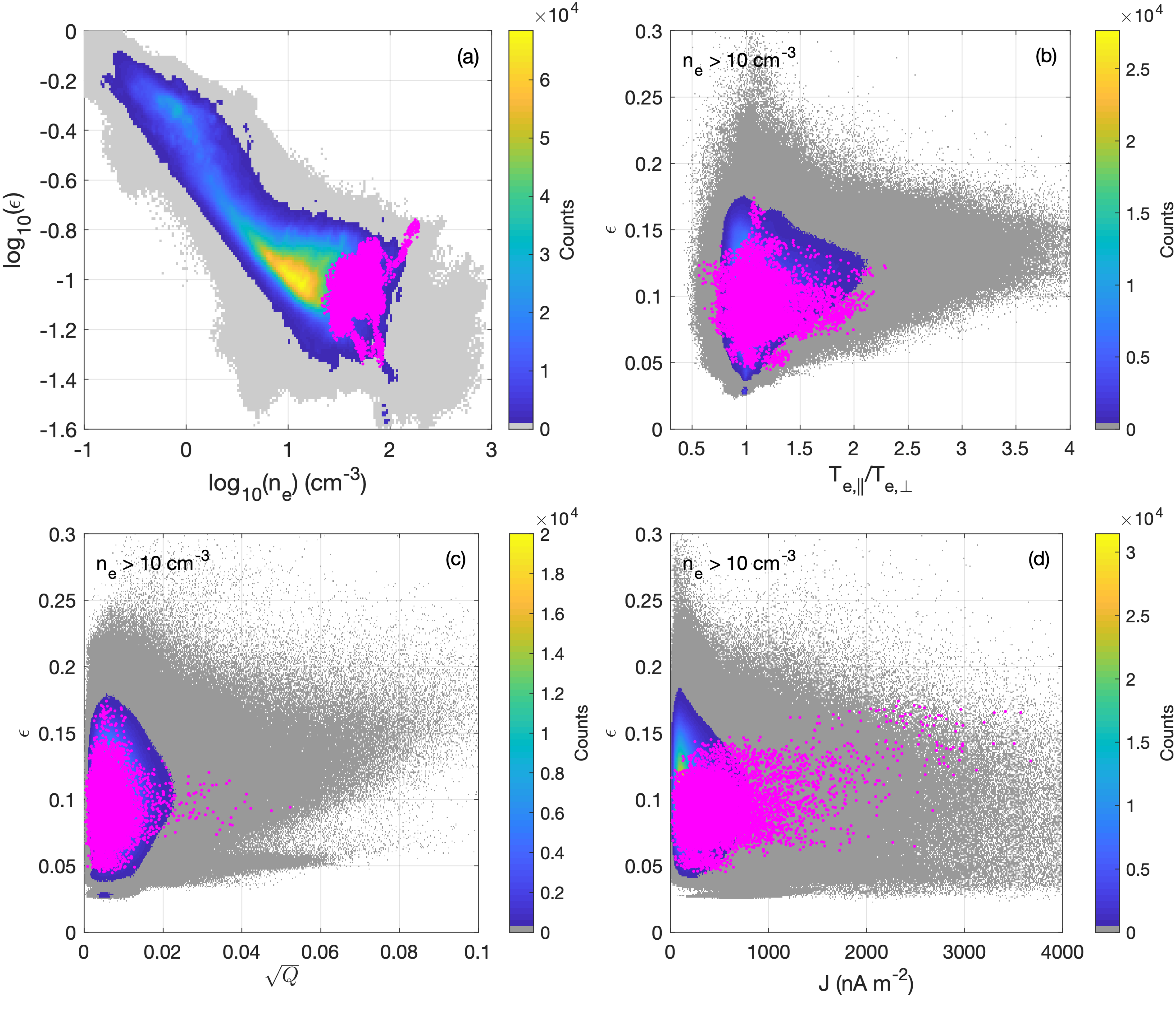

(a)
$\log_{10}(\epsilon)$
$\log_{10}(n_e)$ (cm^{-3})
$\times 10^4$
Counts
(b)
$n_e > 10$ cm^{-3}
ϵ
$T_{e,\|}/T_{e,\perp}$
$\times 10^4$
Counts
(c)
$n_e > 10$ cm^{-3}
ϵ
$\sqrt{Q}$
$\times 10^4$
Counts
(d)
$n_e > 10$ cm^{-3}
ϵ
J (nA m^{-2})
$\times 10^4$
Counts

Figure 13.

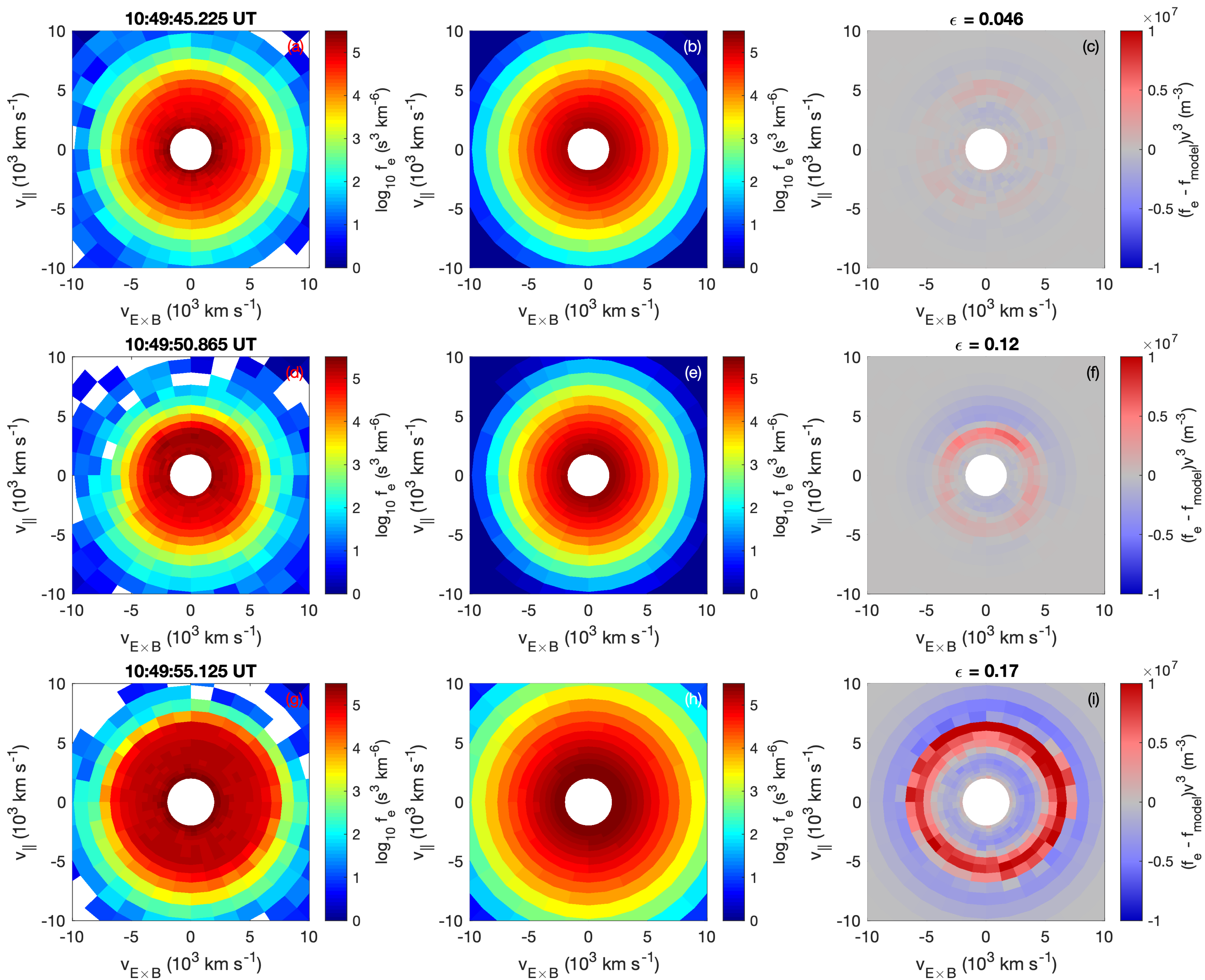

10:49:45.225 UT
(a)
(b)
ϵ = 0.046
(c)
10:49:50.865 UT
(d)
(e)
ϵ = 0.12
(f)
10:49:55.125 UT
(g)
(h)
ϵ = 0.17
(i)
$v_{||}$ (10^3 km s^{-1})
$v_{E \times B}$ (10^3 km s^{-1})
$\log_{10} f_e$ (s^3 km^{-6})
$(f_e - f_{model})v^3$ (m^{-3})
$\times 10^7$

Figure A1.

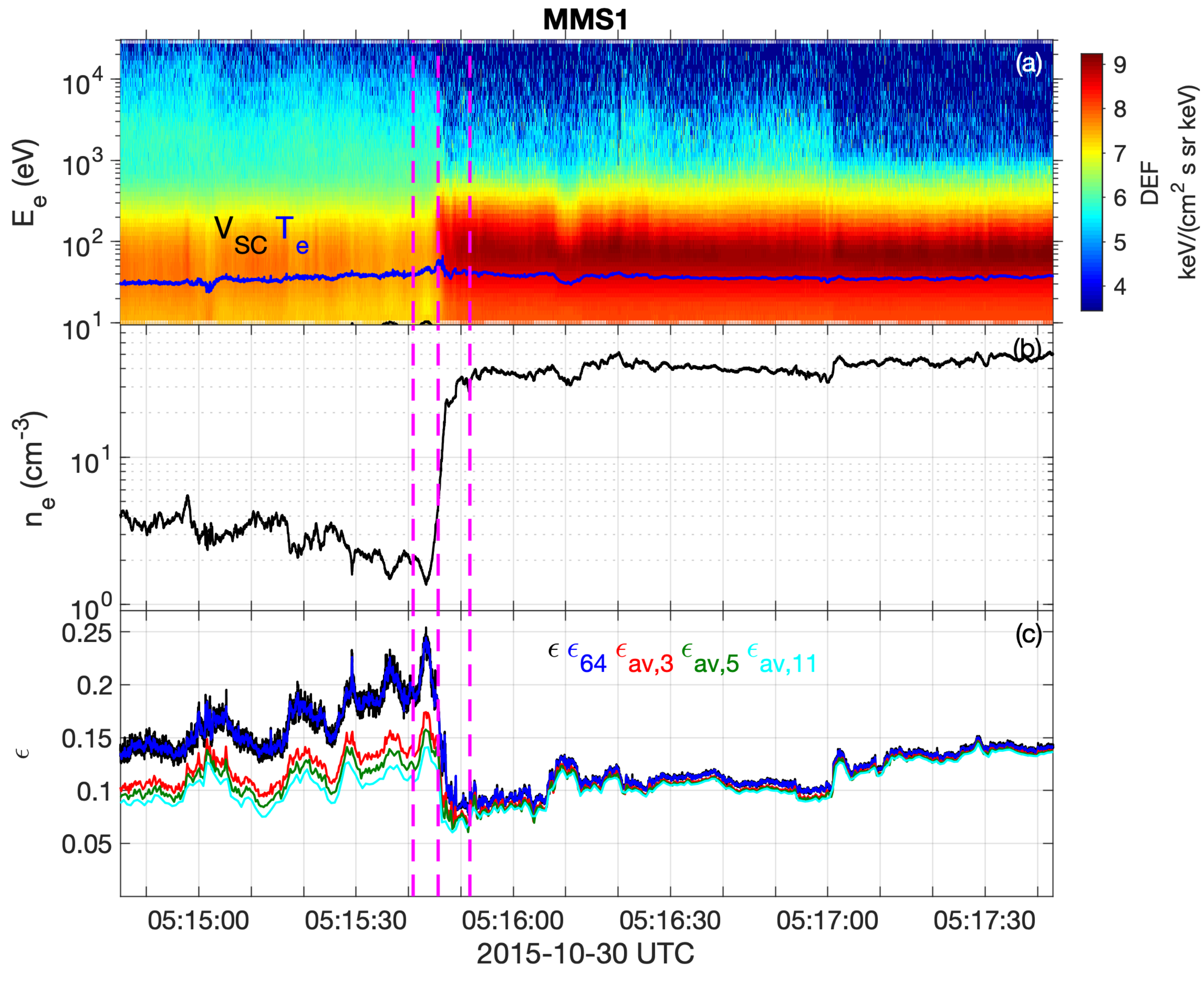

MMS1
(a)
(b)
(c)
E_e (eV)
n_e (cm^{-3})
ϵ
V_{SC} T_e
ϵ ϵ_{64} $\epsilon_{av,3}$ $\epsilon_{av,5}$ $\epsilon_{av,11}$
DEF keV/(cm^2 s sr keV)
05:15:00
05:15:30
05:16:00
05:16:30
05:17:00
05:17:30
2015-10-30 UTC

Figure A2.

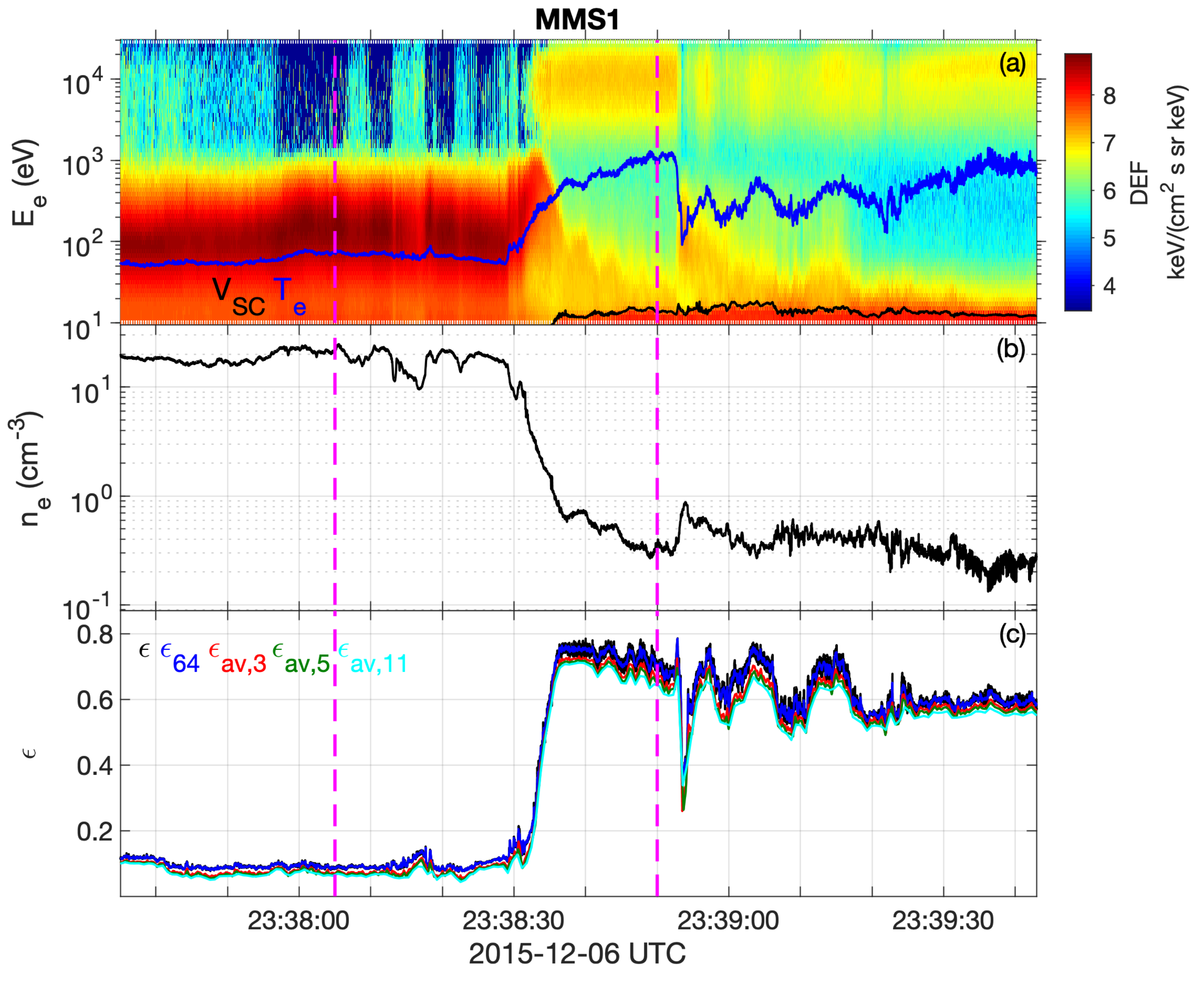

MMS1
(a)
(b)
(c)
E_e (eV)
n_e (cm^{-3})
ϵ
V_{SC} T_e
ϵ ϵ_{64} $\epsilon_{av,3}$ $\epsilon_{av,5}$ $\epsilon_{av,11}$
DEF
keV/(cm^2 s sr keV)
23:38:00
23:38:30
23:39:00
23:39:30
2015-12-06 UTC

Figure A3.

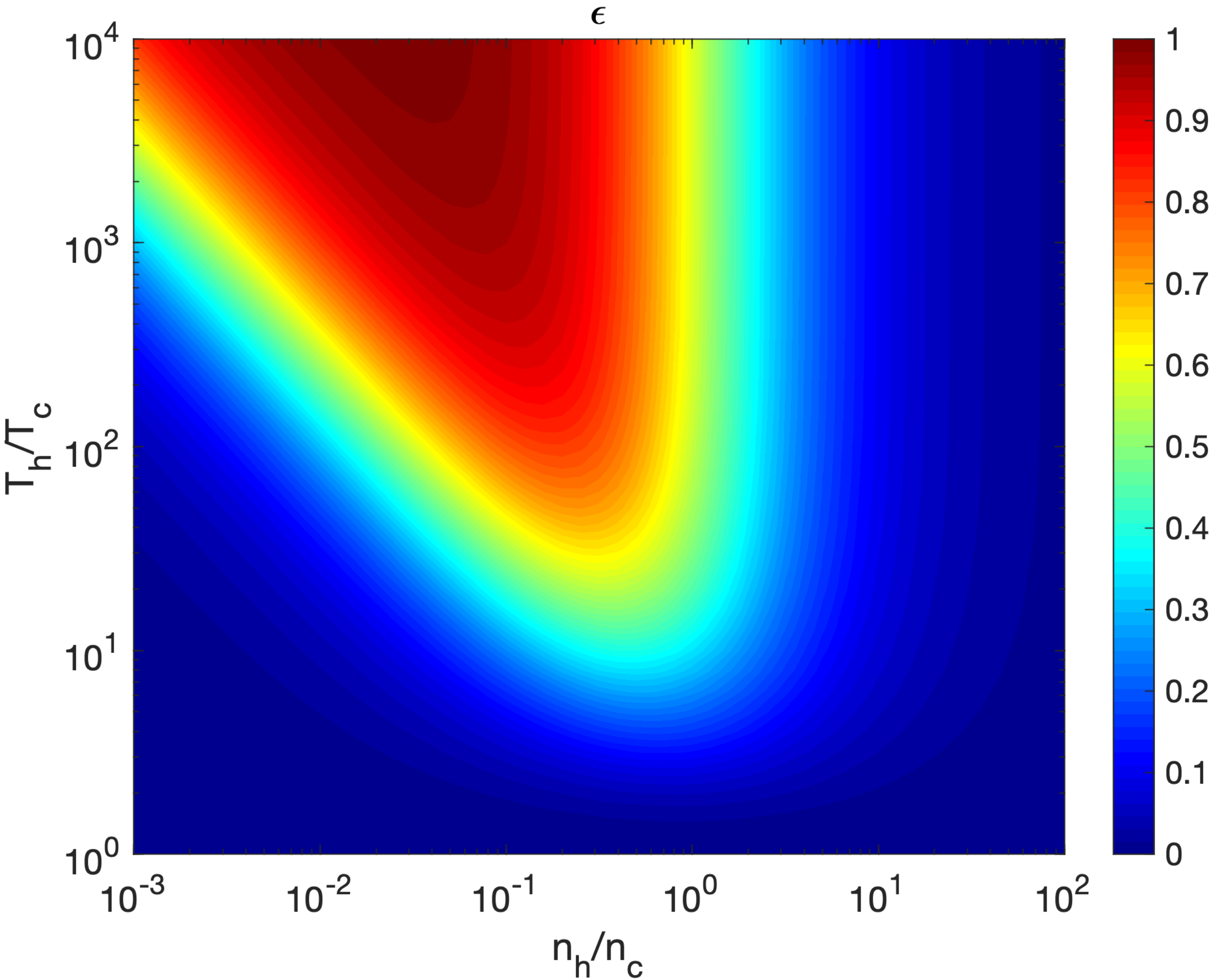

ϵ
T_h/T_c
10^4
10^3
10^2
10^1
10^0
10^{-3}
10^{-2}
10^{-1}
10^0
10^1
10^2
n_h/n_c
1
0.9
0.8
0.7
0.6
0.5
0.4
0.3
0.2
0.1
0

Figure A4.

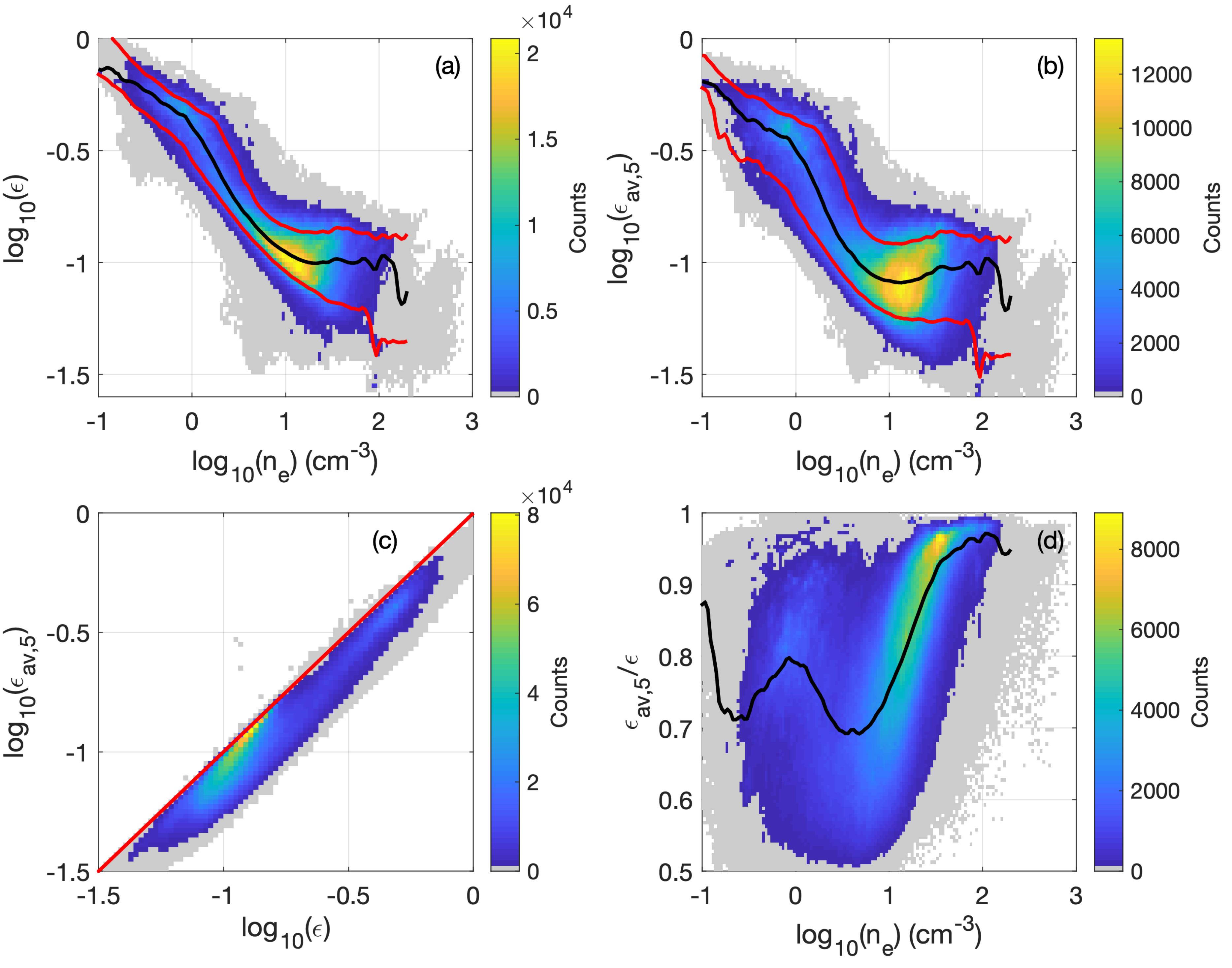

(a)
(b)
(c)
(d)
$\times 10^4$
Counts
$\log_{10}(\epsilon)$
$\log_{10}(\epsilon_{av,5})$
$\log_{10}(n_e)$ (cm^{-3})
$\epsilon_{av,5}/\epsilon$
0
-0.5
-1
-1.5
2
1.5
1
0.5
12000
10000
8000
6000
4000
2000
3
8
0.9
0.8
0.7
0.6